ELUCIDATING THE ONSET OF STALL AND CAVITATION BREAKDOWN IN AXIAL TURBOMACHINES AND APPLICATIONS OF CASING TREATMENTS TO ALLEVIATE THEM

by
Huang Chen

A dissertation submitted to the Johns Hopkins University in conformity with the requirements for the degree of Doctor of Philosophy

Baltimore, Maryland

March 2019

Abstract

Stall and cavitation breakdown are detrimental to the performance and structural integrity of axial turbomachines. However, the underlying mechanisms leading to them are not fully understood. This work utilizes a unique optical refractive index-matched facility at the Johns Hopkins University to study the onset of stall in an axial compressor and the causes for cavitation breakdown in a waterjet pump. Different types of casing treatments are applied to the turbomachines to delay the onset of stall or to mitigate the adverse effects caused by cavitation breakdown. Qualitative high-speed flow visualization of cavitation identifies the origin of vortical structures and follows their development in the rotor passage. High-resolution Particle Image Velocimetry measurements reveal the detailed flow structures and help to explain the effects caused by the structures with and without casing treatments.

Results have shown that the onset of stall in the axial compressor is associated with the development and propagation of a large-scale, inter-blade vortical structure called backflow vortices. To delay the onset of stall, semicircular axial casing grooves are installed and tested. Results show that the stall flow rate is reduced by 40% with performance degradation and efficiency loss at high flow rates. Detailed flow measurements in the rotor tip region reveal complex interactions between the tip flow and casing grooves. Relevant flow structures associated with stall delaying and efficiency loss mechanisms are identified. This study paves the way for designing better casing treatments that can delay the onset of stall while not degrade the performance at high flow rates.

Cavitation breakdown in the waterjet pump is initiated when the attached cavitation on the blade suction side develops into the blade overlap region and blocks a part of the passage. The narrowing passage results in a further acceleration of the flow, which in turn causes the reduction

in pressure, further development of cavitation, and the formation of large scale cavitating vortices that blocks the tip region. When the attached cavitation reaches near the blade trailing edge, the pressure on the suction side is nearly vapor pressure. A further reduction in the mean pressure directly unloads the blade pressure side, contributing to the dramatic performance degradation. Circumferential grooves are used to alleviate the performance breakdown caused by cavitation. However, limited success is achieved since the shallow groove only reduces the blockage in the tip region briefly in the early phase of cavitation breakdown.

Advisor: Professor Joseph Katz

Readers: Professor Dennice Gayme and Professor William Blake

Acknowledgements

During this long journey of my Ph.D. study at JHU, I am indebted to many people. My advisor, Prof. Joseph Katz, has been a true mentor. His excellent knowledge of experiments and fluid dynamics has navigated me through the difficulties in research. His uncompromising attitude and the willingness to pursuit perfection has encouraged me to push the boundaries. I am thankful for the knowledge I've learned from him, which will surely guide me through the rest of my career.

I want to thank Prof. Dennice Gayme and Prof. William Blake for spending their precious time reading this thesis. I would also like to thank Prof. Darryn Waugh, Prof. Anand Gnanadesikan, Prof. Ciaran Harman and Prof. Dennice Gayme (again) for serving as my Graduate Board Oral exam committee members. I am thankful to other faculty members in the Department of Mechanical Engineering for their instructions.

This experimental study is teamwork. Special thanks to Dr. Yury Ronzhes who designed and built this wonderful facility, and helped us to deal with countless (non-safety-related) emergencies during experiments. I want to thank Dr. David Tan, Dr. Chao Zhang, Dr. Kaushik Sampath, and Dr. Yuanchao Li, who taught me everything about the facilities and experiments and helped me with daily operations. Thanks to my co-workers Nick Doeller, Subhra Shankha Koley, Jibu Tom Jose, and Ayush Saraswat who have helped me tremendously during the experiments. Thanks to all my labmates, Dr. Cheng Li, Dr. Hangjian Ling, Dr. Lakshmana Dora, Dr. Jian Gao, Dr. Omri Ram, Jing Wang, XinZhi Xue, Karuna Agarwal, and Zeng Zhang, who I have been privileged to work with. Also, I would like to thank the hard-working undergrad research assistants, including Ian Wilkes, Benjamin Keyser, Sydrake Abdi, Khan Nguyen, John Moore, Chris Williams, Paarth Sharma, and Arion Morshedian. Thanks to Barb Adamson for her help in the daily lab operations.

I am in great debt to the NASA Glen Research Center and the Office of Naval Research who are the sponsors for my Ph.D. study. Special thanks to Dr. Chunill Hah of NASA Glenn for his help in the NASA project.

Without the encouragement and support from my family and friends, I wouldn't finish this long endeavor. I am especially grateful to my wife, Limeng Xie, for her understanding, support, companionship, and love.

Contents

List of Figures

List of Tables

Nomenclature

A	=	through-flow area
c	=	rotor blade tip chord
c_A	=	rotor blade tip axial chord
h	=	width of the rotor blade tip gap
H	=	rotor blade span
k^*	=	normalized turbulent kinetic energy
L	=	nominal distance from the hub to the inner casing endwall
p_{exit}	=	static pressure at stator outlet
p_{in}	=	static pressure upstream of the IGV
P_{0i}	=	total pressure upstream of the IGV
Q	=	volumetric flow rate
r, z, θ	=	radial, axial and circumferential coordinates
r^*	=	normalized radial coordinate
r_{hub}	=	rotor hub radius
s	=	rotor blade chordwise coordinate
t^*	=	normalized time
T	=	motor input torque
u, v, w	=	velocity components in laser sheet coordinate system
u_r, u_z, u_θ	=	radial, axial and circumferential velocity
U_r, U_z, U_θ	=	esemble-averaged radial, axial and circumferential velocity
U_{T}	=	rotor blade tip speed

U^*_n	=	tip leakage flow normal to the blade chord in the rotor reference frame
$U_{z,in}$	=	axial velocity at the inlet to AxWJ-2
u'	=	velocity fluctuation
V_z	=	average axial velocity in the rotor passage
W	=	fluid speed in the rotor reference frame
x', y', z'	=	laser sheet coordinate system
ρ	=	NaI solution density
φ	=	normalized flow coefficient for NASA compressor
φ_P	=	normalized flow coefficient for AxWJ-2
η	=	efficiency
θ_{blade}	=	circumferential angle of a rotor passage
θ_{PIV}	=	circumferential location of the laser sheet coordinate system
σ	=	cavitation index
σ_{local}	=	local cavitation index
ψ_{SS}	=	static-to-static pressure rise coefficient
ψ_{TS}	=	total-to-static pressure rise coefficient
ψ_P	=	normalized head rise coefficient for AxWJ-2
$\omega_r, \omega_z, \omega_\theta$	=	radial, axial and circumferential vorticity
Ω	=	rotor angular velocity
$< >$		ensemble averaged quantity

Chapter 1 Introduction

Turbomachines are widely used in industries to convert energy between rotating blades and fluids. Due to the mechanical complexities of a rotating machine, flow phenomena within turbomachines are usually complicated, not well-understood, and are subject to active research. This experimental work investigates two extreme phenomena in turbomachines, namely onset of stall in compressors and cavitation performance breakdown in pumps. Later, different types of casing treatments are installed in the machines aiming at delaying the onset of stall or mitigating the adverse effects caused by cavitation breakdown. In a unique refractive index-matched liquid facility at JHU, a variety of experimental techniques including high-speed imaging of cavitation and Particle Image Velocimetry (PIV) are used to characterize the flow near the rotor blade tip region as well as in the rotor passage, with and without casing treatments. Detailed analyses of the causes for the onset of stall and cavitation breakdown are presented. Flow structures that are associated with the increased performance by casing treatments are discussed, and novel concepts of casing treatments are tested.

1.1 Compressor stall

The operating conditions of a turbomachine at a fixed speed can usually be described by three variables, flow rate (φ), pressure (head) rise across the machine (ψ) and efficiency (η). Relations between the three variables are illustrated by sample φ-ψ and φ-η curves in Figure 1-1. As shown in Figure 1-1a, ψ initially increases with decreasing φ, then decreases as the machine stalls. The point when the head rise reaches the maximum value just before decreasing is usually called the pre-stall condition. The φ-η curve in Figure 1-1b shows a similar trend. The efficiency increases initially with decreasing flow rate and then decreases. The point where the machine

reaches the peak efficiency is called the Best Efficiency Point (BEP). However, the BEP usually occurs at a much higher flow rate than the pre-stall condition. The general goal of turbomachine research is to develop a machine that has the highest possible efficiency while has the lowest possible pre-stall flow rate. Specifically, the goal of this experimental work is to investigate the flow phenomena leading to the onset of stall and the uses of casing treatment to delay stall while minimizing the efficiency loss at high flow rates.

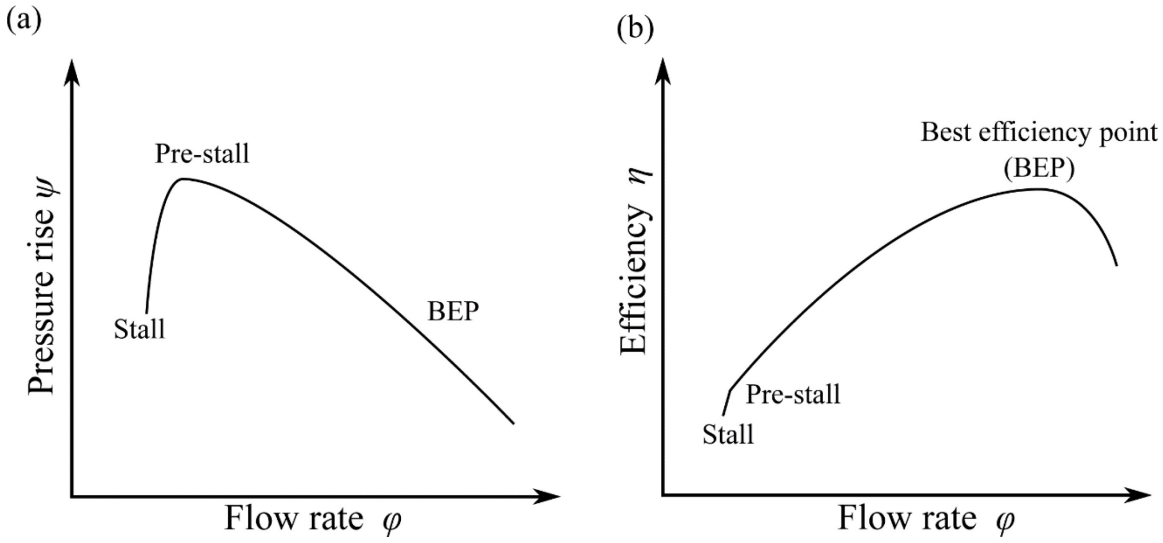

Figure 1-1 Sample illustration of (a) φ-ψ curve and (b) φ-η curve.

When the flow rate is reduced, an axial compressor becomes less stable and more prone to stall, where the pressure rise across the pump drops dramatically. In extreme cases, a negative flow rate can occur, a phenomenon called compressor surge (Fukano *et al.*, 2004; Pampreen, 1993; Schoenenborn *et al.*, 2012). Understanding how instabilities develop in the rotor passage and grow into a full-scale stall, i.e., the stall inception, is important in developing tools to predict it and developing methods to mitigate its adverse effects (Day, 2015). In a developed state, multiple stall cells propagate circumferentially in a phase velocity that is typically lower than that of the rotor speed, a phenomenon typically referred to as rotating stall (Emmons, H. *et al.*, 1955; Greitzer, 1976).

The precursors to stall are generally divided into two types, namely the long length-scale "modal-type" and the short length-scale "spike-type." Modal-type stall inception involves a long length-scale, wave-like circumferential velocity variations before stall cells appear (Camp *et al.*, 1998; Day, 1993; Garnier *et al.*, 1991; McDougall *et al.*, 1990). In comparison, spike-type stall inception typically involves a large pressure spike at the endwall casing near the leading edge (LE) of the rotor (Camp *et al.*, 1998; Deppe *et al.*, 2005; Tan *et al.*, 2010) before stall. The exact reasons for spike-type stall are still under debate, in spite of the numerous experimental and computational studies attempting to elucidate it.

Surface-oil flow visualization and casing pressure measurements by Deppe *et al.*, (2005) show that spike formation involves leading-edge spillage and the trailing-edge backflow, proposed by Vo *et al.*, (2008) as the criteria for spike-type stall inception. Measurements by Inoue et al. Inoue *et al.*, (2001, 2002) indicate that a large low-pressure region exists ahead of the rotor passage during stall, leading them to postulate the presence of a "tornado-like" vortex originating from leading edge separation, with one end at the suction side (SS) of the blade and the other at the casing. A similar inter-blade vortex has also been observed by Kosyna et al. within a single-stage axial-flow pump in deep stall (Kosyna *et al.*, 2005). Subsequent pressure measurement and simulation by Yamada *et al.* (2013) agree with these findings and their relations to the onset of spike-type stall. They show that the tornado-like separation vortex propagates circumferentially to the adjacent blade and induces separation there. Numerical simulations by Pullan *et al.* (2015) indicate the leading edge separation induced by high incidence at the rotor tip is the cause of spike-type stall. More importantly, they demonstrate that tip leakage flow is not a necessity in terms of leading edge separation or spike formation, although the leakage flow itself contributes to the high incidence angle of the adjacent blade. Spike-type stall involving leading edge separation has also been observed computationally in centrifugal compressors (Everitt *et al.*, 2012).

A computational study by Hoying *et al.* (1999) shows that the stall inception is caused by the interaction of the tip leakage vortex (TLV) with the leading edge of the adjacent blade when

the TLV is aligned circumferentially at low flow rates. Simulations by Hah *et al.* (2006) indicate that leading edge spillage and stall onset occurs when the tip leakage flow from one blade reaches the pressure side (PS) of the next blade.

Another type of large scale instability occurring in the rotor passage has been called "rotating instability" by several researchers (Day, 2015; Mailach *et al.*, 2001; März *et al.*, 2002; Mathioudakis *et al.*, 1985; Young *et al.*, 2012), although the specific nature of this phenomenon is still not resolved. März *et al.* (2002) argued, based on an experimental and numerical study that this phenomenon is caused by the migration of low pressure areas from one blade to the next. They show that the instabilities are more likely to happen for a large tip gap, and attribute the low pressure region to the leg of an axial vortex.

1.2 Cavitation breakdown

Adverse effects of cavitation have caused major concerns in marine propulsion, liquid handling turbomachinery, and other hydraulic systems. These effects include erosion (e.g., Philipp and Lauterborn 1998), instabilities (e.g., Tsujimoto et al. 1997) decrease in performances (e.g., Ng and Brennen 1978), and noise (e.g., Chudina 2003). A sudden and severe degradation of pump performance at low inlet pressures, so-called cavitation breakdown, is one of the most severe effects. Numerous experimental and theoretical studies have shown that temperature, flow rate, rotor tip clearance, blade solidity, and geometry affect cavitation breakdown (summarized by Arndt 1981 and Brennen 1994). However, the specific causes of this phenomenon and the mechanisms involved are still unknown.

Several possible explanations have been proposed for the onset of cavitation breakdown. For example, based on experimental observations and theoretical analyses, Pearsall (1973) suggests that cavitation breakdown occurs when the attached cavitation at the SS of the blade surface extends into the blade overlap region, blocking the passage flow. Using RANS simulation

on the same axial waterjet pump studied in this work, Lindau *et al.*, (2012) propose that the rapid performance degradation is caused by the blocking of the trailing edge region by cavitation. A theoretical model by Jakobsen, (1964) shows that the rapid decrease in the speed of sound caused by cloud cavitation might lead to the development of shock waves and associated performance breakdown. A recent study by Tan et al. (2015) argues that interactions between the TLV and the vortical cloud cavitation on the SS of the rotor play a key role in the onset of cavitation breakdown. The TLV entrains the cloud cavitation and reorients it perpendicularly to the blade SS surface. When this process occurs in the blade overlap region, the resulting perpendicular cavitating vortices (PCV) extend from the SS surface of the originating blade to the PS of the neighboring blade, essentially blocking the passage. When the passage flow in the tip region of the rotor passage is blocked, the PCV rotates with the blade, while migrating slowly downstream. Subsequently, the presence of PCVs and formation mechanisms have been confirmed experimentally and computationally by Zhang *et al.*, (2015) for other machines. Based on this perceived mechanism, preventing the formation of PCVs could presumably alleviate the rapid degradation during the breakdown.

1.3 Casing treatments

Casing treatments have been used successfully to delay the onset of stall in axial turbomachines with a limited penalty in efficiency (Moore *et al.*, 1971; Osborn *et al.*, 1971; Prince *et al.*, 1975). Among the different approaches, axial casing grooves (ACGs) have been found to be the most effective (Fujita *et al.* 1984). Considerable efforts have already been invested to understand the flow mechanism involved and to optimize the geometry of ACGs. For example, Takata *et al.* (1977) show experimentally that the stall is delayed only when the ACG is skewed in the direction of the rotor rotation, and that the grooves generate periodic high-speed jets in front of the blade, which increases the incidence angle at the entrance to the passage. Smith *et al.* (1984)

observe that ACGs cause a considerable increase in blade loading near the tip, presumably by reorienting the flow. Stereo-PIV (SPIV) measurements in a transonic compressor rotor by Brandstetter *et al.* (2014) show that the ACGs generate periodic jets and suppress the tip region blockage. Experimental and numerical studies by Müller *et al.* (2011), using ACGs that are very similar to those used in the present study, show a 23% increase in stall margin and the associated reduction in tip region blockage. Crook *et al.* (1993) show numerically that the improvement to the stall margin by ACGs involves suppression of the TLV-induced blockage by sucking the low energy fluid and reinjecting it at high speed in front of the passage. Recent studies mostly involve RANS simulations. For example, Beheshti *et al.* (2004) show that the ACGs are more effective in rotors with a large tip gap. Wilke *et al.* (2004) associate the improvement with suppression of the tip leakage flow and reduction in TLV strength. Recommendations for groove geometries based on steady-state single passage simulations are provided by Djeghri *et al.* (2015). They show that the skew angle and axial position of the groove have more impact on the stall margin improvement than the slot depth and shape.

In spite of the stall delaying effect, casing grooves tend to cause efficiency loss at a higher flow rate, near the BEP of the machine. Measurements by Müller *et al.* (2011) have shown that ACGs similar to those used in the present study cause a 0.5% efficiency penalty in a transonic compressor rotor. Reynolds-averaged Naiver-Stokes (RANS) simulations by Wilke *et al.* (2004) show that when the ACGs are located around a transonic rotor blade LE, there is a 0.2% efficiency loss, but the loss increases to 4% when the groove is centered above the rotor. They associate the efficiency loss with the distortion of the shock system in the blade passage. Similar trends have been reported in Osborn *et al.*, (1971); Seitz (1999), suggesting that positioning the grooves around the LE minimizes the efficiency loss while maintaining similar stall margin improvements compared with the grooves located at the mid-chord. In contrast, results reported by Beheshti *et al.* (2004) based on Favre-averaged Naiver-Stokes simulations have shown an increase in the peak efficiency by ACGs. Efforts have also been invested in modifying groove geometry to minimize

efficiency loss. For example, Weichert *et al.* (2011) propose a self-regulating casing treatment that maintains the circulation in the groove at a low flow rate to delay stall, but minimizes flow into the groove at high flow rates to improve the efficiency. They achieve a 6% increase in stall margin and 0.8% efficiency loss. This work is aimed at finding casing grooves that can delay stall without causing efficiency loss using the knowledge learned from examining the flow in the rotor passage with and without casing grooves.

There is another type of groove that orientates in the circumferential direction, which is called as the circumferential groove (CG). Experimental and numerical studies by, e.g. Takata *et al.* (1977) and Müller *et al.* (2011) show that when equipped with proper CGs, the stall margin of axial compressors is increased by 3.8% and 7.3%, respectively. Kang *et al.* (2010) demonstrate experimentally and numerically that backflow cavitating vortices developing upstream of an inducer are confined in the CG, greatly reducing the extent of these vortices upstream of the groove. Consequently, instabilities associated with backflow cavitation are suppressed significantly. An experimental study by Choi *et al.* (2007) shows that the suction performance of a pump can be improved by employing axially orientated "J-Groove". They conclude that the improvement is caused by the leakage of fluid from the pressure side of the blade to low-pressure regions through the axial grooves. However, the improvements are small and occur only below design conditions.

Chapter 2 Experimental Setup

The experimental investigations of flows in turbomachines face one particular challenge: Limited access to the flow inside the rotating blade passages, especially in the tight tip gap region. Past research usually relied on complicated optical setups and only low-resolution data is obtained (e.g., Brandstetter *et al.*, 2014; Yu *et al.*, 2007). To address this problem, a unique refractive index-matched facility has been built at JHU. By matching the refractive index of the acrylic blades and casing with that of the working fluid, an aqueous solution of sodium iodide, unobstructed optical access is achieved. Taking advantage of this optical access, qualitative flow visualization of cavitation identifies the origin of flow structures and follows their development in the rotor passage. High-resolution PIV measurements reveal the detailed flow structures and help to explain the underlying mechanisms associated with them.

Past studies in the current facility have successfully examined the blade-wake interactions between different stages (Chow *et al.*, 2005; Soranna *et al.*, 2006; Uzol *et al.*, 2001), tip flows and complex vortical structures (Miorini *et al.*, 2012; Tan, 2015; Tan *et al.*, 2015b; Wu *et al.*, 2011b, 2011a, 2012), the effects of tip gap size on the performance of the machine (Li, 2018; Li *et al.*, 2016), and turbulence in the rotor passage and the associated modeling issues (Li, 2018; Li *et al.*, 2017, 2019). In this Chapter, detailed descriptions of the test loop and facility used in the current studies are provided. General experimental setup for cavitation visualization, PIV measurements, and data processing techniques are discussed. More detailed setups for individual experiments is included at the beginning of the corresponding Chapters.

2.1 Test loop, NASA compressor and AxWJ-2 waterjet pump

Test loop

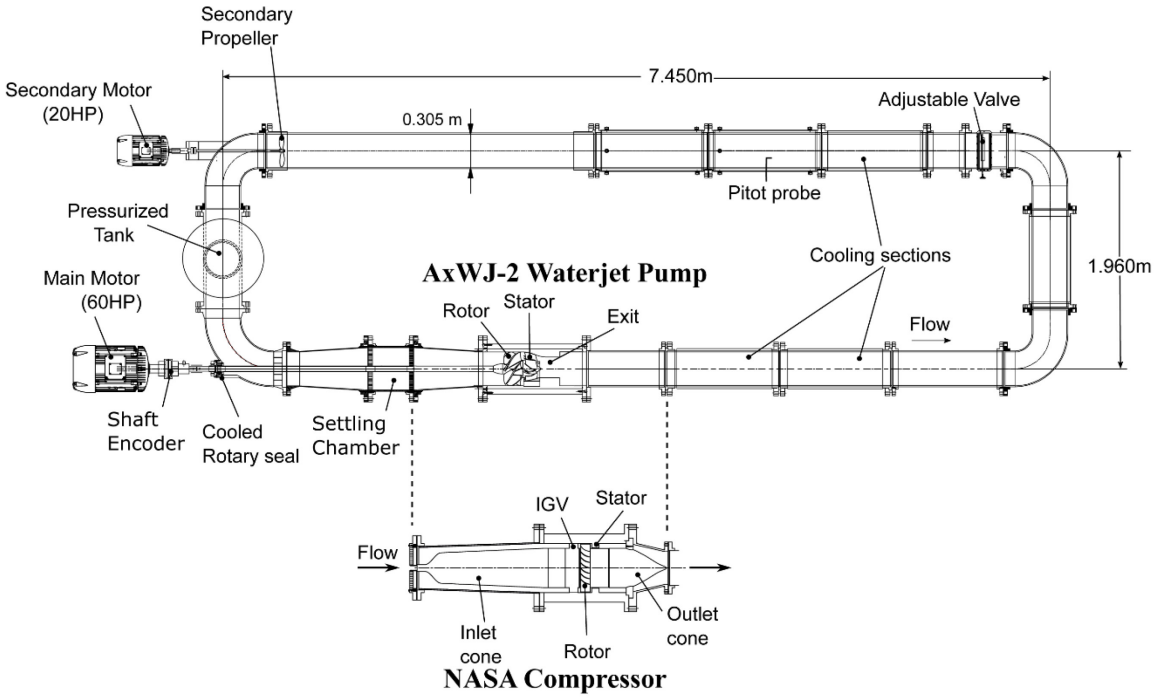

Figure 2-1 The JHU closed-loop refractive index-matched facility

As shown in Figure 2-1, the JHU refractive index-matched facility is closed-loop with an exchangeable test section. The 60HP motor drives the main 50.8 mm diameter shaft, which powers the rotors in the main test section. In addition, a 20HP auxiliary pump has been added to the other side of the loop, allowing us to easily control the flow rate in the loop and to operate at higher flow rates. Both motors are controlled by precision variable frequency drives. The flow and pressure drop in the loop is controlled by an adjustable valve consisting of two perforated disks, which is installed in the return line. The working fluid is 62%-63% by weight concentrated sodium iodide solution, whose refractive index, about 1.49, is matched with that of the acrylic blades and casing. The specific gravity of the solution is 1.8 and its kinematic viscosity at the experimental temperatures is about $1.1\times10^{-6}\,m^2s^{-1}$ (Bai *et al.*, 2014). Liquid temperature is maintained in the 20-

25 ºC range by circulating chilled water through three cooling sections shown in Figure 2-1. The mean pressure is controlled by connecting a half-filled tank located above the facility to a vacuum pump and a source of compressed nitrogen.

The rotor blade phase is monitored by a shaft encoder, enabling us to perform synchronized measurements at desired phases. A strain gauge based torque meter (SensorData® T261-STD-A) integrated with the shaft before it penetrates the loop is used for measuring the power input to the machine. This sensor has been calibrated by the manufacturer prior to the experiments, and they claim that the specified uncertainty is on the order of 0.1% for the present conditions. The torque required to overcome the resistance of the bearing system and rotor hub has been measured by running the rotor hub with flush blanks replacing the rotor blades under the same conditions as the experiments. This torque is subtracted from the measured values when the torque applied on the blades is calculated. The static pressure difference across the machine is monitored by a differential pressure transducer connected to pressure ports upstream of the IGV and downstream of the stator (Chen *et al.*, 2017c; Tan *et al.*, 2015b). The volumetric flow rate is measured by integrating the velocity profile obtained from translating a Pitot tube in the radial direction in the return line of the loop. The data for each point in the performance curve is recorded after operating the machine for several minutes under the same conditions. Accounting for all the contributors, the uncertainties associated with the measured head rise, flow rate, and efficiency are around 1.2%, 1.7% and 2.2%, respectively. The uncertainty in efficiency includes the effects of measurements of flow rate, pressure rise, torque, and even speed (small). The uncertainty in pressure coefficient (1.2%) accounts for the transducer's accuracy and standard deviation of results integrated to a single averaged value (200,000 data points). The uncertainty in flow coefficient (1.7%) includes the effect of transducer accuracy, Pitot tube location and standard deviation of variations in data. The uncertainty in torque (very small) includes effects of all the sensors, the torque without blades for subtraction, and speed. The flow rate and pressure rise are the main contributors to the uncertainty in efficiency.

NASA compressor

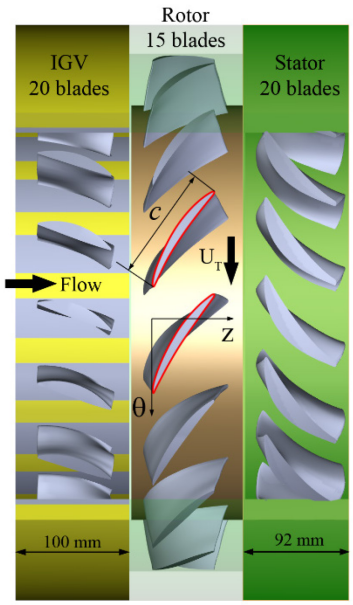

Figure 2-2 Configuration of the one and a half stages NASA compressor

Table 2-1 NASA compressor relevant geometric parameters

Casing diameter (D) (mm)	457.2
Hub radius (r_{hub}) (mm)	182.9
Rotor passage height (L) (mm)	45.7
Rotor diameter (D_R) (mm)	453.6
Rotor blade chord (c) (mm)	102.6
Rotor blade span (H) (mm)	43.9
Rotor blade stagger angle (γ) (deg)	58.6
Rotor blade axial chord (c_A) (mm)	53.5
Measured tip clearance (h) (mm)	1.8 (0.0175c or 0.041H)
Axial casing groove diameter (mm)	34.8
Groove skew angle (deg)	45
Total number of grooves	60
Shaft speed (Ω) (rad s^{-1}) {RPM}	50.27 {480}
Rotor blade tip speed (U_T) (m s^{-1})	11.47
Reynolds number ($U_T c / \nu$)	1.07×10^6

As described in Hah *et al.*, (2014) and shown in Figure 2-2, the blades of this one and a half stages axial turbomachine are based on the first one and a half stages of the low-speed axial compressor (LSAC) facility at NASA Glenn. However, while maintaining the same blade profiles, their aspect ratio has been modified to maintain a minimum thickness required for using acrylic

blades in a liquid turbomachine. As shown in Figure 2-2, the setup consists of a 20-blade inlet guide vane (IGV), a 15-blade rotor and a 20-blade stator. The top nine IGV and stator blades, and all fifteen rotor blades are made of acrylic. The rest of the IGV blades are made of naval bronze, and they support the entire hub of the machine. The surfaces of the acrylic and the bronze blades are all polished, ensuring that the roughness height is in the submicron range. The casing is also made of acrylic with flat exterior surfaces to accommodate PIV measurements. Relevant dimensions are provided in Table 2-1. For the present measurements, the nominal tip gap is 1.8mm or 1.75% of the blade span. However, the tip gap, 2.4mm, measured directly from the PIV images in Chapter 3, is slightly larger, most likely due to slight differences in rotor eccentricity. This problem is fixed for other experiments as the measured tip gap matches the nominal value of 1.8mm.

All experiments for this machine are carried out at 480 RPM. The static pressure rise across the pump is measured using pressure taps located upstream of the IGV and downstream of the stator. Each pressure tap is connected to two circumferentially distributed pressure ports to compensate for circumferential pressure variations in the inlet and outlet planes. The normalized static-to-static (ψ_{SS}) and total-to-static (ψ_{TS}) pressure coefficients are defined as

$$\psi_{SS}=(p_{exit}-p_{in})/(0.5\rho U_T^2) \tag{2.1}$$

$$\psi_{TS}=(p_{exit}-p_{0i})/(0.5\rho U_T^2) \tag{2.2}$$

Here, P_{exit} is the pressure measured downstream of the stator. p_{in} and p_{0i} are the static and total pressure measured upstream of the IGV, respectively. The volumetric flow rate is measured by integrating the velocity profile obtained by translating a Pitot tube across the pipe in the return line. Thirteen equally-spaced measurement points, starting from the centerline, with 12.7mm intervals, are used for mapping the velocity distributions in the pipe. The flow rate coefficient is

$$\varphi=V_Z/U_T \tag{2.3}$$

where V_Z is the volumetric flow rate divided by the annular area (A_T) of the rotor passage

AxWJ-2 waterjet pump

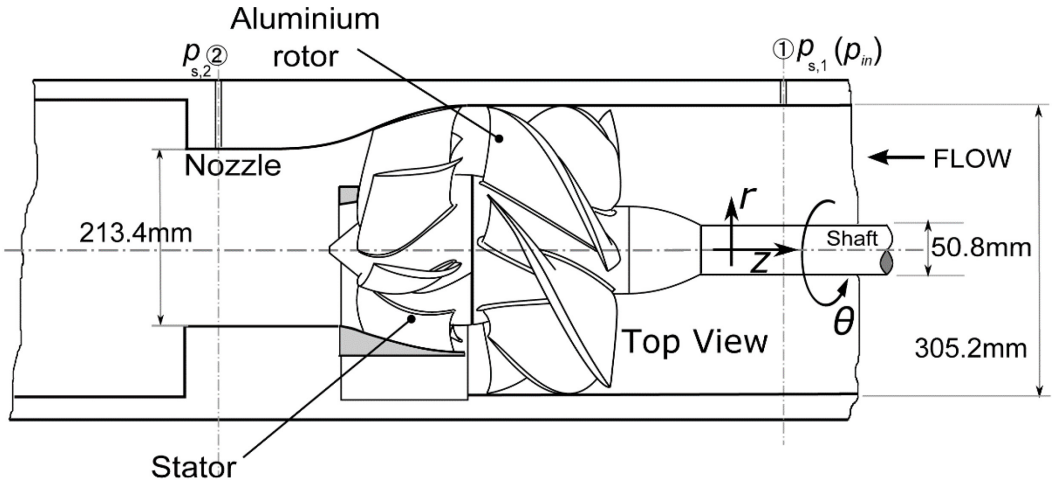

Figure 2-3 The AxWJ-2 waterjet pump

Table 2-2 AxWJ-2 waterjet pump relevant geometric data

Number of rotor blades	6
Number of stator blades	8
Tip profile chord length c	274.3mm
Tip profile axial chord length c_A	127.4mm
Rotor diameter D_R	303.8mm
Rotor radius R_r	151.9mm
Casing diameter D_1	305.2mm
Casing radius R	152.6mm
Outflow section diameter D_2	213.4mm
Pump inner diameter D	304.8mm
Tip clearance h	0.7mm
Tip clearance ratio $2hD^{-1}$	4.6×10^{-3}
Tip profile pitch ζ	159.1mm
Tip profile solidity $c\zeta^{-1}$	1.72
Tip profile stagger angle γ	27.7º
Rotor angular velocity Ω (n)	94.2rad s^{-1} (900rpm)
Tip speed U_T	14.3ms^{-1}
Tip profile Reynolds number Re_c	3.6×10^{6}

The axial waterjet pump, AxWJ-2, used in the current study has been designed by Michael *et al.*, (2008). To delay thrust breakdown, the pressure distribution on the SS is set to be nearly constant at design conditions. Tests performed by Chesnakas *et al.*, (2009) on AxWJ-2 show good agreements with the performance predictions. Detailed descriptions of this pump and cavitation

phenomena occurring in it can be found in Chesnakas et al. (2009), Michael et al. (2008), and Tan et al. (2012, 2015). Relevant geometric parameters of this machine are listed in Table 2-2, and a sketch of it is provided in Figure 2-2. Briefly, AxWJ-2 has 6 rotor blades and an inlet diameter of 305.2 mm. The rotor tip chord length is 274.3mm. The stator downstream of the rotor has 8 blades with a hub chord length of 121.5mm. The directly measured tip gap when the pump is installed in the JHU refractive index matched facility is 0.7mm. For the present study, we use the very same rotor that Chesnakas *et al.* (2009) used during their tests. Based on their findings, the efficiency of this pump peaks at 89% when the flow rate coefficient of the pump, defined as

$$\varphi_P = \frac{Q}{nD^3} \tag{2.4}$$

is φ=0.76. Here, Q is the volumetric flow rate, n is the rotor angular speed in revolutions per second, and D is the diameter of the inlet. The subscript "P" differentiates the variable definition from that for the NASA compressor. The total head rise coefficient is defined as

$$\psi_P = \frac{p_{S,2} - p_{S,1} + \frac{\rho}{2}\left[\left(\frac{Q}{A_2}\right)^2 - \left(\frac{Q}{A_1}\right)^2\right]}{\rho n^2 D^2} \tag{2.5}$$

where, as illustrated in Figure 2-3, the subscripts 1 and 2 refer to the planes where the pressure taps are located, A is the through-flow area and p_s is the measured static pressure. The static head rise, $\Delta p_S = p_{s,2} - p_{s,1}$, is measured directly by a differential pressure transducer connected to the pressure taps. To account for the variations of the flow downstream of the stator, $p_{s,2}$ is the average reading of five circumferentially distributed pressure ports.

2.2 Cavitation visualization

Cavitation, which is used for visualizing vortical structures due to the low pressure in their cores (Arndt, 2002), is induced by reducing the mean pressure in the facility. The visualization

experiments have been performed numerous times at varying pressures, first to confirm that the occurrence and behavior of observed vortices are repeatable, and second, to verify that they are not affected, generated or caused by the cavitation. The vortices appear consistently in all the experiments and varying the pressure only changes the concentration of bubbles in the vortices, but not their location and behavior. Furthermore, in (Tan *et al.*, 2015b), we compare the location of the TLV seen in the visualizations with that obtained in the PIV measurements. There is full agreement between them. All the PIV measurements are performed at higher pressure when cavitation is suppressed.

A commonly used cavitation visualization setup is shown in Figure 2-4 for the NASA compressor. Two continuous halogen lamps are placed at both sides of the pump and illuminate the tip region of the rotor passage. The PCO. dimax high-speed camera has a CMOS sensor of 2016×2016 pixels, but only parts of the pixels are recorded to boost the acquisition rate to 2400-5760 frames/s, corresponding to 20-48 images per blade passage period. The field of view is on the order of 100×100 mm^2. The raw images are enhanced by subtracting the background and applying histogram modification algorithms. Different experiments may use a slightly different setup, which will be described in the corresponding Chapters.

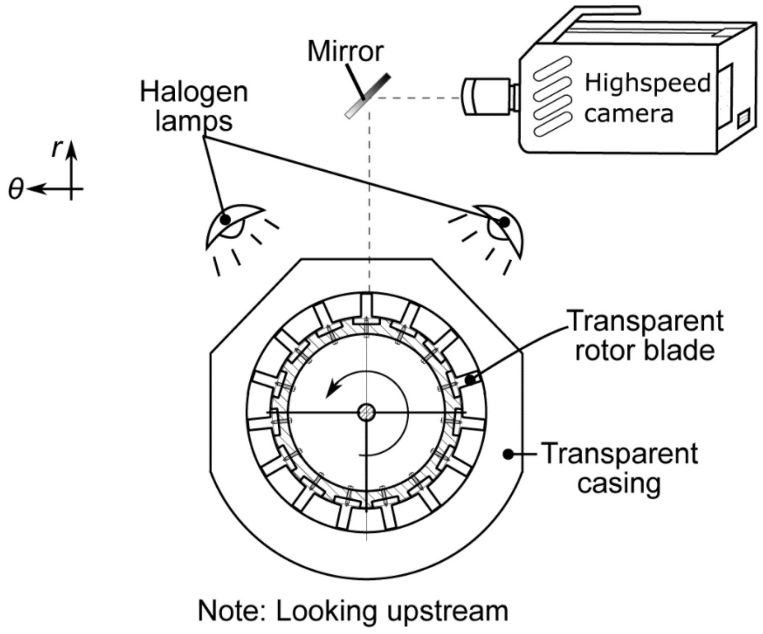

Figure 2-4 Cavitation flow visualization setup

2.3 PIV setup and data processing

Most of the PIV experiment carried out in the current study is SPIV, which gives us 3D velocity data in a 2D plane. Most of the time we are looking at pump meridional planes. A typical SPIV setup for NASA compressor is shown in Figure 2-5a. The flow field is illuminated by a dual head, 200mJ/pulse, Nd:YAG laser whose beam is expanded to a laser sheet with a thickness of less than 1mm, which illuminates meridional planes intersecting the rotor blade at different chord fractions. The delay between pulses is set between 20-40μs. The flow is seeded with 13μm, silver coated hollow spherical glass particles that have a specific gravity of 1.6, which is slightly lower than that of the fluid. A pair of PCO© 2000, interline transfer cameras with resolutions of 2048×2048 pixels are mounted on different sides of the laser sheet. To obtain higher resolutions, a pair of Imperx B6640 CCD cameras that have 6600×4400 pixel arrays are sometimes used. Each camera is equipped with a 105mm macro lens mounted on a Scheimpflug adaptor to satisfy the imaging conditions. To reduce image distortion and multiple reflections, the sample area is viewed

through an acrylic prism whose external surfaces are perpendicular to the optical axes of the lenses. Both cameras are mounted as a unit on a precision-controlled vertical motorized slide. Calibration is carried out following the two-step procedure described by Wieneke (2005). First, coarse calibration is performed based on images of a target immersed in a calibration chamber and filled with the same fluid, which is located above the compressor. Then, fine calibration is performed based on a series of particle images recorded within the sample volume. As illustrated in Figure 2-5b, SPIV measurements have been conducted over a series of meridional planes. The location of sample planes is defined as *s/c*, where *s* is the chordwise distance from the leading edge. The planes are usually chosen to follow the development of the TLV.

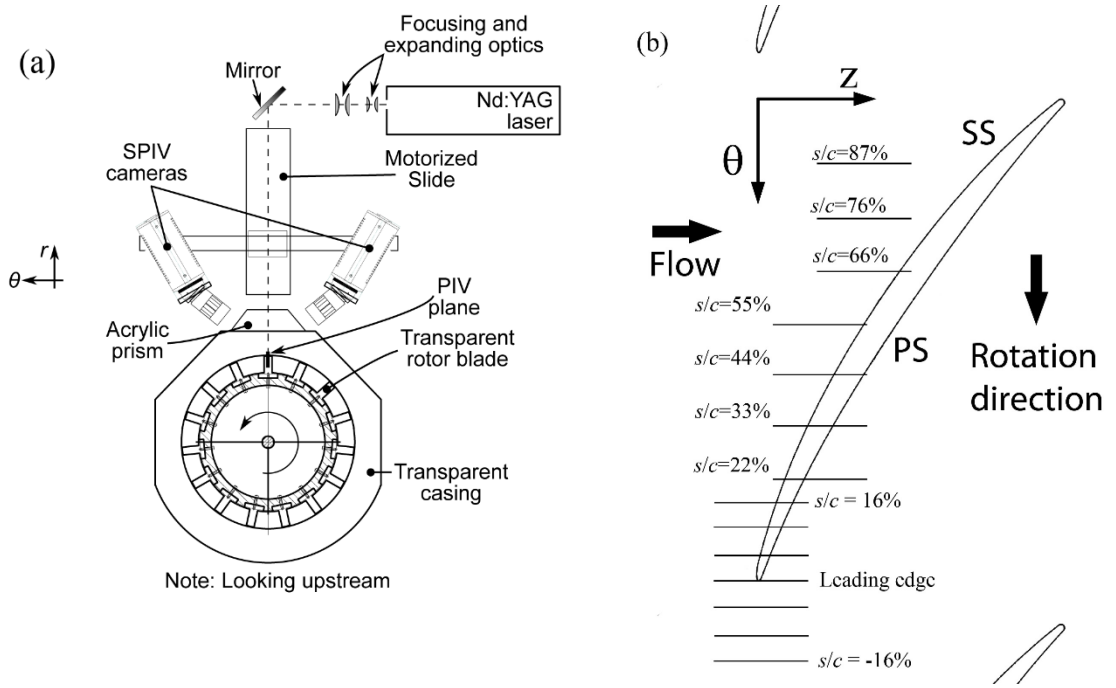

Figure 2-5 (a) SPIV setup in NASA compressor meridional planes. (b) Rotor blade tip profile with horizontal lines highlighting the SPIV measurement sample areas.

During analysis, the SPIV images are pre-processed, first by filtering out the background noise and image non-uniformities (Adrian *et al.*, 2011), and then enhanced by applying a modified histogram equalization algorithm (Roth *et al.*, 2001). Multi-pass FFT-based cross-correlations of image pairs are carried out using the LaVison© DaVis commercial software package. If 32×32

pixels final interrogation window is used with 50% overlap, the corresponding vector spacing is around 0.16-0.17mm in measurement planes. Universal outlier detector filters described by Westerweel *et al.* (2005) are adopted to reject bad vectors during vector post-processing. The uncertainty in instantaneous velocity is on the order of ~0.1 pixel as long as there are more than five particles within each interrogation window (Miorini *et al.*, 2012). The present results are presented in a cylindrical coordinate system with the origin located at the center of the machine, and the axial and circumferential directions coinciding with the rotor blade leading edge (Figure 2-2 and Figure 2-5b). The corresponding velocity components are u_z, u_r, u_θ, and are normalized by the rotor tip speed U_T throughout the thesis. Circumferential vorticity in the cylindrical coordinate system is defined as

$$\omega_\theta = \frac{\partial u_r}{\partial z} - \frac{\partial u_z}{\partial r} \tag{2.6}$$

Vorticity is normalized by the rotational speed of the machine (Ω in rad/s). Ensemble-averaged velocity components, denoted as U_i, are calculated by averaging all the data obtained for each phase. Velocity fluctuations are defined by $u_i' = u_i - U_i$, i.e. by deviation of the instantaneous data from the ensemble-averaged result. Normalized turbulent kinetic energy (TKE) is defined as

$$k^* = \frac{\overline{u_r' u_r'} + \overline{u_\theta' u_\theta'} + \overline{u_z' u_z'}}{2U_T^2} \tag{2.7}$$

A normalized radial coordinate defined as

$$r^* = (r - r_{hub}) / L \tag{2.8}$$

is used throughout this thesis. Here, L is the distance from the hub to the inner casing endwall. The coordinate starts at the rotor hub (r^*=0) and ends at the endwall casing (r^*=1).

Chapter 3 Visualizations of Flow Structures in the Rotor Passage of the NASA Compressor at the Onset of Stall

This Chapter examines flow phenomena developing in the rotor passage of the NASA compressor at the onset of stall. High-speed imaging of cavitation performed at low pressures qualitatively visualizes vortical structures. Stereoscopic particle image velocimetry measurements provide detailed snapshots and ensemble statistics of the flow in a series of meridional planes. At pre-stall condition, the tip leakage vortex (TLV) breaks up into widely distributed intermittent vortical structures shortly after rolling up. The most prominent instability involves the periodic formation of large scale backflow vortices (BFVs) that extend diagonally upstream, from the suction side of one blade at mid-chord to the pressure side near the leading edge of the next blade. The 3D vorticity distributions obtained from data recorded in closely-spaced planes show that the BFVs originate at the transition between the high circumferential velocity region below the TLV center and the main passage flow radially inward from it. When the BFVs penetrate to the next passage across the tip gap or by circumventing the leading edge, they trigger a similar phenomenon there, sustaining the process. Further reduction in flow rate into the stall range increases the number and size of the BFVs, and they regularly propagate upstream of the leading edge of the next blade, where they increase the incidence angle in the tip corner. As this process proliferates circumferentially, the BFVs rotate with the blades, indicating that there is very little through-flow across the tip region. This work was published in the *Journal of Turbomachinery* (Chen *et al.*, 2017c).

3.1 Experimental setup

The setup for cavitation visualization and SPIV are described in Chapter 2.

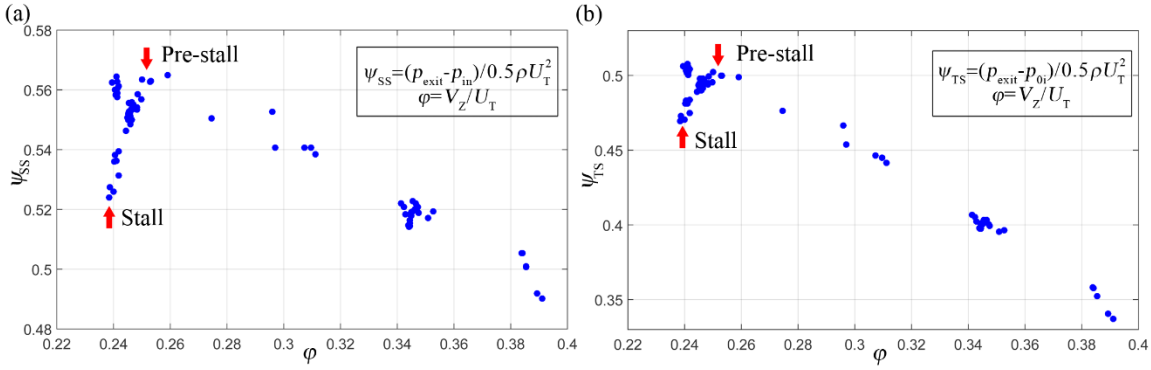

Figure 3-1 (a) Static-to-static and (b) total-to-static performance curves for NASA compressor at 480 RPM

The performance curves for the present tip gap is shown in Figure 3-1. The present Chapter discusses SPIV measurements and cavitation visualizations performed at pre-stall conditions, namely at φ=0.25. This point is chosen because it corresponds to the minimum possible stable operating flow rate. Further increase in pressure drop in the loop causes substantial fluctuations in performance. The performance curves shown in Figure 3-1 includes all the data points obtained while operating the facility at fixed resistance and speed instead of continuously logging the pressure and flow rate as the compressor is throttled into stall, as suggested by Day (2015). As φ is reduced below 0.25, there is a certain narrow range ($0.24<\varphi<0.242$) for which we sometimes observe further increase in pressure, and at other times, there is a sharp decrease in ψ accompanied by an audible increase in noise and blade vibrations visible to a naked eye. We opt to include all data points. Once φ is reduced below 0.24, the noise and vibrations as well as the decrease in ψ_{SS} below 0.53 persist. Hence, we use φ=0.24 as a representative for early stall conditions. Cavitation visualizations have been performed at both φ=0.25 (and ψ_{SS}=0.56), and φ=0.24 (and ψ_{SS}=0.53). As recommended by Day (2015), Figure 3-1b shows the performance in

terms of total-to-static pressure coefficient (ψ_{TS}) as a better means of characterizing the performance slope near stall conditions. In this plot, the presently selected pre-stall condition resides slightly to the right of the peak ψ_{TS} point, namely when the performance curve still has a negative slope. As discussed later, this observation is included in the discussion about the type of stall occurring under this condition, following the criteria discussed in Camp *et al.* (1998).

We have not performed SPIV measurements under stall conditions, in great part out of concern for the ability of the acrylic blades to withstand the unsteady loads and vibrations for prolonged periods. However, the flow visualizations described in this study indicate that there is considerable similarity between flow instabilities under pre-stall and stall conditions. Hence, the measurements at φ=0.25 provide ample data for characterizing flow instabilities involved with the onset of stall.

3.2 Results and discussion

Mean flow characteristics

Sample ensemble-averaged circumferential vorticity ($<\omega_\theta>$) and velocity (U_θ) obtained at pre-stall conditions, φ=0.25, are shown in Figure 3-2. The three blade phases are chosen to follow the TLV development, from the vicinity of the leading edge, mid-chord and aft parts of the rotor passage as a baseline for subsequent discussions. At s/c=0.16, the TLV is in its early stage of development, but there is already a strong backward leakage flow across the tip gap, from the PS to the SS of the blade. It meets the main passage flow at z/c=−0.03, located upstream of the plane of the blade leading edge, creating a local stagnation point there (not shown). The average vorticity peaks around the TLV center and around the PS tip corner. However, it should be noted that in instantaneous 'snapshots' of the flow, the vicinity of the TLV center contains multiple interlacing vortex filaments that never merge into a distinct vortex, as demonstrated by the sample in Figure 3-3 and in previous studies involving several turbomachines and operating conditions (Miorini *et al.*, 2012; Tan *et al.*, 2015b; Wu *et al.*, 2011a, 2011b, 2012). Figure 3-3 also serves as a baseline

image of the flow around an un-stalled blade tip. At s/c=0.33, the TLV grows in size and detaches from the blade, but remains connected to the SS tip by a shear layer that keeps on feeding vorticity into it. At s/c=0.76, the average peak vorticity magnitude within the TLV is substantially lower than that in previous planes, but it is spread over a large area. As discussed in (Tan *et al.*, 2015b) for the same condition, as well as reported in previous studies (Furukawa *et al.*, 1998; Miorini *et al.*, 2012; Schrapp *et al.*, 2004; Tan *et al.*, 2015b; Wu *et al.*, 2011a, 2011b, 2012; Yamada *et al.*, 2004), this rapid expansion is caused by bursting/breakup of the TLV. When it occurs, presumably because of adverse pressure gradients in the aft parts of the passage and migration to the PS side of the next blade, the vortex filaments become randomly scattered over an area that covers a substantial fraction of the passage.

Two distinct areas with elevated U_θ are evident in the distribution presented in Figure 3-2b, d & f. The first broad area is located on the PS of the blade, and the second is centered radially inward (under) and slightly upstream of the TLV. These high U_θ regions contain fluid moving in the same circumferential direction as the blade. Combined with the low values of U_z there, especially to the left of and immediately under the TLV, the velocity distributions indicate that substantial fractions of the tip region are blocked. The size and the magnitude $<u_\theta>$ under the TLV grow substantially with increasing chord fraction (and with decreasing flow rate – see (Li *et al.*, 2016)), especially after vortex breakup. In fact, the high circumferential velocity on the PS in Figure 3-2b & d is associated with migration of the TLV generated by the previous/adjacent blade to the pressure side of this blade. This phenomenon has also been reported by previous experimental studies (Tan *et al.*, 2015a; Wu *et al.*, 2011b; Yu *et al.*, 2007). It is caused by entrainment of fluid originating from the tip gap, which attains the blade circumferential momentum. It is also affected by exposure to adverse pressure gradients during its propagation in the passage to the PS of the next blade. As will be shown later, the formation of high U_θ zones in the tip region plays a role in processes affecting the onset of stall.

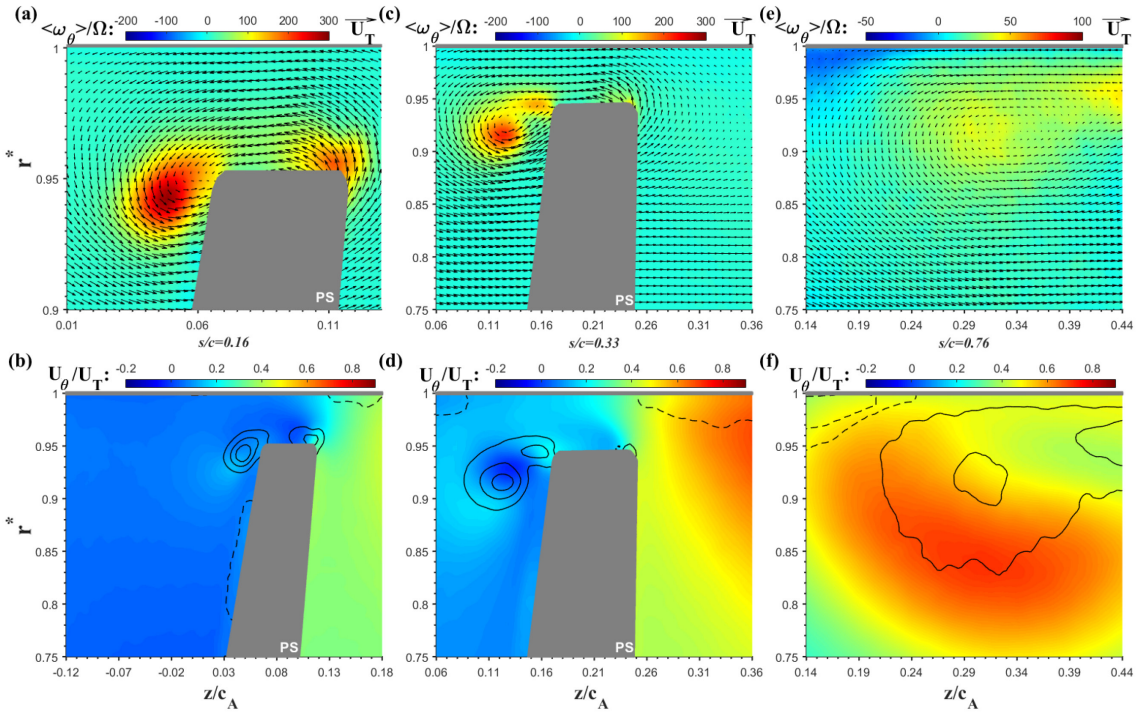

Figure 3-2 Ensemble-averaged color contours of $<\omega_\theta>$ (top row) and U_θ (bottom row) at: (a, b) s/c=0.16, (c, d) s/c=0.33, and (e, f) s/c=0.76. Lines in (b, d&f) are contours of $<\omega_\theta>$, with dashed lines indicating negative values. Vectors in (a) are shown in full resolution for part of the sample area. In (c, e), vectors are diluted by 2:1 axially and 2:1 radially for clarity. Note the differences in the vorticity scales. A reference vector showing the tip speed is provided on top. Horizontal axis is the streamwise direction while vertical axis is the radial direction. Other plots of SPIV results follow the same convention.

Sample distributions of turbulent kinetic energy (TKE), are shown in Figure 3-4. They are presented to highlight the regions of high flow instabilities, especially under pre-stall conditions. To demonstrate the associated enormous increase in turbulence, Figure 3-4d shows the distribution of TKE s/c=0.33 for φ=0.35, at the same location as Figure 3-4b, for which results have to be presented at a significantly different color scale to be visible. For all the cases corresponding to φ=0.25, the TKE is high around the TLV center, to a substantial part due to fluctuations in the distributions of vortex filaments around the mean core. Once bursting occurs (Figure 3-4c), the

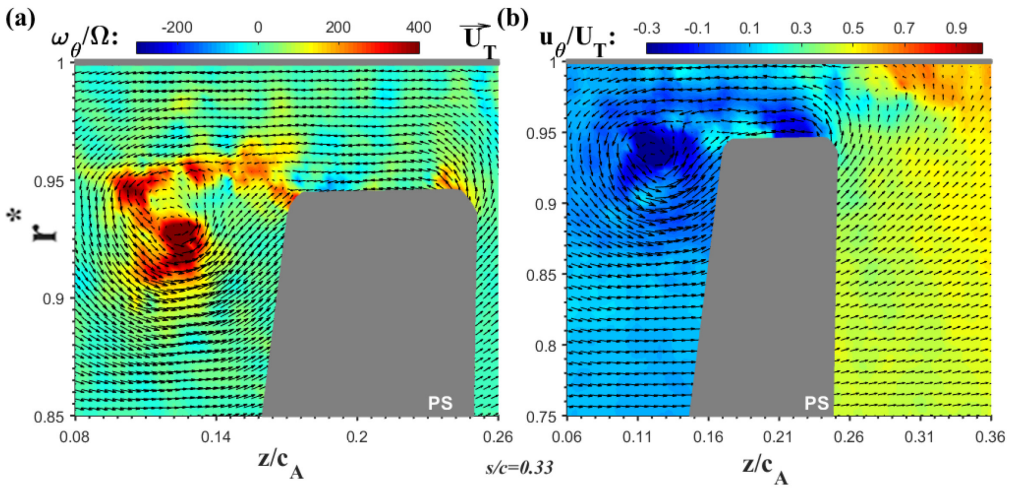

Figure 3-3 A sample instantaneous realization of (a) ω_θ and (b) u_θ at s/c=0.33, representing conditions when the blade tip is not stalled. Vectors in (b) are diluted by 2:1 axially and 2:1 radially. Note the differences in scales.

high TKE area grows substantially, occupying a large fraction of the rotor passage, all the way to the PS of the adjacent blade (Figure 3-4a&b). Other large scale flow instabilities, which affect the onset of stall are also involved, as described in the next section. At s/c=0.33 (and to a lesser extent also at s/c=0.16), the TLV turbulence on the PS is ingested to the SS of the blade through the tip gap, affecting the flow stability there. This plot provides statistical evidence demonstrating the crosstalk among passages, which is facilitated by tip leakage flow across the relatively wide clearance of the present configuration. Such interactions are minimal for narrow gaps, e.g., for h/c=0.5% (Li *et al.*, 2016). This crosstalk contributes to the development of instabilities on the SS side of the machine prior to stall. The resulting substantial decrease in flow stability is demonstrated by the comparison between in Figure 3-4b&d At φ=0.35, secondary structures associated with the previous TLV arrive at the next blade much further downstream in the rotor passage, and have much less impact on the flow stability.

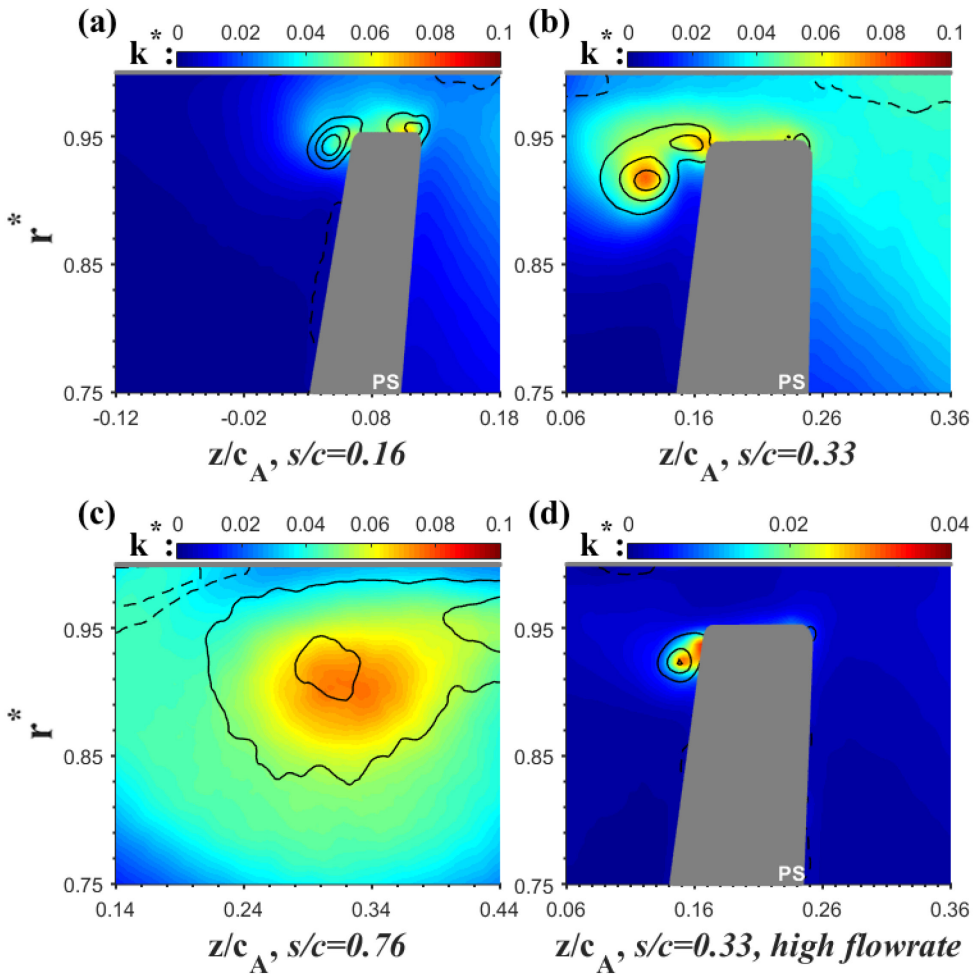

Figure 3-4 Color contours of the TKE at (a) s/c=0.16, (b) s/c=0.33, and (c) s/c=0.76 at φ=0.25. (d) TKE at φ=0.35 and s/c=0.33, the same location as (b), aimed at highlighting differences between them. Note the differences in scale. Lines are the contour of $\langle\omega_\theta\rangle$, with dashed lines indicating negative values.

Visualization of flow structures at pre-stall conditions

A time sequence of high-speed images demonstrating the evolution of vortical structures in the rotor passage is presented in Figure 3-5. Here, the time is normalized by blade passage period

$$t^* = (t - t_0) / (2\pi/15\Omega) \tag{3.1}$$

The TLV rolls up very near the tip of the leading edge but quickly breaks down into a series of secondary structures (Figure 3-5a). More interestingly, apart from the TLV, another vortical structure aligned perpendicularly to the blade develops and propagates from the leading edge to mid-chord. Arrows of the same style highlight its location in different frames.

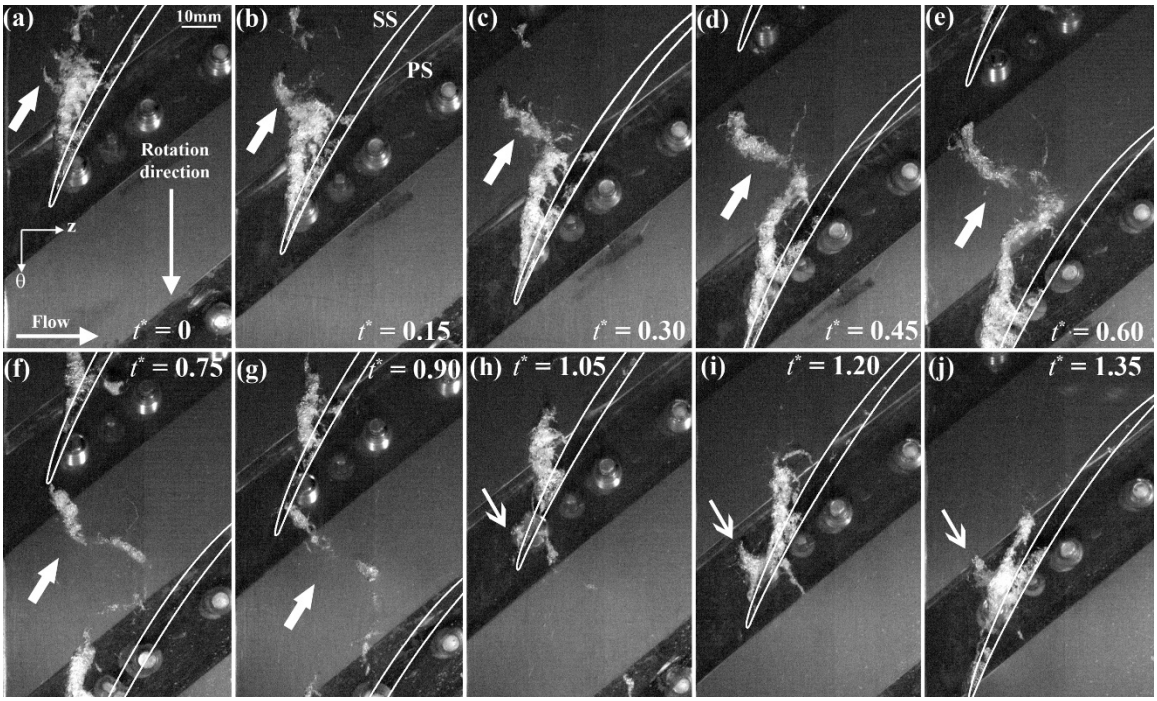

Figure 3-5 A time sequence of cavitation images showing the propagation of vortical structures at pre-stall conditions. Arrows of same styles follow the evolution of the same backflow vortex. White lines indicate the blade tip profile.

At t^*=0, a vortex starts as a small filament under the TLV near the blade leading edge. As it migrates downstream, this structure increases in length, with one end just about following the tail of the TLV, and the other extending diagonally upstream while getting closer in time to the leading edge of the next blade. The rotation direction of this vortex, determined by following vortical structures in time in the high-speed movies of cavitation, is that the vorticity points at the SS of the originating blade. This direction is also consistent with the SPIV data discussed later. Because of its orientation, and terminology used in prior studies detecting similar structures in

other turbomachines (Yamamoto *et al.* (2009); Yamanishi *et al.* (2007); Yokota *et al.* (1999), details follow), we refer to this structure as a backflow vortex or BFV. As it grows, the orientation of the BFV diagonally upstream does not change significantly. Since this vortex is largely transported with the blade circumferentially, and its outward end remains at nearly the same axial plane (z~0), it implies that there is very little through-flow in the tip region. At t^*=0.45 (Figure 3-5d), the vortex seems to be strong enough to alter the trajectory of the end of the TLV. At t^*=0.75, the upstream end of the vortex reaches the leading edge of the next blade, and at t^*=0.9 its end penetrates the tip gap. Additional evidence recorded at a different time that the vortex extends across the tip gap is provided in Figure 3-6b at a higher magnification. At t^*=1.05 (Figure 3-5h), the backflow vortex (or structures associated with it) appears to be split by the blade into two sections, leaving a short segment, which is marked by another arrow, on the suction side. Subsequently, as Figure 3-5i&j show, this segment grows and forms a structure that appears to be quite similar to that shown in Figure 3-5a. Indeed, at later times (not shown), this vortex continues to grow and propagates to the next blade, following a sequence that is very similar to that presented in Figure 3-5a-i. Based on examination of the movies (including the sample shown), the phase speed of what appears to be a circumferentially propagating periodic pattern is slower than the blade rotational speed by about 30%-40%. By comparing the locations of initial TLV rollup in Figure 3-6a&b, it is evident that rollup of the TLV is delayed when the upstream end of the backflow vortex arrives at the leading edge of the next blade or crosses the tip gap. Such a change indicates a considerable shift in the distribution of blade loading. In addition, when SS end of this vortex reaches trailing part of the TLV, it appears to be sufficiently powerful to disrupt the development of TLV (Figure 3-5d&e). Hence, development and propagation of the vortex cause sub-synchronous rotating disruption to both the blade performance and the entire flow in the rotor passage. Both are phenomena associated either with the inception of rotating stall or rotating instabilities discussed in (Day, 2015; Mailach *et al.*, 2001; März *et al.*, 2002; Mathioudakis *et al.*, 1985; Young *et al.*, 2012).

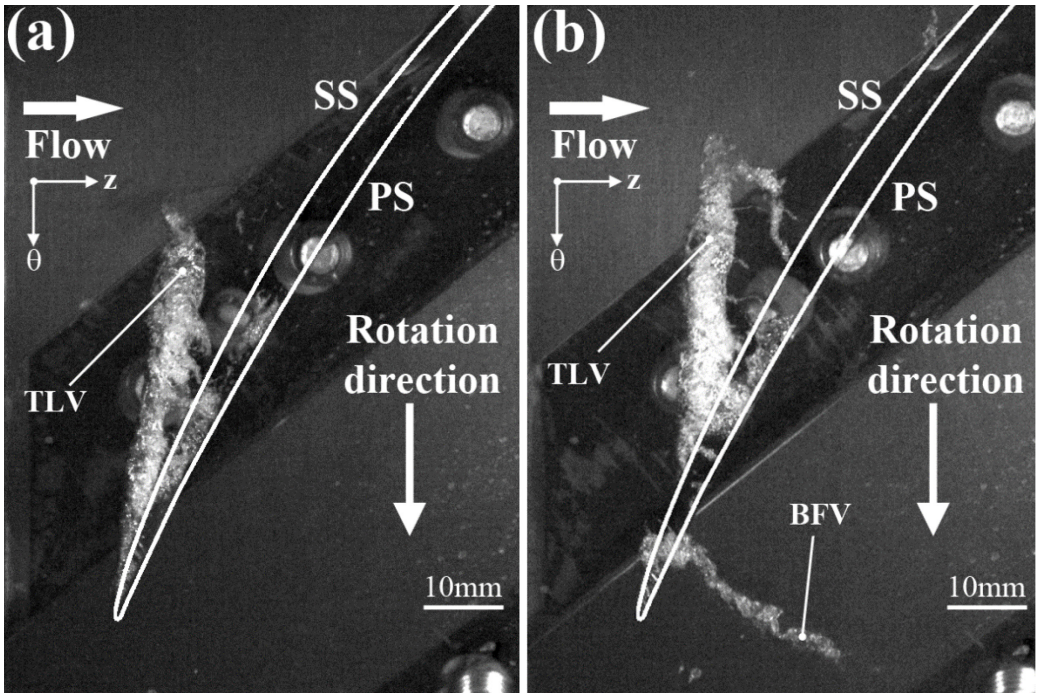

Figure 3-6 Sample cavitation images showing (a) TLV without the influence of the backflow vortex and (b) the backflow vortex propagating across the tip gap

The origin of a backflow vortex

The observations described above raise a question of where does the BFV come from, and what is the origin of its vorticity. Since during early phases of development, the vortex appears to protrude diagonally upstream from under the TLV and recalling that there is a region of elevated U_θ below TLV, one questions whether they are related. Selecting s/c=44% for further discussion, this relationship is elucidated by examining the 3D ensemble-averaged velocity and vorticity distributions in the tip region. First, the distributions of U_θ, U_z and U_r are shown in Figure 3-7(a-c), and the velocity diagram is shown in Figure 3-7d. Two points are selected as representatives, the first from the high U_θ region under the TLV (A) and the second from the low U_θ, but high U_z region below the area influenced by the tip leakage (B). Corresponding values of U_θ and U_z are tabulated and illustrated in Figure 3-7d, along with the projection of the relative velocity between B and A in the z-θ plane, The relative velocity $U_{\text{B-A}}$, which is indicated by the red arrow, is nearly

parallel to the blade chord. Hence, if the shear layer under the high U_θ region rolls up into a vortex due to some perturbation, the primary vorticity direction would be nearly perpendicular to the blade chord, as indicated by the direction of ω_{BFV}. This conceptual, but data-based, discussion is consistent with the direction and orientation of the BFVs in Figure 3-5 and Figure 3-6. The large upstream propagating vortex might originate from roll-up of the shear layer located at the interface between the high U_θ region (TLV induced blockage) and the through-flow under it.

Further evidence is provided by the sample average three-dimensional vorticity distributions in Figure 3-7(e-h). To determine the ensemble-averaged derivatives of velocity in the circumferential direction ($\partial/\partial\theta$) required for calculating the 3D vorticity components, we have recorded data in eleven closely spaced meridional planes, which are separated by an angular distance of 3.6×10^{-4} rad. The corresponding circumferential distance between planes is 0.081mm at the casing and 0.073mm at the bottom of the field of view, namely it is smaller than the in-plane vector spacing. In each plane, 2500 realizations are ensemble-averaged to obtain the distributions of all three velocity components, like the rest of the data. Using 2nd order finite differencing, the vorticity components involving out-of-plane derivatives are obtained from

$$\omega_z = \frac{1}{r}\frac{\partial}{\partial r}(ru_\theta) - \frac{1}{r}\frac{\partial u_r}{\partial \theta} \tag{3.2}$$

$$\omega_r = \frac{1}{r}\frac{\partial u_z}{\partial \theta} - \frac{\partial u_\theta}{\partial z} \tag{3.3}$$

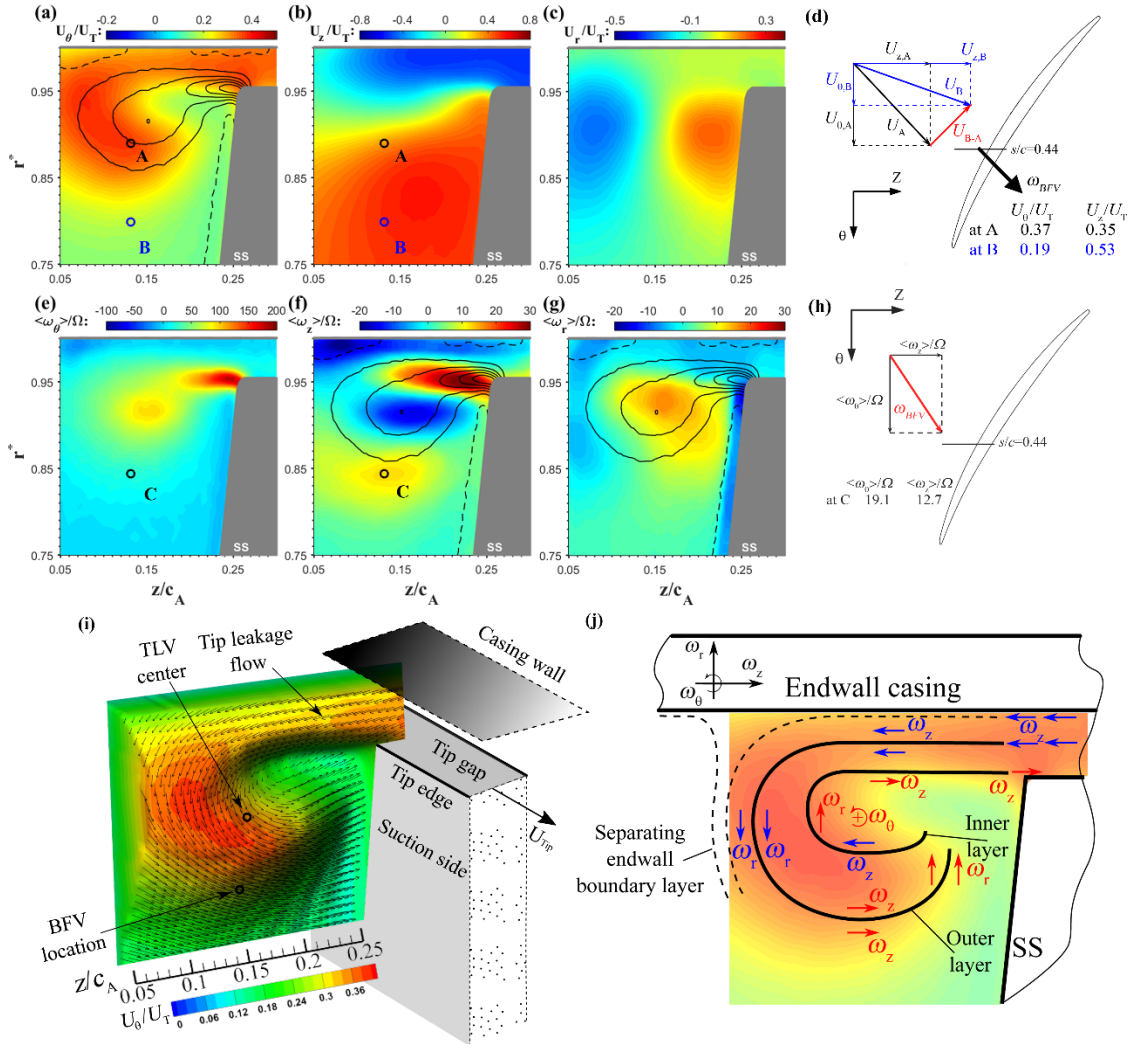

Figure 3-7 Ensemble-averaged three-dimensional velocity and vorticity distributions in the meridional plane at s/c=0.44 and φ=0.25. (a, b&c) Plots of U_θ, U_z and U_r. (d) Velocity diagram for points A and B, explaining the orientation of the BFVs. (e, f&g) Distributions of $<\omega_\theta>$, $<\omega_z>$ and $<\omega_r>$. (h) Vorticity diagram for point C, explaining the direction of the BFVs. (i) Perspective view of circumferential velocity distribution with three-dimensional velocity vectors. The elevation of the protruding surface is proportional to U_θ. Vectors are diluted by 2:1 axially and radially. (j) Sketch of vortical layers originating from the tip gap and surrounding the TLV. The background is the U_θ color contour. Lines in (a, f&g) are contours of $<\omega_\theta>$, with dashed lines indicating negative values.

To improve the data quality, we use the data from all 11 planes, by circumferentially averaging vorticity distributions calculated from planes 1 and 3, planes 2 and 4, planes 3 and 5, and so on. Figure 3-7(e-g) show the resulting distributions of all three vorticity components at s/c=0.44, where $<\omega_\theta>$, the largest component, is based on the in-plane data. Compared with $<\omega_\theta>$ at s/c=0.33 shown in Figure 3-2c, the TLV is clearly larger, but the peak vorticity decreases, indicating the TLV has already started to burst. However, most important for the present discussion is the broad area of elevated $<\omega_z>$ centered around point (C) in Figure 3-7f. This region is located in the region of radial gradients in U_θ under the TLV, at the transition between the high U_θ zone surrounding the TLV and the main passage flow. The values of $<\omega_\theta>$ and $<\omega_z>$ in point (C) are tabulated in Figure 3-7h, along with a plot of the resulting projection of the vorticity in the z-θ plane. The orientation of the vorticity projection in the z-θ plane is consistent with the orientation of the BFV seen in the cavitation images in Figure 3-5 and Figure 3-6, and the velocity vectors in Figure 3-7d. The mean vorticity distributions indicate that the underlying flow phenomenon causing the formation of the BFV is the radial gradients in U_θ under the TLV, which persists along the entire blade. While mean vorticity in this region is substantially lower than $<\omega_\theta>$ near the TLV center, once the BFV rolls up intermittently and stretched by the strain field in the passage, the cavitation images suggest that its core vorticity becomes large (further discussion follows).

Figure 3-7f&g also show that the TLV center is located in a region of negative $<\omega_z>$, and the distribution of $<\omega_r>$ is also non-uniform, with both positive and negative regions. To explain the 3D flow structure that these patterns represent, Figure 3-7i provides a 3D depiction of the distribution of circumferential velocity, where the out of the plane protrusion is proportional to U_θ, and Figure 3-7j sketched the origin of vortical layers emerging from the tip gap superimposed on the distribution of U_θ. The magnitudes and directions of $<\omega_z>$ and $<\omega_r>$ coincide with radial and axial gradients in U_θ, respectively. These vortical regions are originated from the tip gap and could be elucidated as a combined effect of three layers (Figure 3-7j) with different vorticity

distributions. The inner layer starts at the SS tip corner and carries substantial circumferential vorticity directly into the TLV center. The associated $<\omega_z>$ is positive, consistent with the positive radial gradients in U_θ at the interface between the leakage flow and the passage flow under. As this layer is entrained by the TLV, the positive $<\omega_z>$ becomes positive $<\omega_r>$, then negative $<\omega_z>$. The second layer follows the other side of the elevated U_θ region, as it emerges from the tip gap. It starts as a negative $<\omega_z>$ in the tip gap, consistent with the radial decrease in U_θ between the blade and the endwall casing. As this layer circumvents the TLV, the negative $<\omega_z>$ becomes negative $<\omega_r>$ to the left of the TLV, positive $<\omega_z>$ under the TLV, and finally positive $<\omega_r>$ to the right of the TLV. The flow field has a third outer layer, which contains fluid originating from the endwall boundary layer. This layer separates from the endwall when the leakage flow meets (impinges on) the main passage flow. Only parts of this layer are shown on the right sides of the distributions presented in this Chapter (Li *et al.*, 2016; Tan *et al.*, 2015b; Wu *et al.*, 2011b), hence it is sketched using a dashed line in Figure 3-7j. This discussion suggests that the BFVs evident in the cavitation images originate from the outer layer of a "ring-like" vortical structure that surrounds the TLV. As discussed later, we have seen very similar multi-layer phenomena in other axial waterjet pumps (Wu *et al.*, 2011b). Hence, the flow structure illustrated in Figure 3-7j is not unique to the present compressor. Furthermore, the present depiction bears several similarities to the partial vortical ring surrounding the TLV and leading edge separation in (Pullan *et al.*, 2015; Yamada *et al.*, 2013), except that in their depiction, the layers connect to the endwall and the blade surface.

The present observations and conjectures are consistent with several prior studies. First, they agree with experimental and numerical studies focusing on the development of so-called BFVs in rocket inducers by Yamanishi *et al.* (2007) and Yokota *et al.* (2004). They show that in heavily loaded inducers, where the strong leakage flow extends upstream of the rotor ('backflow'), the BFVs are caused by the interaction of the swirling backflow and the forward flow under it. Although there are some differences in magnitudes, orientations and specific flow structures

involved, the origin of the present observed propagating/rotating instability is still interaction of the main passage flow with the region dominated by the leakage flow. Hence, we opt to also refer to the present phenomenon as "backflow vortex (BFV)", following Yamamoto *et al.* (2009); Yamanishi *et al.* (2007); and Yokota *et al.* (1999, 2004). Next, in previous measurements within a waterjet pump performed within this index-matched facility, SPIV data obtained in a series of closely-spaced parallel meridional planes, has also enabled calculation the ensemble-averaged 3D vorticity distribution (Wu *et al.*, 2011b). Results show a region of concentrated streamwise vorticity radially inward from the high U_θ region under the TLV. The associated vorticity magnitude, about 50% of the circumferential vorticity in the TLV core, is substantial, confirming the presence of a powerful shear layer there.

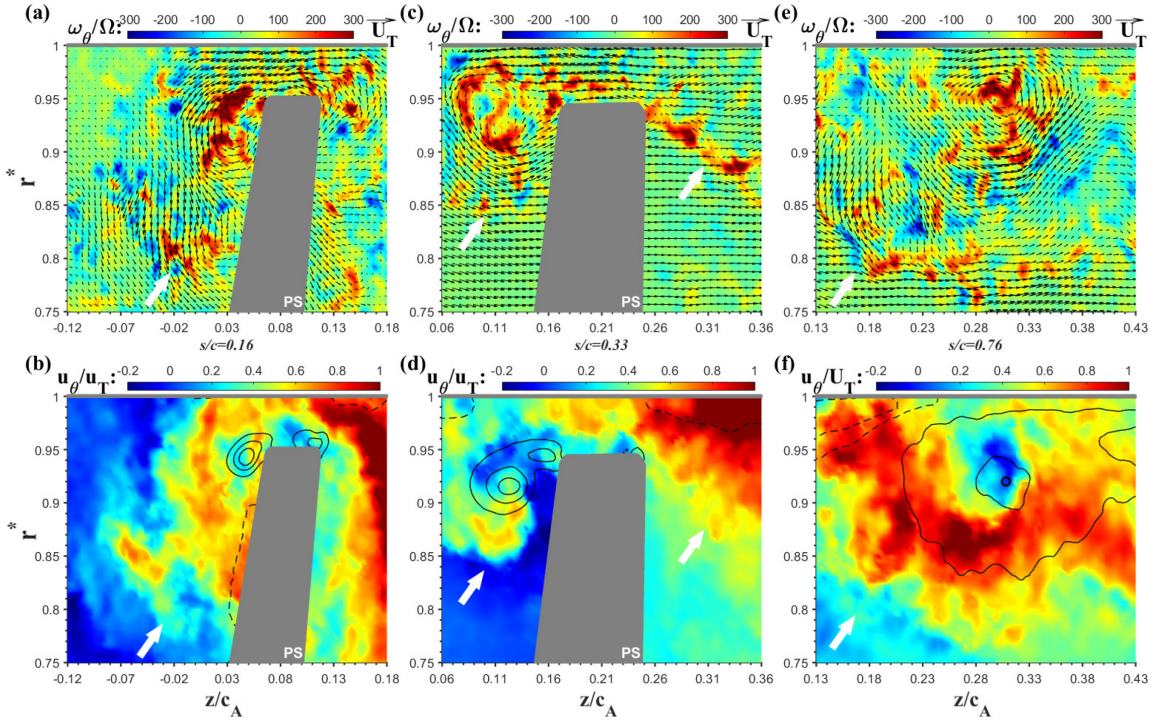

Figure 3-8 Samples of instantaneous realizations of $<\omega_\theta>$ (top row) and u_θ (bottom row) at (a, b) s/c=0.16, (c, d) s/c=0.33 and (e, f) s/c=0.76, when the BFVs interact with the adjacent blade. Vectors are diluted by 2:1 axially and 2:1 radially. Lines in (b, d&f) are contours of $<\omega_\theta>$, with dashed lines indicating negative values.

Since the present SPIV measurements only allow us to calculate the ensemble-averaged $<\omega_r>$ and $<\omega_z>$, and as the cavitation images show, the formation of the BFV is intermittent, it is difficult to discern its presence from the vorticity distributions in the relevant region (Figure 3-2 and Figure 3-7). However, since the BFV is aligned diagonally, snapshots of its signature and impact on the flow around the leading edge and tip gap should be readily seen in the part of the 2500 instantaneous realizations for each plane. Indeed they are! Selected instantaneous realizations of ω_θ and u_θ for the same s/c as Figure 3-2, are presented in Figure 3-8. In all three examples, regions of high u_θ that increase in size with s/c, wrap around the mean TLV center. At s/c=0.76, the layer appears to be connected to the endwall casing, but in plots showing the blade, the high u_θ zone originates from the tip gap. Outside of this region u_θ is small, indicating large radial and axial gradients in u_θ (depending on the orientation of the interface) at the interface between these area regions. It is possible that these gradients involve high axial and radial vorticity, respectively, as well. Furthermore, a series of distributed circumferential vortex fragments/filaments with high vorticity appear to be distributed along the boundary of the high u_θ region indicated by the arrows, clearly well below the TLV center. Combined with the analyses of ensemble-averaged results shown Figure 3-7, this picture strongly indicates that the BFV exists at the border of the high u_θ region and the main passage flow, and circles around the TLV. The instantaneous snapshots show that the underside of the high u_θ region contains multiple filaments distributed along the boundary of a flow domain jetting in the circumferential direction, essentially at the blade speed.

Moreover, Figure 3-8c&d show a series of elevated ω_θ regions coinciding with the underside of the high u_θ zone on the PS of the blade being entrained into the tip gap. As these BFVs crossed the gap, they interact with the TLV on the SS, causing the latter to deviate from its "normal" shape shown in Figure 3-3. In addition, the flow structure shows early signs that new BFVs begin to rollup into distinct vortices well below the TLV, at r^*~0.85, coinciding the lower boundary of the swirling high u_θ region. It appears that this snapshot corresponds to the phase at

which the upstream end of the BFV penetrates across the tip gap to the SS of the blade (Figure 3-5g&h and Figure 3-6b). Figure 3-8a&b is another example of the tip flow being disrupted by the BFV, this time at s/c=0.16. A strong backflow with high u_θ rushes through the tip gap to the SS, disrupting the TLV and generating a radially inward spiraling 'jet' that impinges on the blade surface. Such a flow structure differs significantly from the "normal" conditions depicted in Figure 3-2a. This violent flow disruption appears to cause the formation of a new BFV at r^*~0.8, well under the TLV, in the region of high u_θ gradients.

Before concluding this section, it should be noted that the intermittent formation of BFVs is not limited to the present setup that has a relatively wide tip gap. A series of such structures appear to form also under the high u_θ region of the same machine when the tip gap is narrow (h/c=0.5%), as demonstrated e.g., in Figure 3-8(h-g) in Tan *et al.* (2015b). However, the narrow tip gap seems to inhibit the penetration of structures across the tip gap, greatly reducing "cross-talk" between passages.

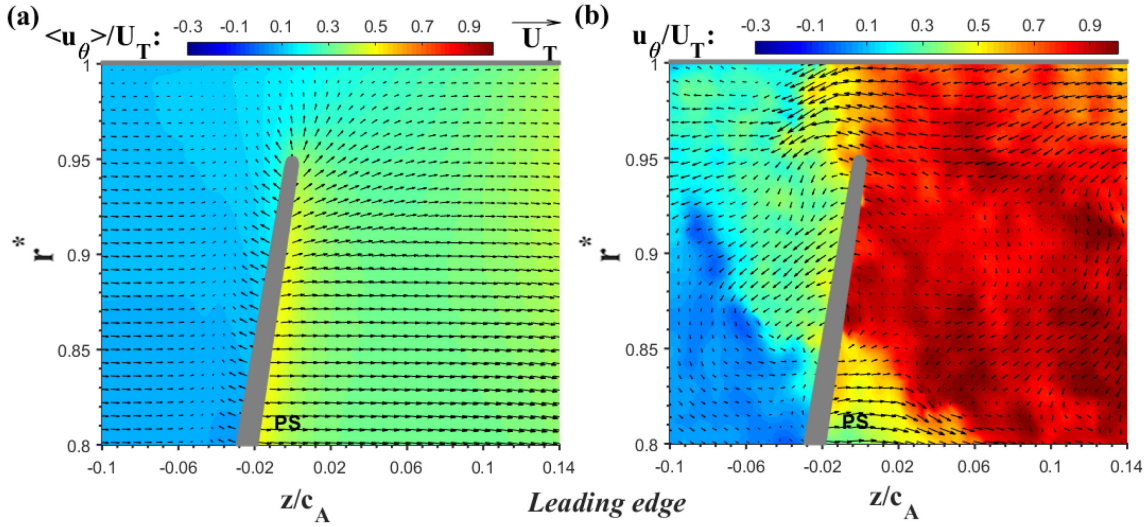

Figure 3-9 (a) U_θ and (b) an instantaneous sample u_θ at the leading edge at φ=0.25. Vectors are diluted by 2:1 axially and 2:1 radially.

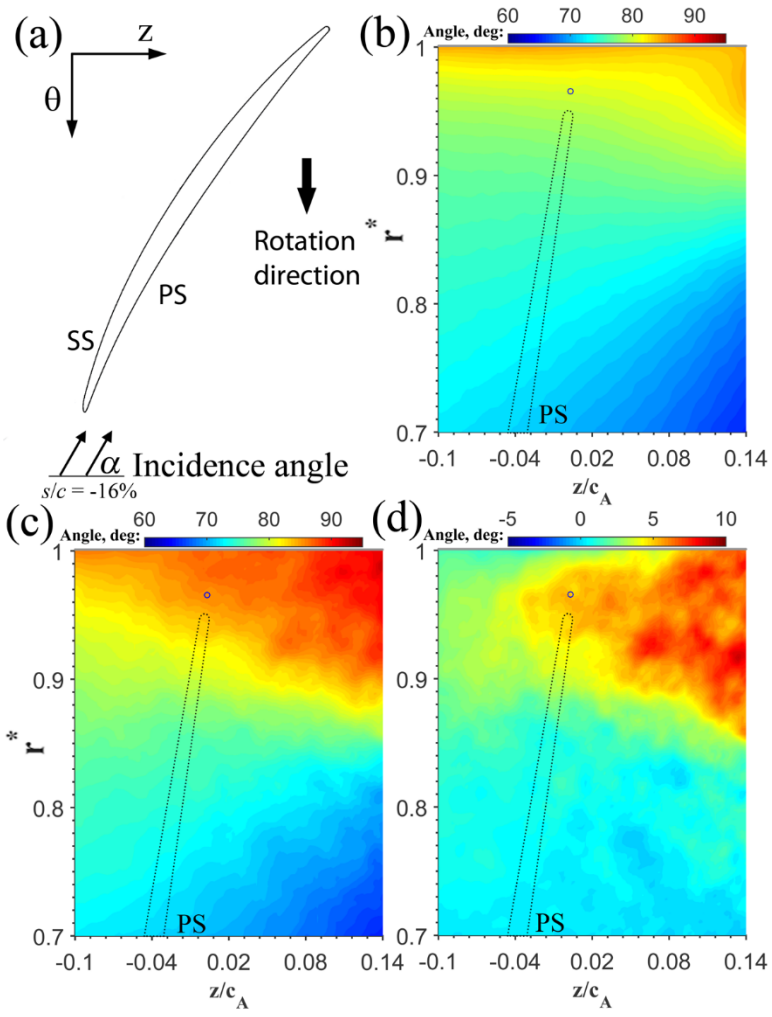

Figure 3-10 Relative incidence angles (angles relative to the meridional plane) at s/c=−0.16. (a) A sketch showing the definition of incidence angle. (b) Ensemble-averaged result of 2500 realizations. (c) Conditionally averaged result of 100 extreme cases when BFVs reaching near the LE. (d) The change in incidence angle. Dot line indicates the location of the leading edge. The circle indicates the location used for conditional sampling.

Finally, considering that the upstream end of the BFV makes it to the leading edge of the next blade, it would be of interest to conclude this part of the discussion by examining its impact on the flow there. The distribution of ensemble-averaged velocity for θ=0 and a sample snapshot of the flow when the BFV reaches the leading edge are presented in Figure 3-9. In the mean distribution, the leakage flow is minimal, and the magnitude of U_θ along the pressure side is

significant but mild. Conversely, in the selected instantaneous sample, u_θ over the entire PS is well above 80% of the tip speed, and there is a strong leakage flow, which brings fluid with elevated u_θ to the SS as well. Under the present pre-stall condition, such events are still quite intermittent; namely, they occur in 40 out of the 2500 realizations, using high U_θ rushing through the gap as a criterion. The high intermittency of this event is one of the indications that the presently described flow phenomena correspond to spike-type stall. Figure 3-10 demonstrates the impact of the BFV and the high u_θ zone on the incidence angle s/c=−0.16, just upstream of the rotor blade leading edge. Figure 3-10a shows the location of s/c=−0.16 relative to the blade and defines the angle relative to the meridional plane depicted in the other plots, where the intersection of the blade tip leading edge with the *r-z* plane is illustrated by the dashed line. Figure 3-10b presents the distribution of the ensemble-averaged angle based on the entire database. In contrast, Figure 3-10c shows the conditionally averaged angle using the criterion u_θ>0.29U_T at the point indicated by a circle, which would be located in the tip gap once the blade arrives. This condition corresponds to the 100 most extreme cases (out of 2500) of BFVs reaching the leading edge of the next blade. As is evident, the BFV and associated high u_θ region cause a significant increase to the tip region incidence angle. As plotted in Figure 3-10d, the increase in incidence angle around the leading edge of the blade tip and to the right of it falls in the 4° to 10° range. Hence, for heavily loaded blades, such a change in incidence might cause leading edge separation, which has been proposed before as a mechanism affecting the onset of stall (Pullan *et al.*, 2015; Yamada *et al.*, 2013). In addition to the changes in incidence angle, the increase in u_θ, namely a decrease in velocity relative to the blade, also affects the blade loading in the tip region. Consequently, as demonstrated in Figure 3-6, the BFV-induced flow disrupts and delays the TLV roll-up process. Figure 3-10d also show that the change to incidence angle (and decrease in relative velocity) are, for the most part, restricted to the tip region of the blade (r^*>0.8).

Visualization of flow structures at stall conditions

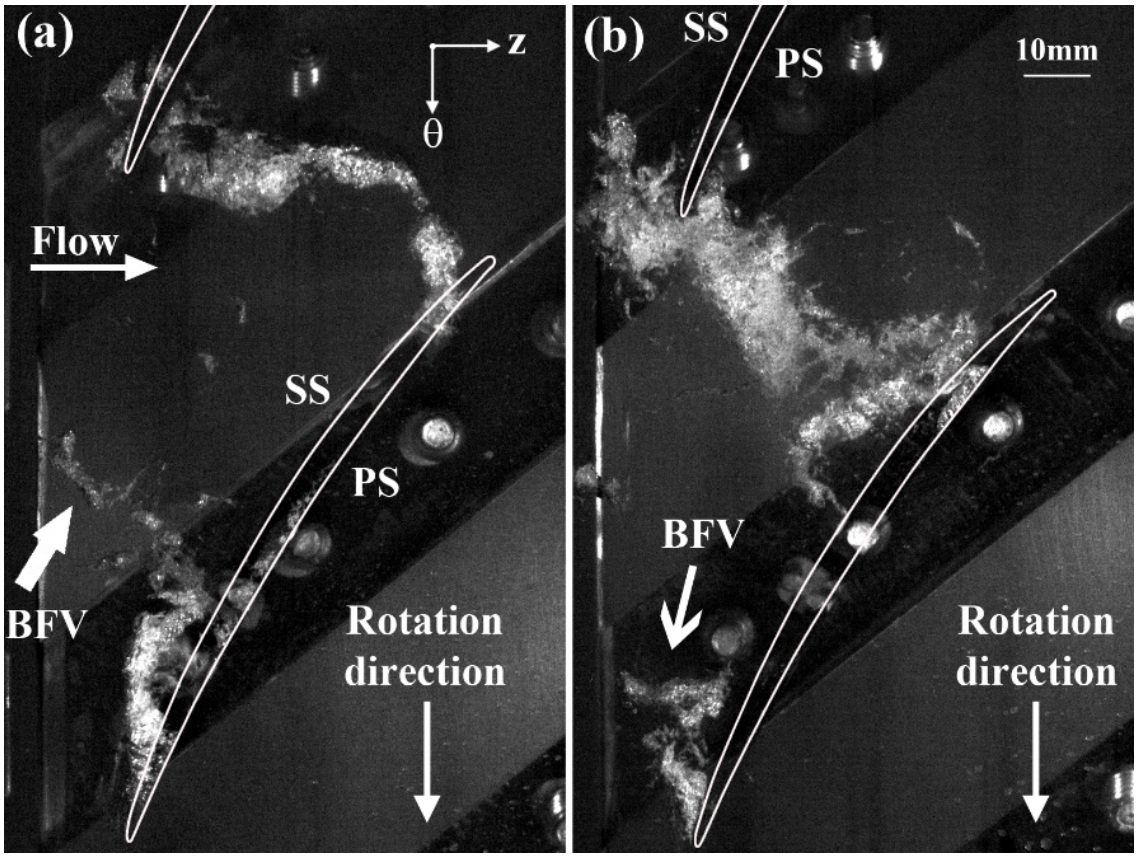

Figure 3-11 Sample unrelated snapshots of huge BFVs in the rotor passage at stall conditions

As discussed before, stall inception occurs and the pressure rise across the pump drops dramatically when the flow rate coefficient is reduced from φ=0.25 to 0.24 (Figure 3-1). The cavitation visualizations, samples of which are presented in Figure 3-11, reveal that under this condition, the BFVs roll up earlier and appear more frequently, as well as grow more rapidly and to a considerably larger size compared to those at the pre-stall condition. Hence, multiple BFVs frequently extend from the SS of the same blade at the same time. Yet, their appearance and process of development appear to have many of the same characteristic features. Their downstream ends appear to be connected to the SS of one blade, and the upstream ends extend well upstream of the leading edge of the adjacent blade or penetrating across the tip gap to the next passage, depending on their location. Propagation from upstream around the leading edge,

which occurs frequently under stall conditions would presumably have more influence on the flow in the next passage than disturbances penetrating across the tip gap. Figure 3-11a, the size of the newly formed BFV indicated by an arrow is already comparable to that of a "fully developed" structure in Figure 3-5d. In Figure 3-11b the vortex indicated by another arrow rolls up near the blade leading edge. These structures migrate mostly circumferentially with the blade, and slowly downstream, indicating that once they form, there is little through-flow in the tip region. Accordingly, when a BFV begins to interact with the leading edge of the next blade, the TLV of that blade disappears completely, suggesting a loss of the lift force at least in the tip region. Such interactions might also induce leading edge separation, the process affecting stall onset according to (Pullan *et al.*, 2015; Yamada *et al.*, 2013). It should be noted that this structure appears to be similar to that observed in (Kosyna *et al.*, 2005) under the deep stall, but in their case, the vortex appears to be fixed relative to the blade.

Discussion

Among the questions that the present measurements raise, it would be of interest to determine whether the phenomena described in this study correspond to spike or modal type stall (Camp *et al.*, 1998; Day, 1993; Deppe *et al.*, 2005; Garnier *et al.*, 1991; McDougall *et al.*, 1990; Tan *et al.*, 2010). We have not performed wall pressure fluctuation measurements at the enwall casing at the onset of stall, so our assessment is suggestive, but not decisive. Several features of the available data at φ=0.25 appear to be consistent with a spike-type stall described in (Camp *et al.*, 1998; Day, 2015). First, the pre-stall condition, φ=0.25, is still located at a slightly higher flow rate than the peak in the total-to-static performance curve. Second, the influence of the BFV on the flow around the leading edge of the next blade is intermittent and quite infrequent under the pre-stall conditions. Third, once the flow around the leading edge is disrupted by the BFV, the effect, as Figure 3-8 shows, is substantial covering the entire tip region of the blade. In other words, this is not a small perturbation. Fourth, yet, all the presently observed phenomena are confined to

the tip region, where they are expected to generate high-pressure fluctuations in the endwall casing. Conversely, at φ=0.24, the slope of the T-S curve (Figure 3-1b) is already positive, consistent with trends of modal stall inception. The frequency of events is also much higher. However, as the present observations indicate, the flow phenomena triggering the performance loss at φ=0.24 and 0.25 appear to be similar, but with increasing frequency and strength.

Another question is the relationship between the BFV and the tornado-like vortex described in (Inoue *et al.*, 2001, 2002; Yamada *et al.*, 2013) and affiliated with the onset of stall. Both cases involve a complete or partial ring-like vortical structure that surrounds the TLV. However, the formation mechanisms and locations involved are very different, since the BFV is not associated directly with leading-edge separation, although it might cause one. In fact, in most of the present cases, the BFV is initiated downstream of the leading edge as a previous BFV propagates across the tip gap and causes rollup of the shear layer at the bottom of the high u_θ region. Furthermore, as discussed in Pullan *et al.* (2015), the tornado-like vortex does not necessarily require a backflow, whereas the present structures are an inherent outcome of backward leakage flow.

Before concluding, it should be noted that BFVs are also observed at much higher flow rates than the current pre-stall and stall conditions. However, at φ=0.35 for example, roll-up of these structures occurs in the aft part of the rotor passage, they are much more intermittent, and for the most part, they appear to be much weaker. Hence, they are mostly entrained by the TLV before it bursts and rarely makes it to the tip gap of the next blade. Also, as noted before, in a parallel study focusing on the effects of the tip gap size on the flow structures of the same machine (Li *et al.*, 2016) and in (Tan *et al.*, 2015b), similar BFVs have been observed when the tip gap is much narrower (h/c=0.5%). However, since the BFV cannot be entrained across the narrow tip gap, its influence on the adjacent blade passage is greatly diminished. Furthermore, occurrence and persistent formation of BFVs is not limited to the present blade geometries. For example, the BFV and vortical layers emerging from the tip gap have been seen in previous measurements

performed within the previous generation AxWJ-1 waterjet pump (Wu *et al.*, 2011a, 2011b). Sample cavitation images showing the BFVs developing in the AxWJ-1 rotor passage are shown in Figure 3-12 at two different flow rates. At high flow rate (Figure 3-12a), the ring-like BFV develops around the TLV while at a low flow rate (Figure 3-12b) it extends upstream and orientates perpendicular to the blade. Although the presently available data is limited to three pump/compressor geometries, several flow rates, and two tip gaps for the present compressor, the BFVs and mechanisms generating them appear with varying degrees of influence in all of them. The formation of a BFV and its association with tip leakage flows appears to be a ubiquitous phenomenon.

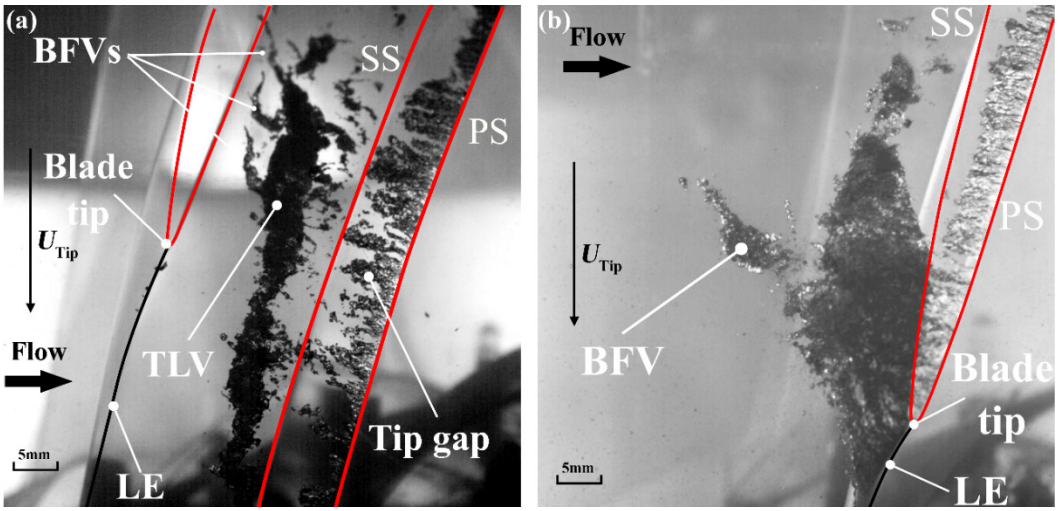

Figure 3-12 Sample cavitation images showing BFVs formation in the AxWJ-1 rotor passage at different flow rates: (a) High flow rate and (b) low flow rate near stall. Images are taken in the AxWJ-1 pump by Huixuan Wu (Wu *et al.*, 2011b).

Lastly, another question involves the influence of the IGV and its wakes on the formation and development of the BFV. We have not studied this effect based on velocity measurements yet. However, systematic evaluations of the cavitation movies clearly show that the appearance and development of the BFV do not occur at specific circumferential angles relative to the IGV blades. In a field of view that covers three IGV blades, the vortex appears intermittently at different

locations. Moreover, similar BFVs appear in the abovementioned axial waterjet pumps that do not have IGVs. However, these observations do not necessarily imply that the non-uniform inflow does not affect the strength, trajectory, and influence of the BFVs. We will explore this question in future studies.

3.3 Summary

Stereoscopic PIV measurements and cavitation-based flow visualizations are used for resolving flow structures characterizing pre-stall and early stall conditions in the tip region of the rotor passage of an axial compressor. The experiments have been performed in the JHU optically index matched facility, which facilitates unobstructed observations on the origin and evolution of flow features at any desired point. All the flow instabilities affecting the onset of stall are associated with the 3D tip leakage flow and its interaction with the rest of the passage flow. As the TLV rolls up, it entrains the leakage flow and forms a region with high circumferential velocity (low circumferential velocity relative to the blade) under the vortex center. Hence, the flow in the tip region could be envisioned as a 3D swirling jet in which the center of swirl is located above the jet center. In the ensemble-averaged 3D vorticity distributions, obtained by combining data recorded in a series of closely spaced meridional planes, this jet appears as a vortex ring that surrounds the TLV. As the TLV grows in size, detaches from the blade SS, and breaks down in the middle of the passage, the size of the elevated circumferential velocity region expands, eventually reaching the pressure side of the adjacent blade. The vorticity at the transition between the high circumferential velocity region below the TLV center and the main flow deeper in the passage is oriented nearly perpendicularly to the blade surface. Once this vortical region is perturbed, it rolls up into a vortex segment that extends diagonally upstream, from the vicinity of the suction side (SS) of the originating blade to the edge of the elevated circumferential velocity region (where the vorticity changes direction). Due to its orientation, we refer to this structure as

a backflow vortex (BFV), adopting the terminology used to describe vortices extending upstream of rocket fuel inducers (Yamamoto *et al.*, 2009; Yamanishi *et al.*, 2007; Yokota *et al.*, 1999).

As the SS end of the BFV propagates in the passage, it grows in length, and intermittently reaches the pressure side of the next blade together with the high u_θ zone above it. For the present large tip gap, the BFV and high u_θ zone readily propagate across the tip gap to the SS of the adjacent blade and trigger a similar instability in the next passage. Hence, once it starts, the process propagates circumferentially from one passage to the next. As it crosses the tip gap, the BFV and high u_θ zone alter the blade load distributions, as demonstrated by the major shift in the location of TLV rollup on this blade. Although the ensemble-averaged 3D vorticity distributions cannot reveal the structure of such intermittent phenomena, a small fraction (~4%) of the instantaneous planar snapshots bear clear signatures of the BFV, which include a series of vortical structures bounding the bottom side of a very high u_θ zone, where the passage flow is essentially blocked. These snapshots reveal a flow structure that differs substantially from the "normal" SS flow condition when the passage is not stalled.

BFVs of varying strengths and locations have been seen in rotors having a narrow tip clearance, but in these cases, they cannot propagate to the next passage across the tip gap. The same flow phenomenon also causes intermittent, but significant changes to the incidence angle upstream of the blade leading edge. Such incidence changes might cause leading edge flow separation in some machines, as observed at the onset of stall in other studies, but it does not appear to occur for the present pre-stall flow. Although we have not measured the pressure fluctuations in the endwall casing, several features of the BFV development process described in this study at pre-stall conditions are consistent with spike-type stall (Camp *et al.*, 1998; Day, 1993; Garnier *et al.*, 1991; McDougall *et al.*, 1990). Included are the location of the pre-stall condition in the performance curve, intermittent appearance, and effect on the flow around the leading edge of the blade, and confinement to the tip region.

By further reducing the flow rate and pushing the present machine into stall conditions, the size and frequency of the BFVs increase substantially, and they extend upstream of the leading edge of the adjacent blade. Hence, they can propagate to the next passage and trigger instabilities there without being ingested across the tip gap. Furthermore, they alter the blade loading, as indicated by the delayed TLV rollup.

Chapter 4 Study of Stall Suppression and Associated Changes to the Flow Structures in the Tip Region of the NASA Compressor Rotor by Axial Casing Grooves

This Chapter discusses the effects of axial casing grooves on the performance and flow structures in the tip region of NASA compressor rotor. The semicircular grooves have a dramatic effect on machine performance, reducing the stall flow rate by 40% compared to the same machine with a smooth endwall. However, they reduce the pressure rise at high flow rates. The flow characterization consists of qualitative visualizations of vortical structures using cavitation, as well as SPIV measurements in several meridional and (z,θ) planes covering the tip region and interior of the casing grooves. The experiments are performed at a flow rate corresponding to pre-stall conditions for the untreated machine. They show that the flow into the downstream sides of the grooves and the outflow from their upstream sides vary periodically. The inflow peaks when the downstream end is aligned with the PS of the blade, and decreases, but does not vanish when this end is located near the SS. These periodic variations have three primary effects: First, substantial fractions of the leakage flow and the TLV are entrained periodically into the groove. Consequently, in contrast to the untreated flow, the TLV remnants remain confined to the vicinity of the entrance to the groove, and the TLV strength diminishes starting from the mid-chord. Second, the grooves prevent the formation of large scale BFVs, which are associated with the TLV, propagate from one blade passage to the next, and play a key role in the onset of rotating stall in the untreated fan. Third, the flow exiting from the grooves causes periodic variations of about 10° in the relative flow angle around the blade leading edge, presumably affecting the blade loading. The distributions of turbulent kinetic energy provide statistical evidence that in contrast to the

untreated casing, very little turbulence originating from a previous TLV, including the BFVs, propagates from the PS to the SS of the blade. Hence, the TLV-related turbulence remains confined to the entrance to groove. Elevated, but lower turbulence is also generated as the outflow from the groove jets into the passage. This work was published in the *Journal of Turbomachinery* (Chen *et al.*, 2017b).

4.1 Experimental setup

Casing grooves

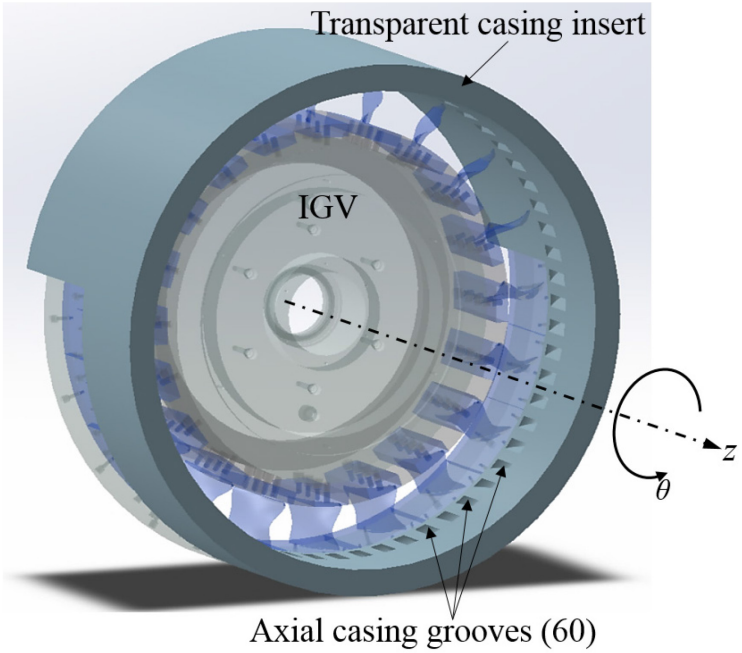

Figure 4-1 A perspective view of the IGV with axial casing grooves.

As shown in Figure 4-1, the casing grooves are machined in an acrylic ring that surrounds the three blade rows. The groove dimensions, location, and orientation are shown in Figure 4-2. The semi-circular grooves have a diameter of $0.65c_A$, out of which, 33% overlaps with the rotor, and the rest, extends upstream of the rotor. The evenly spaced, four per passage grooves are skewed by 45° in the positive circumferential direction, i.e., the same as the rotor rotation (Figure 4-2b).

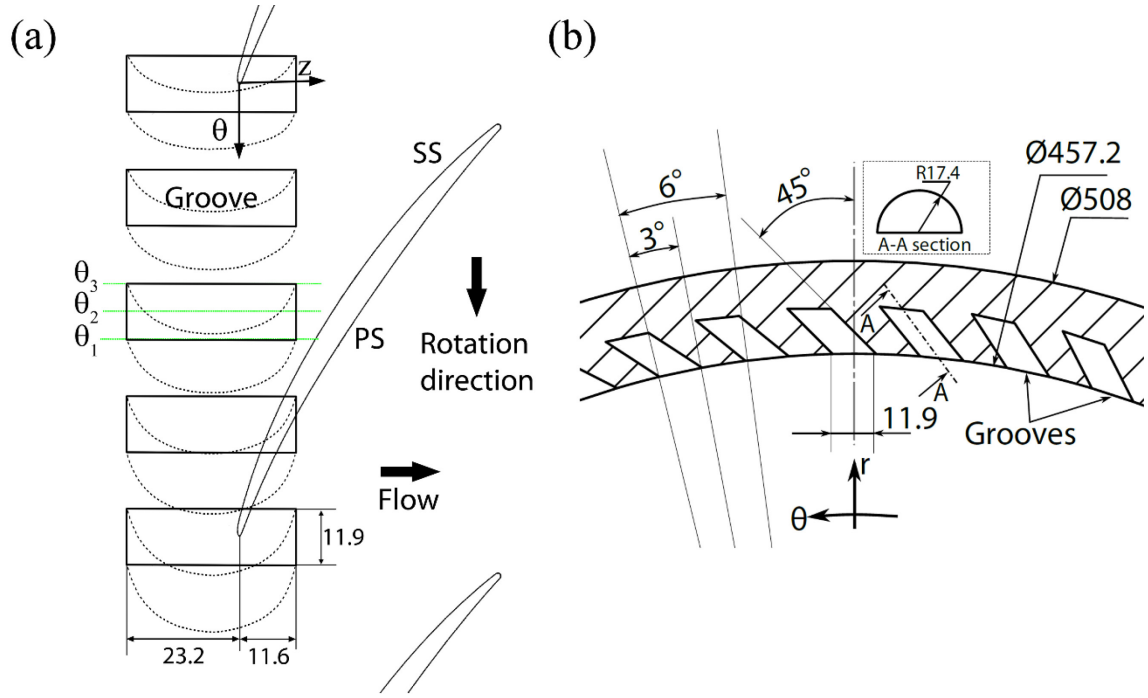

Figure 4-2 The ACG configuration: (a) radial view, and (b) streamwise view (looking upstream). All dimensions are in mm.

PIV setup

The optical setups used in this study are shown in Figure 4-3. During cavitation visualizations, the tip region is illuminated by two continuous halogen lamps shown in Figure 4-3a, the same setup as that in Chapter 3. Images have been recorded by a PCO. dimax high-speed CMOS camera at 5760 frames/s, corresponding to 48 images per blade passage, at a resolution 960×792 pixels. The field of view is 143.6×118.5 mm^2. Index matching allows acquisition of PIV based data in any desired plane. Due to the installation of casing grooves, we have used different setups than those used in Chapter 3. The setup for SPIV measurements in meridional planes is illustrated in Figure 4-3b. The images are recorded by a pair of Imperx B6640 CCD cameras that have 6600×4400 pixel arrays. The total field of view is 44.9×41.1mm^2, and the delay between exposures is 20μs. Data has been recorded in three equally spaced circumferential angles separated by $\Delta\theta = 1.5°$, which are labeled as θ_1, θ_2 and θ_3. Angles θ_1 and θ_3 are located close to the inside

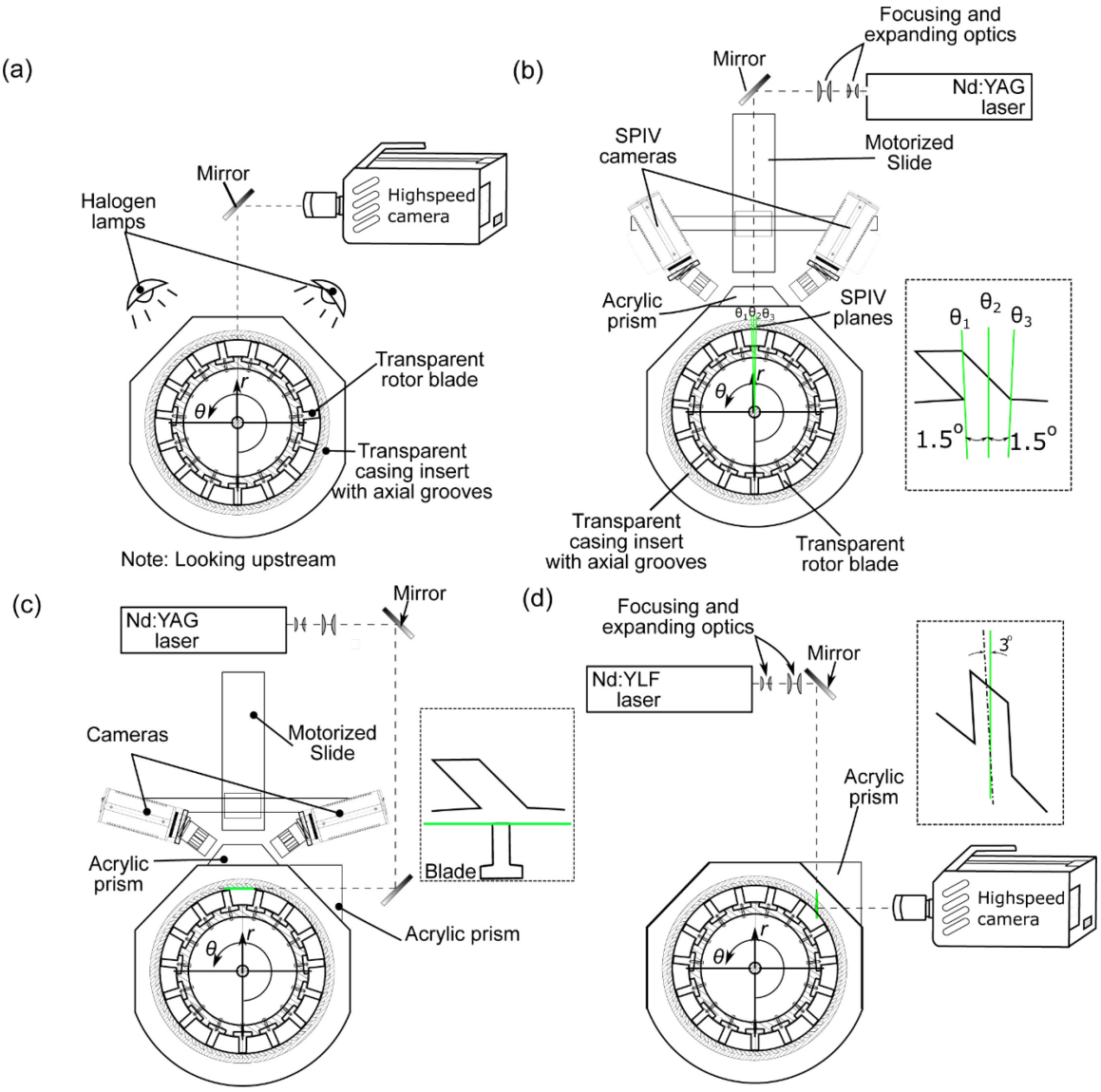

Figure 4-3 Experimental setup for (a) cavitation flow visualization, (b) SPIV in three meridional planes, (c) SPIV in a (z, θ) plane intersecting the blade tip at r^*=0.96, and (d) 2D time-resolved PIV inside a groove.

edges of a casing groove without cutting through them. Angle θ_2 cuts the entrance to the groove. As shown in Figure 4-3c, SPIV measurements have also been performed at a (z, θ) plane, where the radially outer edge of the laser sheet coincides with the blade tip (r^*=0.96). In this case, the images are recorded by a pair of 2048×2048 pixels, PCO. 2000 cameras, also using exposure intervals of 20μs, and the field of view is 40.2×52.2 mm^2. To complete the picture, especially

unsteady flow features, time-resolved 2D PIV measurements at 2.4 kHz have been performed in a plane that is nearly parallel to the center plane of the grooves (Figure 4-3d). In this case, the image pairs have been recorded by the PCO. dimax camera at a resolution of 864×892 pixels, using frame straddling to achieve an in-pair delay of 40μs.

The orientation/phase of the blade relative to the groove is represented by the blade chord fraction (s/c) that the θ_2 plane (Figure 4-2 and Figure 4-3) intersecting the blade chord. For clarity, s/c=0 represents the phase where θ_2 is aligned with the blade LE. The SPIV data have been recorded at 14 different phases, covering an entire blade passage, but the planes are not distributed evenly, with finer separation of $\Delta s/c$=0.055 around the leading edge, and coarser spacing, $\Delta s/c$=0.11 for high chord fractions.

4.2 Results and discussion

Effects of ACGs on the performance

The performance curves with and without casing grooves are compared in Figure 4-4. At high flow rates, the grooves cause a slight decrease in the pressure rise. However, for most of the measured range, they improve the performance substantially, by as much as 17% at φ~0.25. Furthermore, while the onset of stall in the untreated machine occurs at φ~0.24 (Chen *et al.*, 2017c), stall does not occur in the grooved case until φ<0.15, where the performance drops rapidly. For both cases, the rapid decline in performance is accompanied by an audible increase in vibration-induced noise. Hence, the axial grooves reduce the flow rate at the onset of stall by 40%.

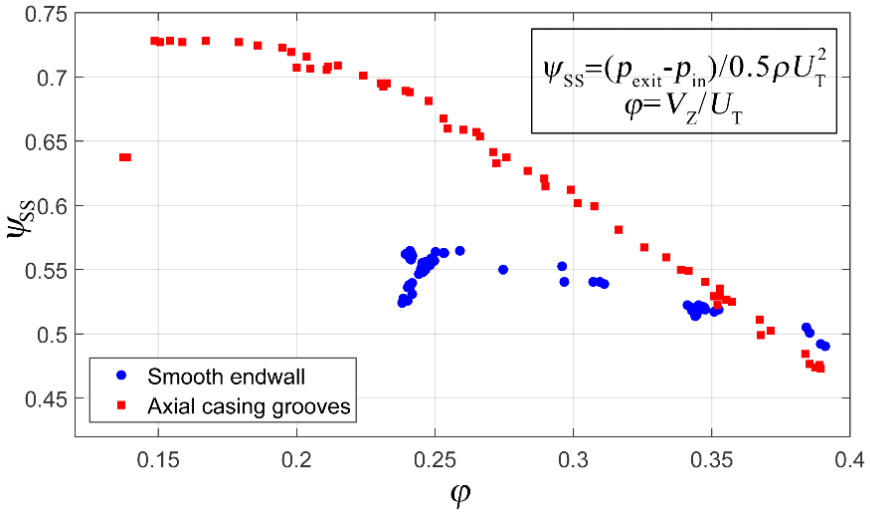

Figure 4-4 Performance curves for h/c=1.8%, with and without the axial casing grooves

Visualization of flow structures by cavitation

Figure 4-5 shows sample images of cavitation at two different flow rates comparing the TLV structure with a smooth casing to that developing when the ACGs are installed. The blade tip profiles and locations of the grooves are highlighted for clarity. At φ=0.35, when the performance of the two machines is not substantially different, Figure 4-5a&b represent a phase for which one of the grooves is located above the initial rollup point of the TLV in the untreated case. The presence of tip leakage cavitation (see annotations) indicates that there is a leakage flow in both cases. However, the point where a distinct TLV first appears on the SS is located further along the blade in the grooved endwall.

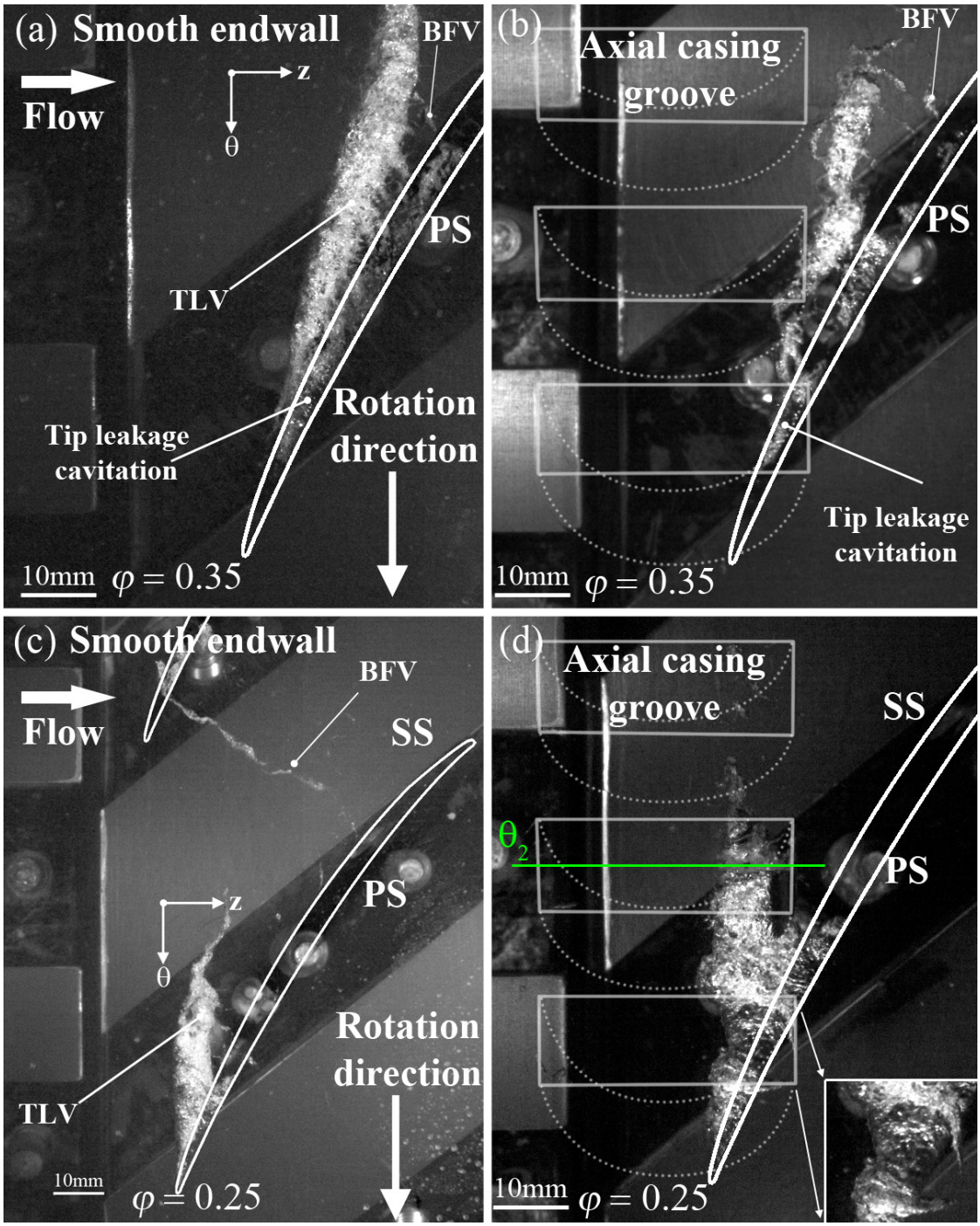

Figure 4-5 Sample cavitation images showing vortical structures in the rotor passage without (left column) and with ACG (right column). Top row (a&b): φ=0.35, and bottom row (c&d): φ = 0.25. Entrance to the grooves are indicated by solid gray lines, and their outlines are marked by dashed lines. Insert in (d) is a magnified view of the groove corner.

Further downstream, the TLV in the untreated rotor gradually detaches from the blade, and small scale BFVs aligned perpendicularly to the blade begin to form between the SS corner and the TLV (marked as BFV). The mechanisms generating them and their influence on the onset of stall are the focuses of our previous publication (Chen *et al.*, 2017c). For the treated endwall (Figure 4-5b), the TLV also begins to migrate away from the blade between the first and the middle grooves (bottom and middle grooves in Figure 4-5b). Yet, near the middle groove, the TLV becomes confined to the space between this groove and the blade, resulting in kinks in the TLV trajectory on both sides of this groove. Further downstream, where the aft parts of the blade that are not located under the grooves, the TLV detaches from the blade again, and several BFVs start to appear as well.

At φ=0.25, the pre-stall condition of the untreated endwall, the TLV rolls up near the blade leading edge and migrates away from the SS at a shallow angle with the circumferential direction. The cavitation disappears at mid-passage, as the vortex breaks up under the influence of the BFVs that appear intermittently in the middle of the rotor passage (e.g., Figure 4-5c). As discussed in Chen *et al.* (2017b), the formation and circumferential propagation of the BFVs diagonally upstream, and their penetration across the tip gap or around the leading edge of the next blade triggers generation of similar structures in the next passage, and so on. The BFV vorticity is originated from the leakage flow, but it rolls up radially inward from the TLV. As the BFV crosses the tip gap, the TLV rollup is disrupted, and in some cases pushed further along the blade briefly, suggesting a temporary reduction in the local blade loading. This process is intermittent under pre-stall conditions but is a major contributor to the substantial increase in turbulence level over a broad area. At the onset of stall (e.g. at φ=0.24), the BFVs roll up earlier, and appear more frequently, sometimes more than one per passage. They also grow more rapidly and to a larger size. Once formed, their propagation from one passage to the next persists for a while. Furthermore, they appear to rotate with the blade, while migrating slowly downstream, indicating that the flow

the entire tip region is nearly blocked. Hence, generation and circumferential propagation of the BFVs is a primary phenomenon associated with the onset of stall.

For the grooved endwall and φ=0.25, Figure 4-5d shows that the TLV boundary becomes wavy, with what appears to be a narrower waist under the first groove combined with decreased tip leakage cavitation in the same area. The high-speed movies show that the waist is formed as part of the TLV cavitation is entrained into the groove. Further away from the blade, the TLV tail seems to diminish under the middle groove, leaving very little cavitation beyond it. As demonstrated quantitatively later, this phenomenon is caused by entrainment of substantial parts of the TLV into this groove, leaving a limited amount of circulation in the main channel. Most importantly, however, is the disappearance of the BFVs, both large and small ones. Hence, the grooves eliminate or at least greatly suppress the primary flow phenomenon propagating circumferentially from one blade passage to the next under pre-stall and stall conditions in the untreated passage. Both effects, namely the periodic suction of TLV and elimination of the BFVs persists at flow rates much lower than φ=0.25 (not shown). Once stall occurs at φ<0.15, the TLV disappears completely periodically, indicating a broad loss of blade loading over more than one blade passage at a time. We have not focused on this domain fearing for the ability of the blades used in the experiments to withstand the unsteady loading for extended periods.

Flow characteristics in the (z, θ) plane

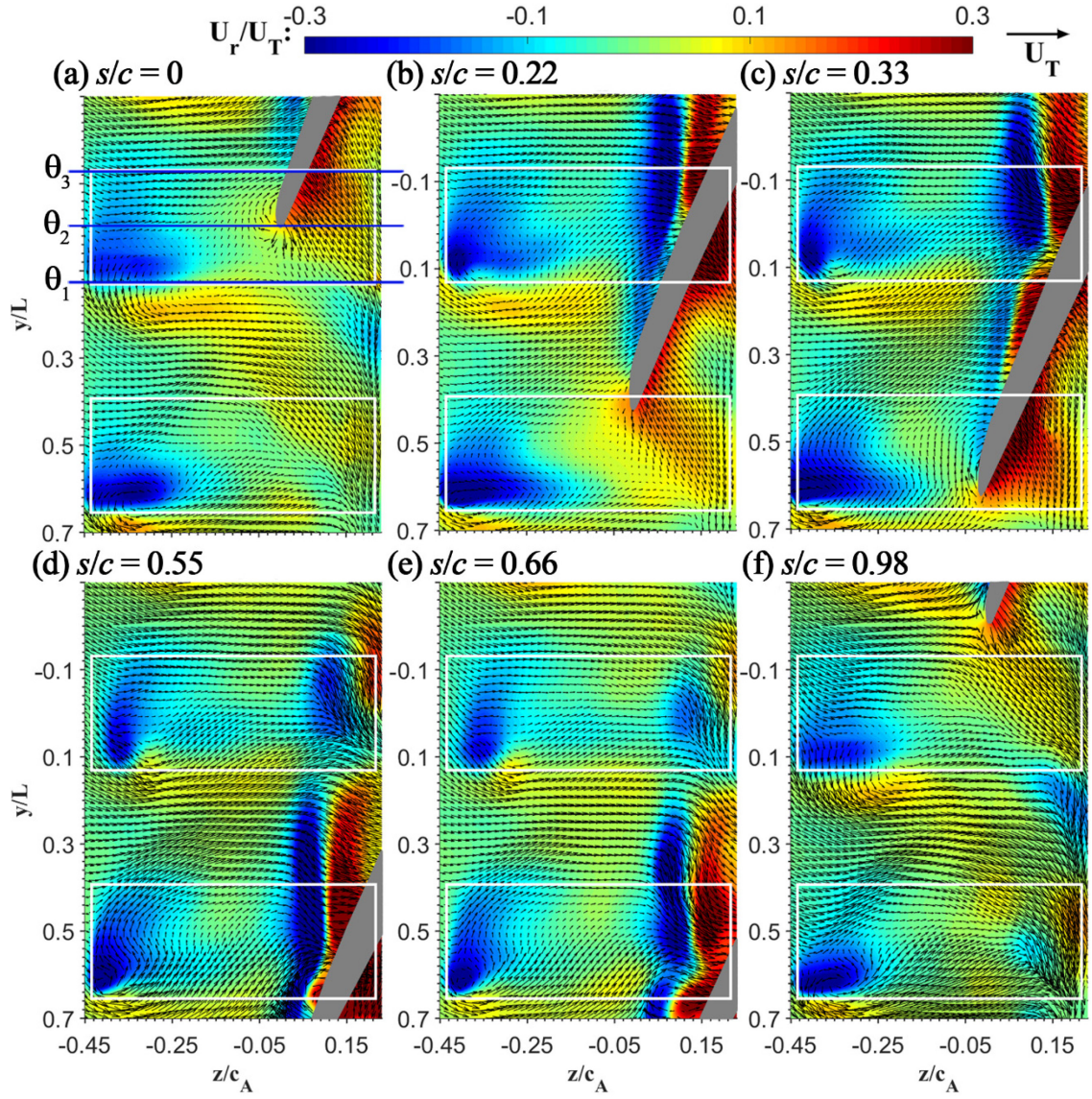

Figure 4-6 Ensemble-averaged in-plane velocity vectors (nearly U_z, U_θ) superimposed on contours of the radial velocity component (r^*=0.96). Vectors are diluted by 4:1 in both directions for clarity. The values of s/c indicate the intersection of the θ_2 plane with the blade chord.

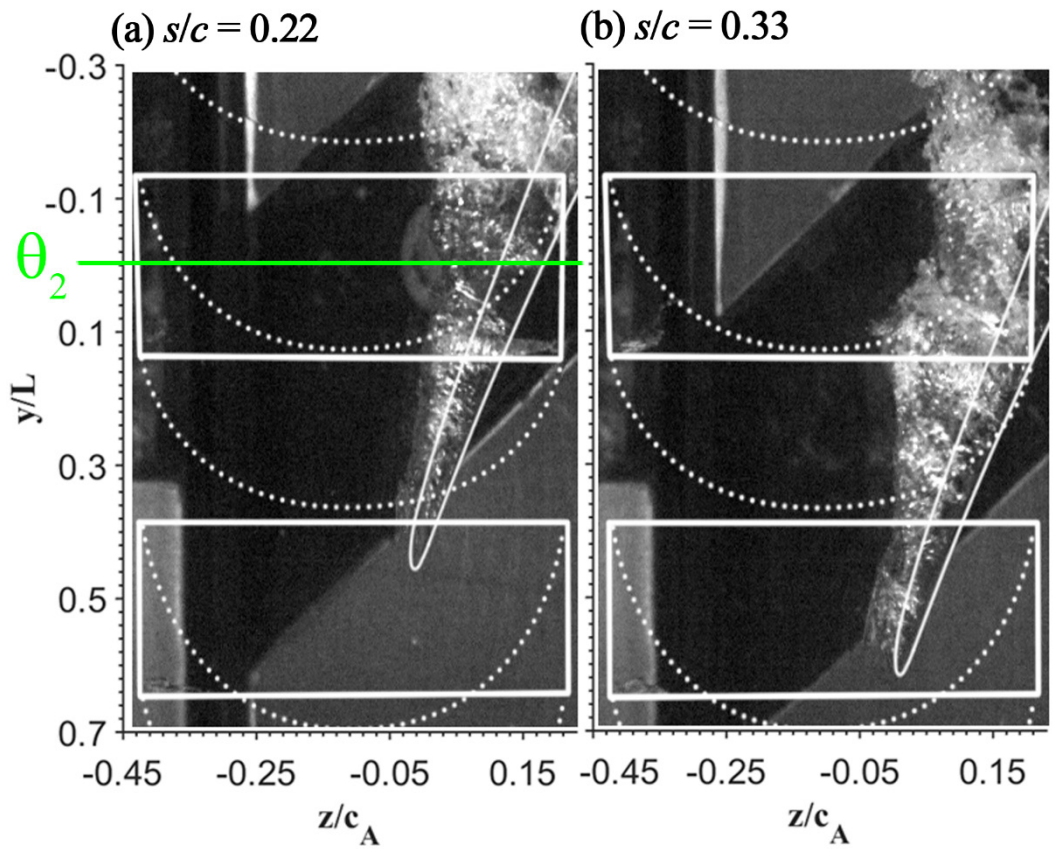

Figure 4-7 Cavitation images at (a) s/c=0.22 and (b) s/c = 0.33

All the PIV data presented in this Chapter has been acquired at φ=0.25 to focus on the mechanism preventing the onset of stall. Figure 4-6 shows six super-positions of ensemble-averaged in-plane velocity vector fields and contours of U_r in a (z, θ) plane intersecting the blade tip. The field of view contains two grooves, and their locations are highlighted, along with the location of the three meridional planes (θ_1, θ_2, and θ_3) discussed subsequently. The selected phases elucidate the impact of the grooves on the flow around the blade tip, including the vicinity of the TLV. Corresponding cavitation images for two phases, s/c=0.22 and 0.33 based on the location of θ_2 are provided in Figure 4-7 for comparison. Several trends are evident:

(i) Consistent with Smith *et al.* (1984), there is generally an inflow into the groove on the downstream side, which overlaps with the blade, and outflow from the groove on the upstream

side. The magnitudes and distributions of inflow and outflow vary spatially and temporally, depending on the orientation of the blade relative to the grooves. Starting with the blade effect, $U_r>0$ along the pressure side (PS) of the blade, as expected. Furthermore, U_r transitions from positive to negative values along the TLV center on the SS, making this transition a convenient qualitative means of identifying the trajectory of the TLV center. A comparison with the cavitation image in Figure 4-7 shows that the upstream edge of the narrow negative U_r area nearly coincides with the upstream edge of the TLV cavitation, confirming that the positive and negative U_r layers correspond to the TLV-induced velocity. In addition, the measurements in meridional planes discussed later confirm that the transition in U_r sign corresponds to the TLV center.

(ii) Except for periods when the downstream end of the groove is facing the SS of the blade (e.g., Figure 4-6c) and strongly affected by the TLV, U_r is largely positive at the downstream end (the inflow/entrance end) of both grooves. This radial inflow, combined with $U_\theta>0$ consistent with the groove angle, increases when the entrance is aligned with the PS of the blade. Such an increase occurs e.g., when the LE is aligned with θ_2 (s/c=0) in Figure 4-6a, or when the LE is aligned with the lower groove at s/c=0.33 (Figure 4-6c). The magnitude of U_r peaks as the PS approaches the downstream edge of the upper groove in Figure 4-7b and the lower groove in Figure 4-6d.

(iii) $U_r<0$ over the entire upstream/exit end of the grooves, with the exit flow being persistently higher at the high θ corner of the grooves, e.g., the corner corresponding to θ_1 in the upper one.

(iv) Discontinuities in the TLV trajectory. When the blade SS is facing the entrance to the groove, Figure 4-6c shows that the TLV signature is divided into two parts, consistent with the corresponding cavitation images (Figure 4-7b). The first part extends from the LE to the vicinity of θ_1. It is characterized by a TLV confined to the vicinity of the blade SS with a weak vortex-induced velocity. The second part originates from the region facing the groove entrance, close to the SS surface, where the in-plane flow appears to converge towards this origin. The (positive and

negative) TLV-induced velocity is initially quite high, reaching 30% of the tip speed, and the vortex center remains aligned in the circumferential direction, not far from the downstream edge of the groove. As the SS moves away from this groove, e.g., in Figs. 6d and e, the remnants of the TLV-induced radial velocity decrease in magnitude, but remain "latched" to the downstream corner of the groove. As demonstrated below, the decreasing TLV signature is associated with partial entrainment of the TLV into the groove. These decaying TLV remnants finally disappear in Figure 4-6f, only as the entrance to the groove begins to be influenced by the PS of the next blade and associated increase in radial inflow. Essentially the same phenomenon occurs around the downstream end of the lower groove, resulting in two TLV discontinuities in Figure 4-6d. These grooves are located at different circumferential angles relative to the location of the IGV blades, suggesting that the IGV or its wake are not playing primary roles in the observed phenomena.

(v) The distribution of in-plane velocity components (U_z, U_θ) vary substantially with blade orientation relative to the groove but persistently show the stream originating from the exit and propagating diagonally towards the blade with $U_\theta<0$ and $U_z>0$. As shown in the following Section, this stream causes fluctuations in the relative flow angle around the blade LE. The direction of U_θ is negative in most of the area overlapping with the groove, as expected, but transitions rapidly to positive values near the θ_1 corner, followed by a sharp turn towards the axial direction. The latter phenomenon is likely caused by the main passage flow circumventing the jet exiting from the groove.

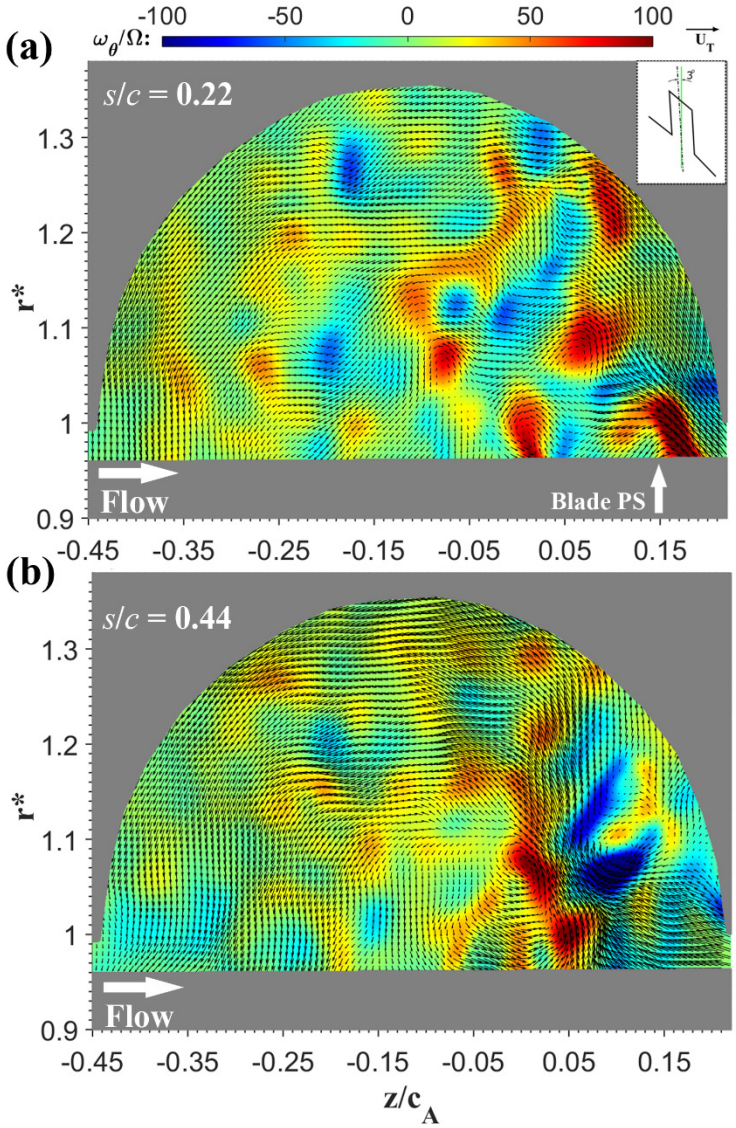

Figure 4-8 Samples of instantaneous vectors of in-plane velocity components and contours of plane-normal vorticity in the center plane of the groove. (a) *s*/*c*=0.22, when the blade PS is exposed to the groove, and (b) *s*/*c*=0.44, when the SS is located downstream of the groove.

Flow characteristics in the meridional planes

Figure 4-8 provides two samples of the instantaneous vectors of the in-plane velocity components and contours of the plane-normal vorticity in the center plane of the groove for different *s*/*c*. In both cases, the flow circulates in the groove, entering from the downstream side

and exiting from the upstream side, as already observed in prior numerical studies (Wilke *et al.*, 2004). The time-resolved data recorded in this plane clearly shows that the flow always circulates in the groove in the same direction, but the velocity magnitude and flow direction around the downstream/entrance end vary substantially with blade location relative to the groove. At s/c=0.22 (Figure 4-8a), when the blade PS is exposed to the downstream end of the groove (see Figure 4-6b), the inflow is dominated by a strong narrow jet originating from the PS. Conversely, at s/c=0.44 (Figure 4-8b), when the blade SS is already located downstream of the groove, the tip leakage flow seen on the bottom right corner of the plot is mostly axial. This axial flow persists for about 20% of the groove's length and then turns into the groove as a diagonal jet while causing flow separation at the downstream corner. As discussed below, the positive vorticity at the upstream side of the jet is originated from the TLV, and the negative vorticity on the downstream boundary is originated from the enwall boundary layer. It is also evident that the peak vorticity in entrained vortical structures persistently decreases as the flow circulates in the slot. Furthermore, the organized vortical layers at the entrance are replaced with what appears to be "scrambled" turbulence at the exit.

Figure 4-9, Figure 4-10 and Figure 4-11 display the distributions of ensemble-averaged circumferential vorticity and three velocity components for three different *s/c* selected to represent different phases of blade-groove interactions. Each figure displays data for three meridional planes intersecting the same groove at a different location, as illustrated in the top right-hand corner. Inherent to variations in their location relative to the groove, the flow structures displayed in them differ significantly. The following discussion highlights and analyzes some of the main features, but not all of them. Yet, we opt to present the entire sets for the selected *s/c* (data is available for other regions as well) to give the reader a complete picture on the blade-groove interactions. The datasets show that:

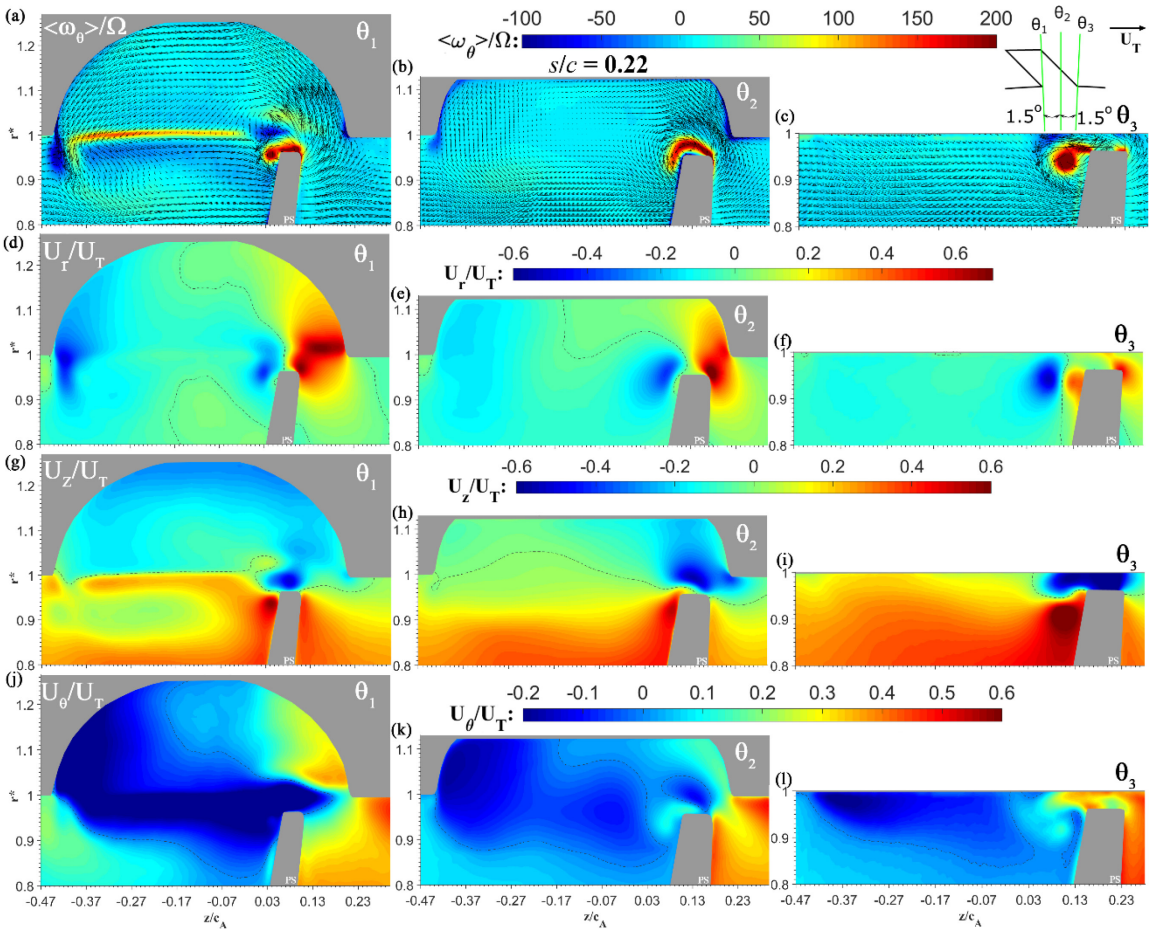

Figure 4-9 Ensemble-averaged vorticity and velocity distributions in meridional planes θ_1 (left column), θ_2, (middle column), and θ_3 (right column) when θ_2 intersects the blade at s/c=0.22. Top row: $<\omega_\theta>/\Omega$; second row: U_r/U_T; third row: U_z/U_T and bottom row: U_θ/U_T. Vectors are diluted by 5:1 in both directions for clarity in the top row. Dash lines indicate the zero values.

General Persistent Features: The discussion starts with features that persist at all s/c. First, consistent with Figure 4-6, the outflow from the upstream end of the groove peaks close to the θ_1 plane irrespective of blade orientation, with U_r reaching 40% of the tip speed. The corresponding peak negative values of U_θ are systematically lower, i.e., the returning flow is not skewed at the same angle as the groove even before entering the passage. A much weaker outflow is also evident in all the θ_2 (middle) planes. As the radially inward jet penetrates the passage, it creates a region with U_z deficit bounded by a negative $<\omega_\theta>$ layer upstream. Second, at θ_1, a narrow positive

vorticity layer aligned along r^*~1 extends along the boundary of the groove, except for the upstream and downstream corners. Being located near the edge of the groove, this layer originates from the nearby endwall boundary layer, as the corresponding sharp transition in U_z confirms. Third, consistent with the skew angle, the inflow into the groove (downstream side) largely involves regions with positive radial and circumferential velocity components. However, the flow phenomena there are complex and phase-dependent due to the blade and TLV interactions with the groove discussed below.

Phase-Dependent Flow Features: Figure 4-9 corresponds to s/c=0.22, the same orientation as Figure 4-6b and Figure 4-7a, providing multiple viewing angles of the same phase. Here, part of the blade PS, which includes the θ_1 and θ_2 planes, is exposed to the downstream corner of the groove, resulting in a high-speed jetting inflow, with radial velocity well above 50% of the tip speed. The circumferential velocity is much smaller, indicating, like in the exit, that the inflow is not aligned with the groove skewness. In the θ_1 plane, a small TLV is already rolled up near the SS tip corner, but a substantial fraction of the vorticity is concentrated above the blade tip. In the θ_2 plane, which corresponds to the origin of the second part of the TLV and where the vortex is "discontinuous", the vorticity is mostly confined to the blade tip. At the end of the groove, in the θ_3 plane, the distinct vortex reappears. These observations suggest that the TLV discontinuity occurs as inflow separates in the PS corner, and jets straight into the groove, with a substantial fraction of the vorticity originating from the PS boundary layer remaining above the blade tip (a comparison to the untreated case follows). Also notable for this phase is the wide layer with negative U_θ in the θ_1 plane, just below r^*~1. As Figure 4-6b demonstrates, this phenomenon originates from the outflow from the next (lower) groove, and as discussed in the following Section, causes periodic variations in the relative flow angle around the blade LE.

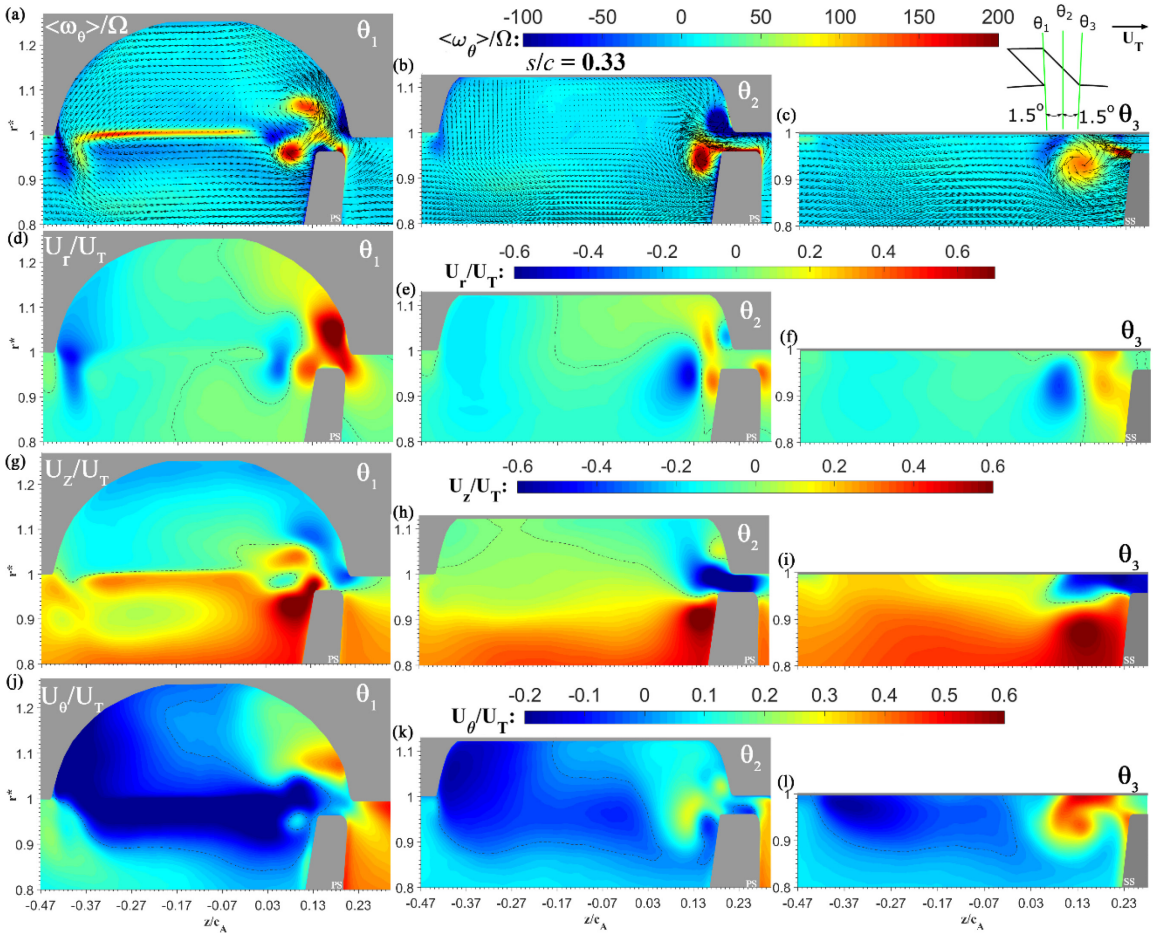

Figure 4-10 Ensemble-averaged vorticity and velocity distributions in meridional planes θ_1 (left column), θ_2, (middle column), and θ_3 (right column) when θ_2 intersects the blade at s/c=0.33. Top row: $\langle\omega_\theta\rangle/\Omega$; second row: U_r/U_T; third row: U_z/U_T and bottom row: U_θ/U_T.

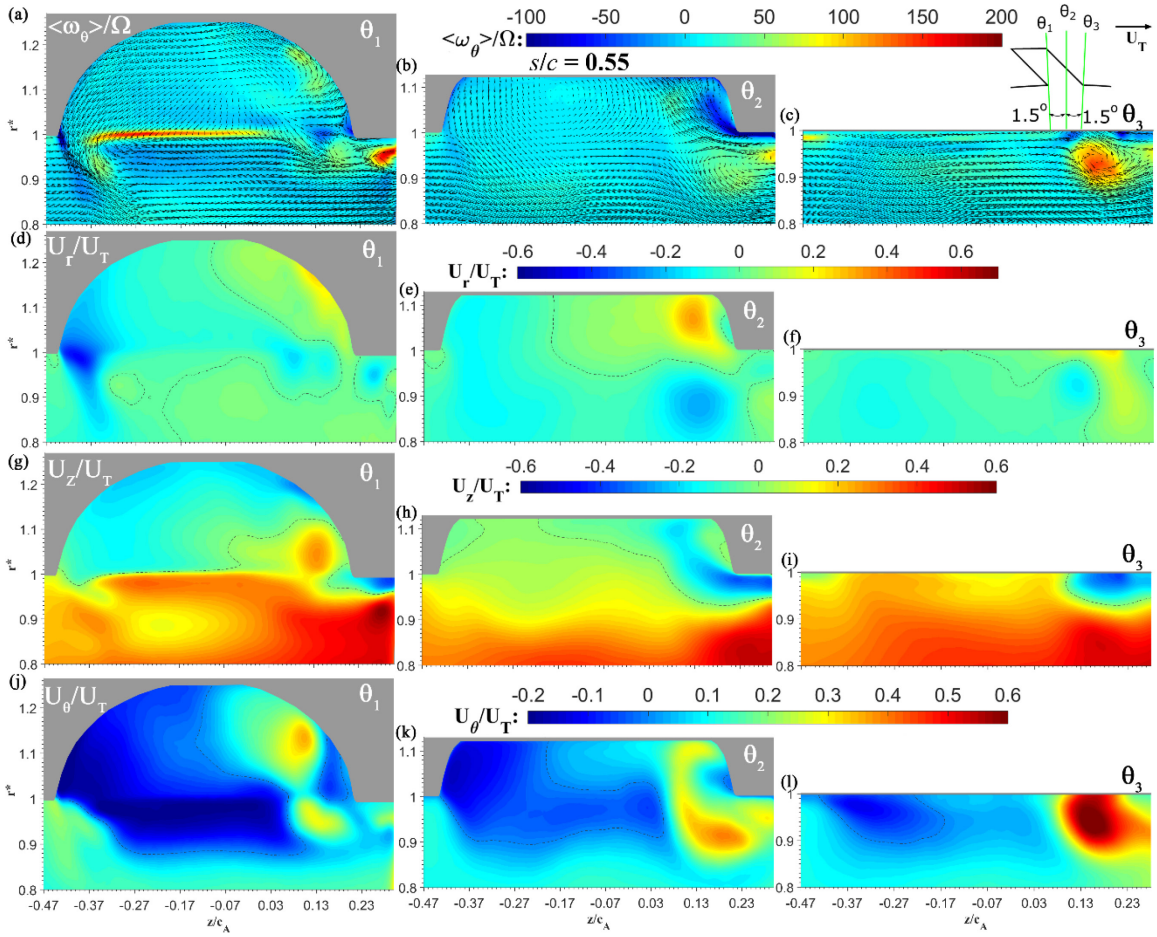

Figure 4-11 Ensemble-averaged vorticity and velocity distributions in meridional planes θ_1 (left column), θ_2, (middle column), and θ_3 (right column) when θ_2 intersects the blade at s/c=0.55. Top row: $\langle\omega_\theta\rangle/\Omega$; second row: U_r/U_T; third row: U_z/U_T and bottom row: U_θ/U_T.

At s/c=0.33 (Figure 4-10), which corresponds to Figure 4-6c and Figure 4-7b, the TLV is split in the θ_1 plane, as part of it is entrained into the groove by the narrow but fast radial jet (U_r/U_T>0.6) still originating from the PS. The abovementioned wide layer with U_θ<0 at $r^*\leq1$ originating from the neighboring groove is evident in this plane as well. In the θ_2 plane, the PS is no longer exposed to the groove, the high-speed tip leakage flow becomes predominantly axial with U_z exceeding 60% of the tip speed, and the radial flow into the groove diminishes. Flow separation occurs at the corner of the groove, near the SS tip, creating a pair of counter-rotating vortices, one associated/coinciding with the TLV, and the other occupying the corner with the

vorticity originating from the endwall boundary layer. In the θ_3 plane, a distinct TLV is already detached from the blade, and a shear layer with the same vorticity sign, seen also in all the untreated cases (Li *et al.*, 2016), connects it to the SS tip corner. The circumferential velocity around the vortex center is positive and higher than the surrounding area, i.e. the TLV behaves like a swirling jet. A negative vorticity layer extends from the endwall upstream of the TLV. A similar layer forms in untreated tip flows (Li *et al.*, 2016), where the vorticity originates from the endwall boundary layer, above the blade tip, and separates from the wall at the point where the main passage flow meets the backward tip leakage flow where.

At s/c=0.55 (Figure 4-11), which corresponds to Figure 4-6d, the blade SS is located just to the right of the present field of view. There are two vortices near the downstream/entrance corner of the groove in the θ_1 plane. The first is "latched" to the corner and the second is a small, concentrated, and newly rolled-up vortex located near the blade SS. In the θ_2 plane, these two structures are already merged into a larger single vortex with a low peak vorticity centered slightly upstream of the groove corner. The location of this vortex remnants just upstream of the corner is consistent with the cavitation images and the (z,θ) plane data. The leakage flow with negative U_z along the endwall and the upper part of the vortex turns upward and becomes a diagonal jet at the entrance to the groove. It carries with it positive vorticity originating from the blade (or TLV) and negative vorticity originating from the endwall boundary layer. Yet, the negative axial velocity (Figure 4-11h) and elevated circumferential velocity (Figure 4-11k) in this area, the latter implying a reduced velocity relative to the blade, indicate that the TLV is still powerful enough to block part of the passage flow. As discussed before, in the untreated endwall, the radial gradients of circumferential velocity at the bottom the elevated U_θ region are involved in the formation and propagation of BFVs at the onset of stall (Chen *et al.*, 2017c). As proposed below, one of the effects of the axial casing grooves is to confine the area with elevated U_θ to the immediate vicinity of the downstream corner of the grooves, preventing the formation of large BFVs that extend across the passage.

Finally, in the θ_3 plane, the TLV becomes distinct again and its peak vorticity is higher than that measured in the middle of the groove (Figure 4-11c). The circumferential velocity in this area is also very high (Figure 4-11i), implying that the TLV behaves like a swirling jet. At higher *s*/*c* (not shown), as the flow begins to be influenced by the PS of the next blade, the peak vorticity and circumferential velocity in this plane also diminish. It appears that the last remnants of the vortex latched to the corner are entrained into the groove.

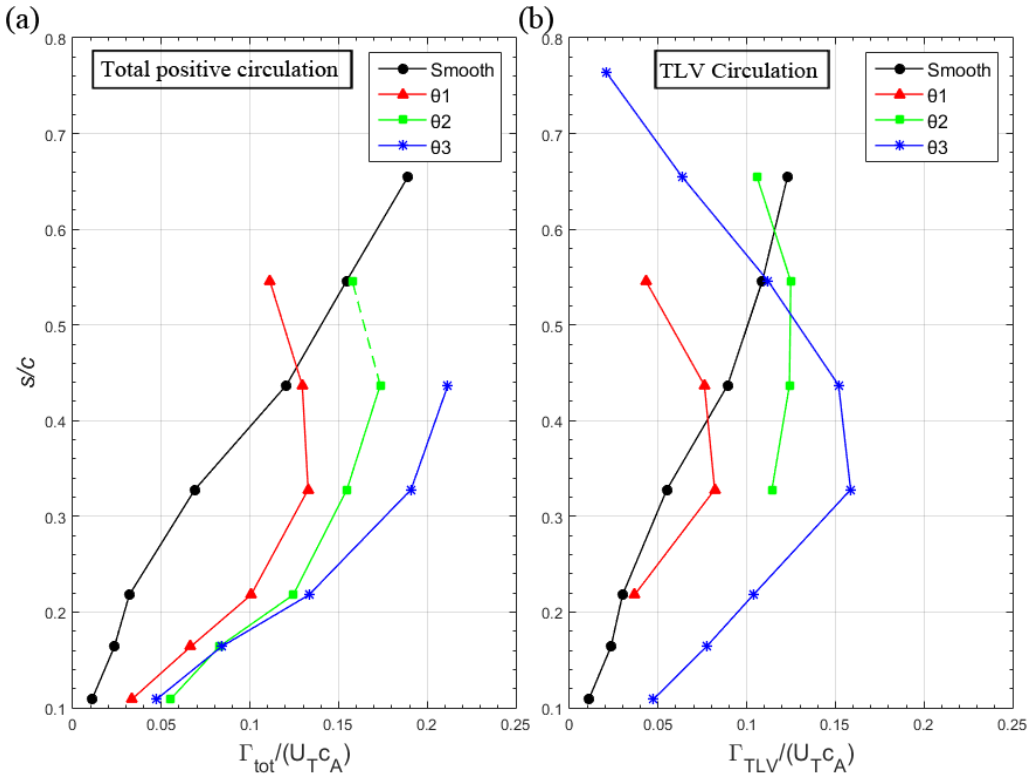

Figure 4-12 Positive circulation (a) over the entire blade SS, and (b) in the TLV

To show the impact of vorticity entrainment on the TLV strength, Figure 4-12a show the evolution of the total positive circulation on the SS of the blade, which is calculated by integrating the circumferential vorticity over areas where it is positive. The dashed lines correspond to the region where the blade is outside of the field of view, hence part of the total circulation is not accounted for in the integration. Figure 4-12b shows the TLV circulation obtained in a similar integration, but only over areas restricted to the TLV. The vortex boundary is defined as the points

where the vorticity drops to 10% of its peak value. Trends are compared to those of the untreated endwall. As is evident and expected, in the untreated case, the TLV and total circulation increase monotonically with *s/c*. The treated endwall has a higher circulation than the untreated casing at low *s/c*, in accordance with the higher pressure rise (Figure 4-4) at the same flow rate. However, in the treated endwall the circulation peaks at mid-chord and then decreases to low values in the aft part. This trend confirms quantitatively that interaction with the groove reduces the TLV strength, presumably by entrainment of part of the TLV circulation as the SPIV data demonstrates. To explain the observed trends, one should note that the magnitude of circulation is affected by two main phenomena, namely shedding from the blade, which increases the circulation, and entrainment by the groove, which reduces it. At low *s/c*, newly shed circulation appears to compensate for the entrained fraction. However, at mid-chord, the generation of new circulation weakens, as the minimal tip leakage cavitation confirms, and entrainment into the groove persists. Hence, the TLV circulation diminishes.

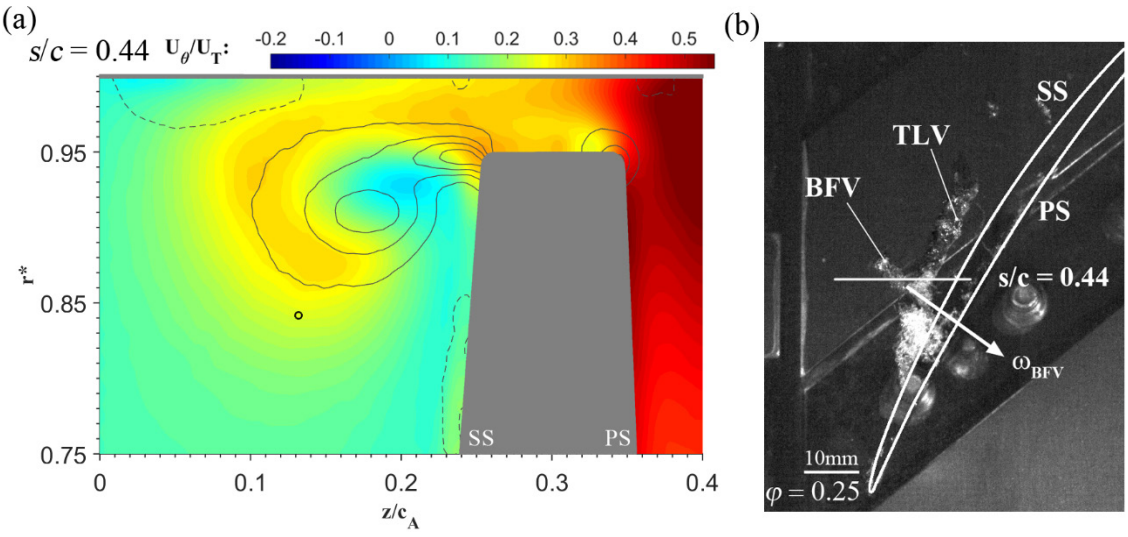

Figure 4-13 (a) Contours of the distribution of U_θ at *s/c*=0.44 and φ = 0.25 in the untreated rotor. The black lines are contours of circumferential vorticity. (b) A sample image shown an early phase of BFV formation at *s/c*=0.44. The arrow shows the measured direction of ensemble-averaged vorticity at the point indicated in (a).

Discussion

The experimental data summarized in the previous sections provide intricate details on the effects of axial casing grooves on the flow structure in the tip region at φ=0.25, which corresponds to pre-stall conditions in the untreated case. The current Section focuses on certain features believed to play an important role in the suppression of stall and the associated substantial increase in pressure coefficient. The discussion is based on comparisons to the flow structure near the untreated endwall. The grooves periodically entrain parts of the TLV circulation, limiting the vortex size and strength, and confining its remnants to downstream corner of the groove. By the time the leading edge of the next blade arrives, the signature of the vortex latched to the corner essentially vanishes.

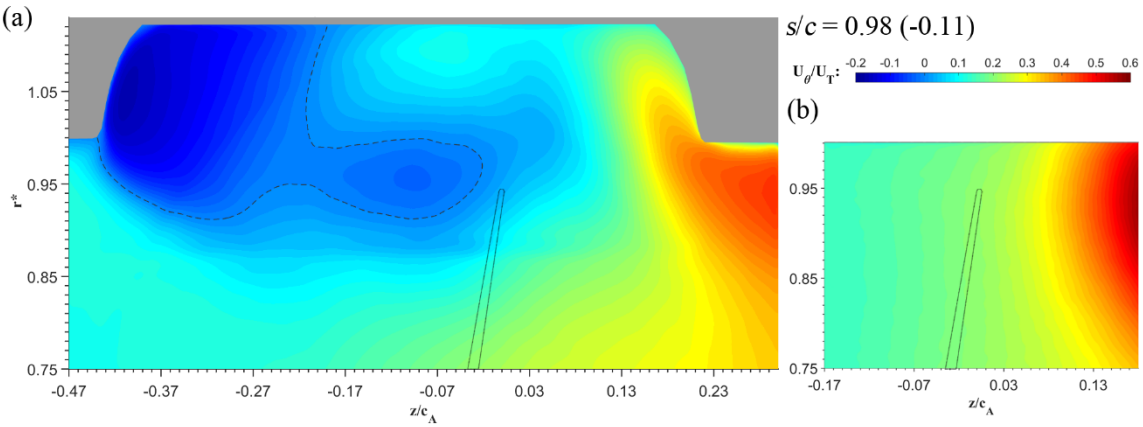

Figure 4-14 Contours comparing the distribution of U_θ at φ=0.25 and s/c=−0.11, i.e. upstream of the blade LE, in the: (a) rotor with axial casing grooves, and (b) untreated rotor. Dashed lines indicate the location of the blade leading edge at s/c=0.0.

It should be noted that the present measurements enable us to determine that vorticity shed from the blade up to *s/c~0.66* is entrained into to groove. However, as the axial distance between SS of the blade and the groove increases, a TLV that is not entrained might rollup between the SS and the groove, outside of the present field of view. Such rollup occurs e.g. at high flow rates, as Figure 4-5b shows. However, Figure 4-5d demonstrates that at φ = 0.25 there is essentially no

cavitation in the tip gap at *s/c>0.5*, suggesting that the leakage flow in the aft part of the passage is weak, consistent with the rotor operating at a low flow rate. Furthermore, the movies do not show a cavitating vortex downstream of the groove, suggesting that if shed vorticity does roll up at *s/c>0.66*, the resulting vortex is weak. Hence, it is reasonable to assume that most of the shed circulation remains within the field of view, and is sucked into the grooves before the next blade arrives. In contrast, the strength of the ensemble-averaged TLV in the untreated machine increases monotonically with *s*/*c* (Li *et al.* (2016) and Figure 4-12), eventually exceeding that of the treated machine in spite of the lower pressure coefficient. This vortex is initially aligned at a shallow angle to the circumferential direction (Chapter 3 and Figure 4-5c), but the concentrated multiple vortex filaments comprising its center "break up" in the middle of the passage and scatter over a broad area (Chen *et al.*, 2017c; Tan *et al.*, 2015b). Once, the TLV becomes fragmented, the area occupied by the scattered filaments grows rapidly, eventually reaching the PS of the next blade, but only at mid-chord. Hence, the onset of stall in the untreated rotor also does not involve direct interaction of the TLV with the vicinity of the leading edge of the next blade.

Instead, in Chapter 3, it is shown that the onset of stall in the untreated rotor involves the formation of BFVs that extend diagonally upstream, from the SS mid-chord of one blade to the PS near the leading edge of the neighboring blade. They propagate to the next passage across the tip gap or around the blade LE. A sample image of a pre-stall BFV is shown in Figure 4-5c. Much larger structures that appear when the rotor is stalled are displayed in Chapter 3. The BFVs essentially disappear in the treated rotor, as the cavitation images and absence of their signature in the vorticity distributions under the TLV clearly indicate. To explain the reason for their disappearance, one must describe their origin briefly, summarizing the findings in Chapter 3. As a visual aid, Figure 4-13a shows the distribution of U_θ in the untreated passage at s/c=0.44 and φ=0.25. The layer of elevated U_θ is originated from the tip gap (and the PS) and surrounds the TLV center. The 3D vorticity distribution, determined by recoding SPIV data in a series of closely spaced planes, indicates that the radial gradients in U_θ under the TLV, e.g. at the point marked in

Figure 4-13a, are primary contributors to the formation of a layer with elevated positive axial vorticity at this location. Similarly, a layer with negative radial vorticity is associated with the axial gradients in U_θ upstream of the TLV. Combined, they create a vortical "ring" originated from the tip gap that surrounds the TLV center. A similar ring has been observed around the TLV of an axial waterjet pump, so this phenomenon is not unique to the present machine (Wu *et al.*, 2011b). Figure 4-13b is a sample image of a BFV located radially inward from the TLV during early phases of development. It also shows the *measured* direction of vorticity at the point marked in Figure 4-13b. As is evident, the BFV is parallel to the measured vorticity, confirming its origin, and both are nearly perpendicular to the TLV and the SS surface. The BFV rolls up into a distinct vortex when the vorticity layer is perturbed. As the TLV migrates away from the blade with increasing s/c, especially after it breaks up, the region of elevated U_θ expands to a substantial fraction of passage, eventually reaching the PS of the next blade. The high U_θ on the PS of the endwall in Figure 4-13a is associated with the TLV of the previous blade. As a result, the BFVs also expand intermittently to the PS of the next blade (Figure 4-5c) and then propagate across the tip gap or around the LE to the SS of this blade. Upon penetration, the BFVs delays the rollup of a TLV increases the flow angle around the LE, and trigger generation of similar vortices in the next passage. Under stall conditions, the frequency and size of BFVs increases, and they regularly expand upstream of the leading edge of the next blade.

Admittedly, as Figure 4-10k and Figure 4-11k clearly show, regions with radial gradients in U_θ (and presumably axial vorticity) also develop under the TLV of the treated machine. Hence, BFVs could still form there. However, the grooves persistently limit the axial extent of this region, preventing the region with $\partial U_\theta/\partial r>0$ from reaching the leading edge of the next blade. As a demonstration, Figure 4-14 compares the distributions of U_θ at s/c=-0.11, a short distance ahead of the LE of the blade. Without the grooves (Figure 4-14b), the elevated U_θ region extends well upstream of the blade LE (z/c_A=0). Conversely, with the grooves, U_θ is near zero around the LE (Figure 4-14a) and is negative in other phases (Figure 4-9k, Figure 4-10k, and Figure 4-11k).

There are two possible reasons for this effect: first, the high positive U_θ fluid is sucked periodically into the groove (Figure 4-14a, and Figure 4-11k). Second, the flow direction around the blade LE is influenced by the outflow from the grooves, where $U_\theta<0$. In fact, all the (z,θ) vector maps in Figure 4-6 show the diagonal "jet" exiting from the upstream end of the groove, and reaching the plane of the blade leading edge. Hence, while BFVs could roll up periodically in the $\partial U_\theta/\partial r>0$ region, they could not propagate to the next passage. Interestingly, evidence of BFVs beginning to form can be seen in the cavitation images of the treated passage at φ=0.35 (Figure 4-5b) under the TLV segment located downstream of the grooves. Finally, Wilke *et al.* (2004) argue based on RANS simulations that the delay of stall in a compressor with axial grooves is associated with weakening of the TLV. The present results agree with this observation since the formation and growth of the BFVs appear to be direct outcomes of the tip leakage flow, as well as rollup, migration, and breakup of the TLV.

Comparisons between distributions of turbulent kinetic energy (TKE) could be used as statistical means of highlighting the effect on the flow stability of the TLV suction into the grooves in the treated rotor, and penetration of BFVs across the tip gap in the untreated machine. Figure 4-15 compares sample distributions of TKE. In the tip region of the grooved endwall, the high turbulence is confined to the vicinity of the TLV (Figure 4-15a, c&e), and to the region of flow separation around the downstream corner of the groove (Figure 4-15c). Once most of the TLV is sucked into the groove, at s/c=0.66, the turbulence around the TLV remnants (Figure 4-15e) is much lower than that near the center of the fragmented TLV after it breaks up in the untreated machine (Figure 4-15f). Deeper within the groove, the TKE is substantially lower. Elevated turbulence levels, which are significantly lower than those at the entrance to the groove, also develop when the outflow from the groove interacts with the passage flow, as shown using different contour scales in the insert in Figure 4-15a. In other parts of the tip region, especially near the PS and entrance to the tip region, the TKE in the grooved machine is much lower than that in the smooth endwall. As demonstrated in Chapter 3, the high TKE near the PS and at the

entrance to the untreated tip clearance (Figure 4-15b&d) is dominated by the formation and penetration of the large BFVs across the tip gap. At higher flow rates, when the BFVs and fragmented TLV in the untreated machine does not make it to the PS of the neighboring blade, the turbulence at the entrance to tip gap is much lower.

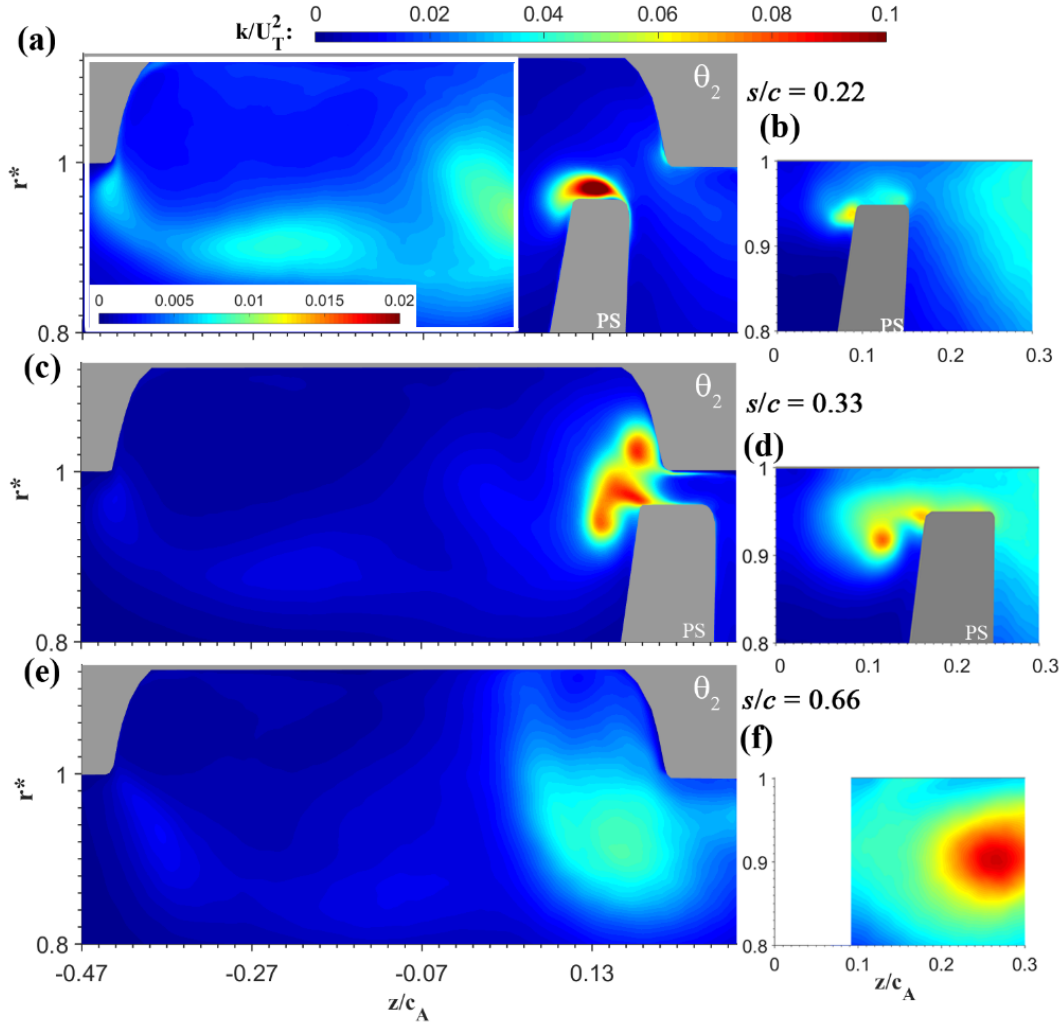

Figure 4-15 Comparison of TKE distributions with casing grooves (left column) and smooth casing (right column). (a&b) s/c=0.22, (c&d) s/c=0.33, and (e&f) s/c=0.66. Note the scale for the insert in (a) has a significantly smaller range.

The abovementioned periodic exposure to the outflow from the groove affects the flow direction near the leading edge of the blade, and presumably the blade loading. As illustrated in Figure 4-16a, in the present discussion, the relative flow angle is defined as the angle between the *z*-axis (positive axial direction) and the flow direction in the *blade reference frame*. Perpendicular views of the distribution of this angle are presented in Figure 4-16. The insert in Figure 4-16b also provides a reference distribution of this angle for a smooth endwall at the same blade orientation, with the dotted lines indicating the location of the LE. Figure 4-16a clearly shows that the outflow from the groove generates a layer with high flow angle, which propagates downstream and periodically increases the flow angle around the blade leading edge. The corresponding θ_1 and θ_2 planes (Figure 4-16b&c) show the significant radial extent of this phenomenon. Evidently, the outflow from the grooves periodically increases the relative flow angle upstream of the LE by more than 5°. This increase does not appear to cause leading edge separation, at least for the present flow conditions.

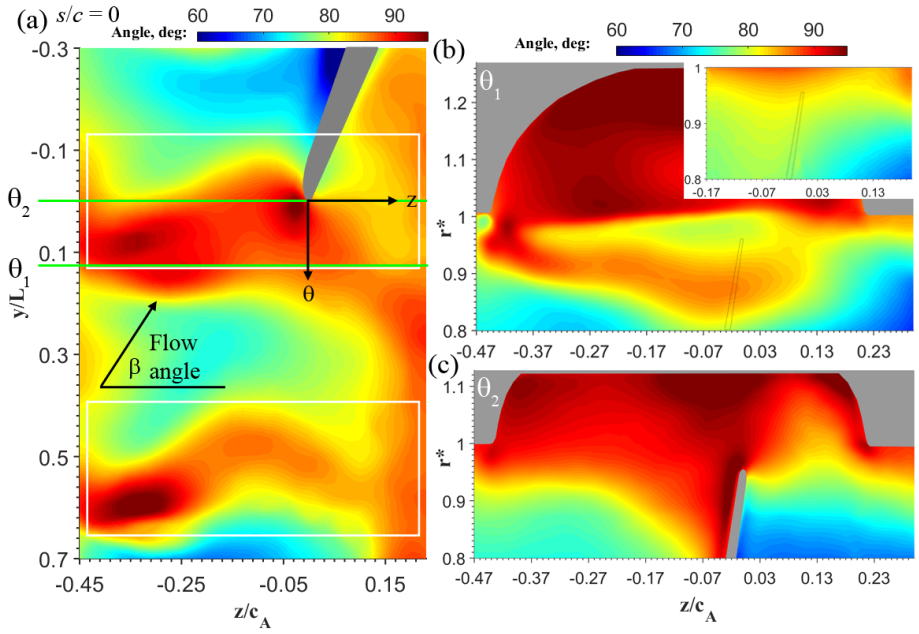

Figure 4-16 Distribution of relative flow angles in the rotor reference frame. (a) (z,θ) plane at r^*=0.96, (b&c) θ_1, θ_2 planes when the θ_2 plane is at s/c=0. Insert in (b) shows the relative flow angle in θ_1 for the untreated case.

4.3 Summary

Performance tests, flow visualization, and PIV measurements confirm that axial casing grooves suppress the onset of stall in the tip region of the NASA compressor rotor and elucidate the flow mechanisms involved. Following Müller *et al.* (2011), the semi-circular grooves are skewed by 45° in the positive circumferential direction. There are four evenly spaced grooves in each rotor passage, with 33% of the groove overlapping with the rotor blade, and the rest extending upstream. Most of the present velocity measurements and flow visualizations are performed at a flow rate corresponding to pre-stall condition for the smooth endwall. The grooves reduce the stall flow rate by 40% and cause a substantial increase in pressure rise at low flow rates. Substantial improvements in stall margin are also reported in Müller *et al.* (2011) for a transonic compressor. However, the grooves reduce the pressure rise at high flow rates. The reason for this performance degradation remains an open question that will be investigated in Chapter 5.

The velocity measurements show that a circulating flow enters the grooves at the downstream end and exits at the upstream edge, confirming prior results for axial casing grooves reported e.g., by Smith *et al.* (1984), Wilke *et al.* (2004) and Müller *et al.* (2011). The present measurements also show that the flow structure over the entire tip region and within the grooves, including the primary inflow location, varies periodically with blade orientation. The periodic outflow agrees with measurements performed by Takata *et al.* (1977). The inflow peaks when the downstream end of the groove is aligned with the PS of the blade, and decreases, but does not vanish when this end is located near the SS. Flow separation occurs at the groove corners as the flow enters and leaves the groove, creating a secondary flow there, and suggesting that the groove geometry could be optimized further. The radially and circumferentially negative outflow is concentrated at the upstream corner of the groove. When this flow propagates to the blade leading edge, it causes a periodic increase in flow angle by as much as 5°. Yet, this periodic increase does not cause leading edge separation. Although not measured, the increase in relative flow angle is

expected to increase the blade loading. Hence, it might play a role in the 17.5% increase in pressure rise under the present flow conditions. Increase in relative flow angle caused by the outflow from the grooves is consistent with trends reported by Takata *et al.* (1977), and Müller *et al.* (2011). However, the improved performance could also be associated with reduced TLV-induced blockage and/or secondary flows reported in Smith *et al.*, (1984), Crook *et al.* (1993), and Müller *et al.* (2011).

As the blade rotates past the grooves, the circulating flows entrain parts of the TLV, reducing its size and strength, as well as confining its remnants to the downstream corner of the groove. By the time the next blade arrives, the vortex signature essentially vanishes. Furthermore, the grooves prevent the formation of large-scale BFVs, which play a key role in the onset of rotating stall in the untreated rotor (Chapter 3). These vortices propagate diagonally upstream from the SS of one blade to the PS of the next blade and then to the next passage. Comparisons between the untreated and treated flows reveal likely causes for BFV disappearance in the latter. The BFVs roll up in a region of high radial gradients in circumferential velocity under the TLV and migrate to the next passage as the TLV grows and migrates away from the blade SS to the PS of the neighboring blade. By sucking the flow with high positive circumferential velocity and reinjecting it back in the negative direction, the grooves constrain the region where the BFVs can form, and prevent them from reaching the leading edge of the next blade. The distributions of turbulent kinetic energy provide statistical evidence that in contrast to the untreated casing, very little turbulence originating from a previous TLV, including the BFVs, propagates from the PS to the SS of the blade across the tip gap. Hence, the high TLV-related turbulence remains confined to the entrance to groove. Elevated, but lower turbulence is also generated as the outflow from the groove is injected into the passage.

Chapter 5 On the Interactions of a Rotor Blade Tip Flow with Axial Casing Grooves in the NASA Compressor near the Best Efficiency Point

In Chapter 4 we have shown that axial casing grooves (ACGs) are effective in delaying the onset of stall, but degrade the performance of axial turbomachines around the best efficiency point (BEP). In this Chapter, newly conducted efficiency measurements show that the ACGs cause a 2.4% peak efficiency loss. They are followed by detailed characterizations of the impact of the ACGs on the flow structure and turbulence in the tip region at high flow rates away from stall. Comparisons with the flow structure without casing grooves and at a lower flow rate (Chapter 4) are aimed at exploring relevant flow features that might be associated with the reduced efficiency. Results have shown that the entrainment of the PS boundary layer and its vorticity by the groove generates counter-rotating radial vortices at the entrance to the groove, and a "discontinuity" in the appearance of the tip leakage vortex (TLV). Interactions of this corner vortex with the TLV cause fragmentation of the latter, creating a broad area with secondary flows and elevated turbulence level. Compared to a smooth endwall, the groove also increases the flow angle near the blade tip leading edge (LE) and varies it periodically. Accordingly, the magnitude of circulation shed from the blade tip and leakage flow increase near the leading edge. The insight from these observations might guide the development of ACGs that take advantage of the stall suppression but alleviate the adverse effects at high flow rates. This work was published in the *Journal of Turbomachinery* (Chen *et al.*, 2018).

5.1 Experimental setup

The SPIV setup for measurements in meridional planes is the same as described in Figure 4-3 and Chapter 4. As shown in Figure 5-1a, in most of the present meridional plane measurements, the laser sheet is cutting through the center of the groove marked as G0 at the inner surface of the casing endwall. In Figure 5-1b, grooves located in the positive circumferential direction are named G1, G2, etc., while those located to the other direction are named G-1, G-2, etc. The particle images are recorded by a pair of Imperx B6640 CCD cameras (6600×4400 pixels) using a field of view of 46.3×42.6 mm^2. Data have been acquired at two different axial locations, covering most part of the blade passage. In Figure 5-1b, a pair of 2048×2048 pixel PCO. 2000 cameras are used to record data in two planes that are aligned perpendicularly to the radial direction in the middle of the G0 groove. Since these planes are flat, their distance from the endwall decreases with increasing θ. When the blade span is vertical, plane R1 intersects with the blade tip at $r^* = 0.96$, and plane R2 cross the radius in the tip gap at $r^* = 0.98$. Here, r^* is the normalized radial coordinate defined by Equation 2-8. The field of view is 47.9×52.43 mm^2, covering both G0 and G1, as shown in Figure 5-1a. Note that due to the casing curvature, planes R1 and R2 are located close to the entrance to groove G1, where they are no longer aligned in the radial direction. SPIV data have been recorded at two flow rates, φ=0.35 and 0.38, with the latter, as shown later, corresponding to the BEP of the untreated machine.

The blade orientation/phase is represented by the blade chord fraction (s/c), which indicates the point where the meridional plane laser sheet (at G0 center) cuts the blade chord. Data have been recorded at 14 blade phases covering an entire blade passage for each setup and each flow rate.

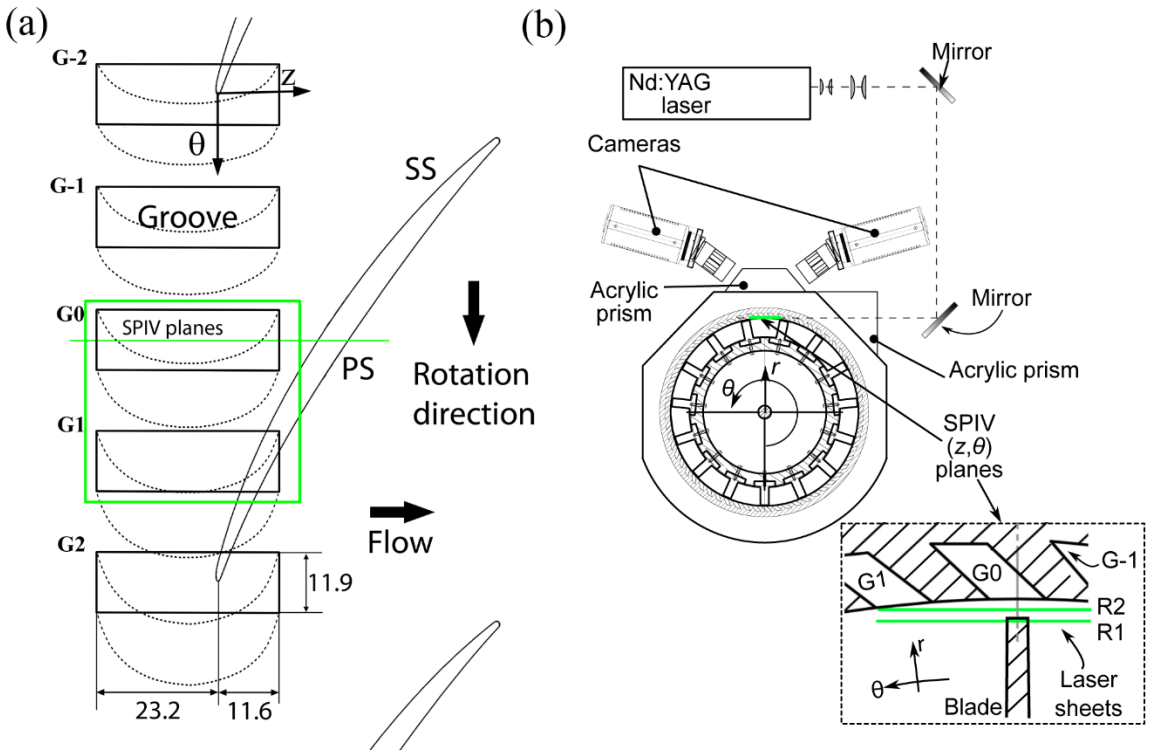

Figure 5-1(a) The ACG configurations and SPIV plane in the meridional plane. (b)Experimental setup for SPIV in (z, θ) planes.

5.2 Results and discussion

Performance and efficiency

Figure 5-2 compares the performances of the machine with and without ACGs. In Figure 5-2, the stall onset flow coefficient decreases from φ=0.25 without grooves to φ<0.15 when ACGs are installed. The most prominent mechanism causing the onset of stall in untreated endwall involves the formation of BFVs that propagate from the SS of one blade to the leading edge of the next blade. The origin of the BFVs is described in (Chen *et al.*, 2017b and Chapter 3). Installation of the grooves, as discussed in (Chen *et al.*, 2017a and Chapter 4), has three primary effects, namely suction of the TLV into the groove, periodic modifications to the flow angle (leading edge

loading), and reduction in the circumferential velocity near the leading edge of the blade, which suppresses the formation of the BFVs.

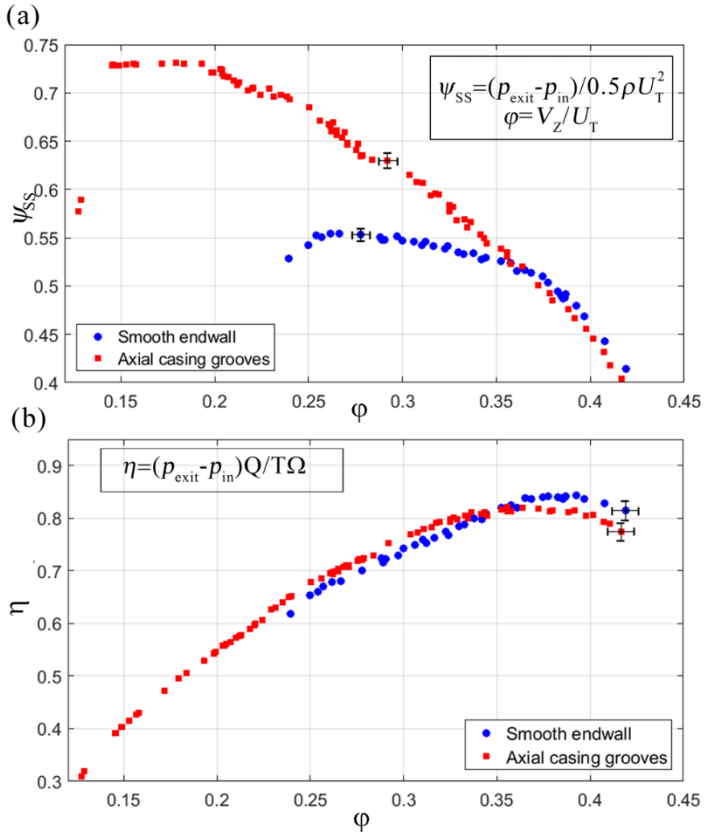

Figure 5-2 Performance curves with and without the axial casing grooves. (a) Static head rise and (b) efficiency. Circular dots represent the smooth endwall case while square dots show the data from the axial casing groove case.

However, at φ>0.36, the grooves cause a slight decrease in ψ_{SS}. Figure 5-2b shows that the BEP for the untreated machine is φ=0.38, where η=0.84. Adding the grooves causes a 2.4% decrease in efficiency at φ=0.38, and shifts the BEP to φ~0.36. The lower efficiency at φ=0.38 is associated with both a lower head rise and a higher torque. The efficiency of the two cases is almost the same at φ=0.35. At lower flow rates, the grooves cause a slight increase in efficiency, indicating that the dramatic improvements in pressure rise co-occur with a similar increase in torque.

The flow visualizations and velocity measurements have been performed at three different flow rates: φ=0.25 which corresponds to the pre-stall condition of the machine without casing groove; φ=0.35 when the two cases have similar efficiency but the head rise coefficient is higher for the grooved case; and φ=0.38 which is the BEP for the untreated rotor. The reason for focusing on φ=0.35 is the previously obtained vast database on the flow structure and turbulence without grooves under the same condition.

Flow visualization of vortical structures by cavitation

Figure 5-3a&b present two sample cavitation images at two blade phases at φ=0.35, which are aimed at highlighting the interactions of the tip region vortical structures with ACGs. In both cases, the TLV has multiple kinks. In Figure 5-3a, which corresponds to s/c=0.33, the blade mid-chord overlaps with the G0 groove corner, and the LE passes above the G1 groove. The TLV initially rolls up between G0 and G1, as indicated by the tip leakage cavitation, which indicates strong tip leakage flow (Tan *et al.*, 2015b), and the thin vortical filament is aligned with the blade SS. The insert in Figure 5-3a shows that part of a vortical structure originating from the PS is entrained into the G0 groove corner. As shown later, this entrainment is caused by an intermittent radial jet that peaks when the downstream end of the groove is exposed to the pressure side of the blade. Similar entrainment of vorticity originating from the PS have been observed at φ=0.25 (Chen *et al.*, 2017a, Chapter 3). Further along the SS, the TLV appears to be aligned with the downstream end of the G0 groove, even beyond this groove, but then starts meandering as it begins to interact with the G-1 groove. Figure 5-3b shows a different phase, corresponding to s/c=0.55. The presence of multiple structures and a discontinuity in the TLV trajectory appear to develop near the G0 groove corner. In particular, a pair of vortical structures appears to be aligned with the downstream end of this groove. The SPIV data presented later in this Chapter indicate that these structures correspond to a pair of counter-rotating vortices, the downstream one being part of the TLV, and the upstream one being a separation vortex at the groove corner. As a comparison,

Figure 5-3c shows the TLV at φ=0.38, where the noticeable leakage flow and TLV rollup occur at higher s/c compared to the images at φ=0.35, and substantial fractions of the TLV develops downstream of the grooves. Yet, the TLV is still parallel initially to the edge of the G0 groove but then has a kink before it reaches the G-1 groove.

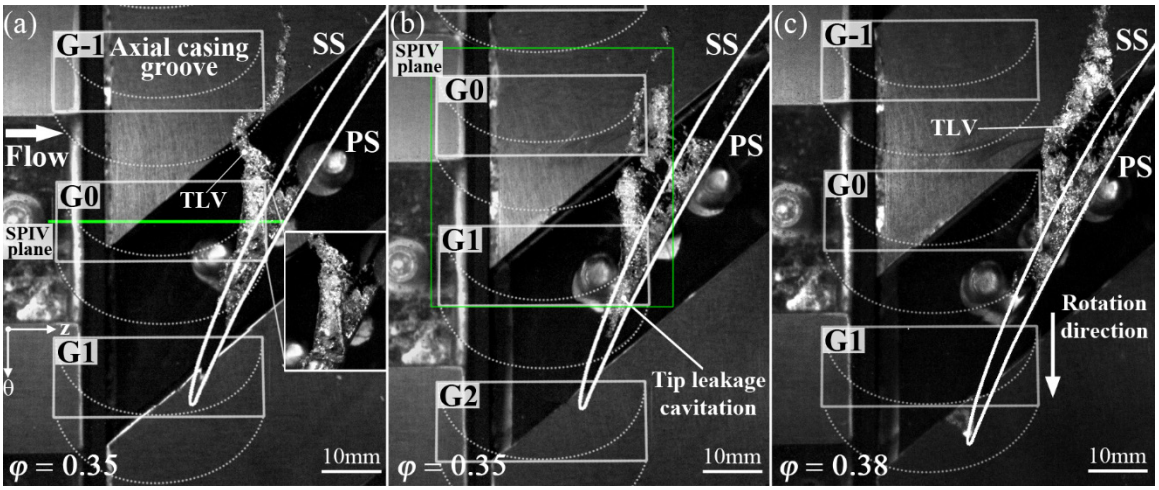

Figure 5-3 Sample cavitation images showing vortical structures in the rotor passage with ACG (a&b) at φ=0.35 for two different blade phases (s/c=0.33 & s/c=0.55, respectively), and (c) at φ=0.38. Entrances to the grooves are indicated by solid white lines, and their outlines are marked by dashed lines.

SPIV measurements in meridional planes

Ensemble-averaged circumferential vorticity distributions and vectors of in-plane velocity components (U_z, U_r) in the center meridional plane of G0, at four different phases, and at φ=0.35, with and without casing grooves, are shown in Figure 5-4. The fields of view in Figure 5-4a-d are expanded by patching results obtained at two different axial locations. In Figure 5-4a, the blade PS is aligned slightly ahead of the downstream corner of the groove, resulting in the generation of a rapid radial jet straight from the PS into the groove. This jet presumably carries with it part of the PS boundary layer vorticity, which appears to be distributed along the blade tip and to a lower extent in the SS. A distinct TLV has not formed yet, similar to the corresponding smooth endwall

trend shown in Figure 5-4e. The velocity magnitude of the outflow from the groove at $-0.4<z/c_A<-0.15$ is much lower than that in the inflow jet. Upstream of the blade, a broad shear layer containing relatively low positive vorticity is aligned parallel to the endwall and extends from the groove upstream corner to the vicinity of the blade SS. Another region with elevated vorticity and a circulating flow pattern appears downstream of the PS, starting from $z/c_A=0.4$. This region contains vorticity associated with the tip vortex of the previous blade passage. The broad region is caused by TLV breakup, as discussed in several of our previous papers (Chen *et al.*, 2017c; Li *et al.*, 2017; Tan *et al.*, 2015b; Chapter 3).

At $s/c=0.33$ shown in Figure 5-4b, the blade tip is located under the downstream corner of the groove, at nearly the same orientation relative to the G0 grooves in Figure 5-3a. Vorticity originating from the blade PS is carried in part into the groove by the still strong jet, and the rest is entrained into the SS as the TLV starts rolling up. A negative vortex containing the endwall boundary layer vorticity begins to develop as the tip leakage flow separates at the downstream corner of the groove. We refer to this structure as a corner vortex in subsequent discussions. In contrast, Figure 5-4f shows that a distinct TLV is already formed near the blade tip SS corner for the smooth endwall.

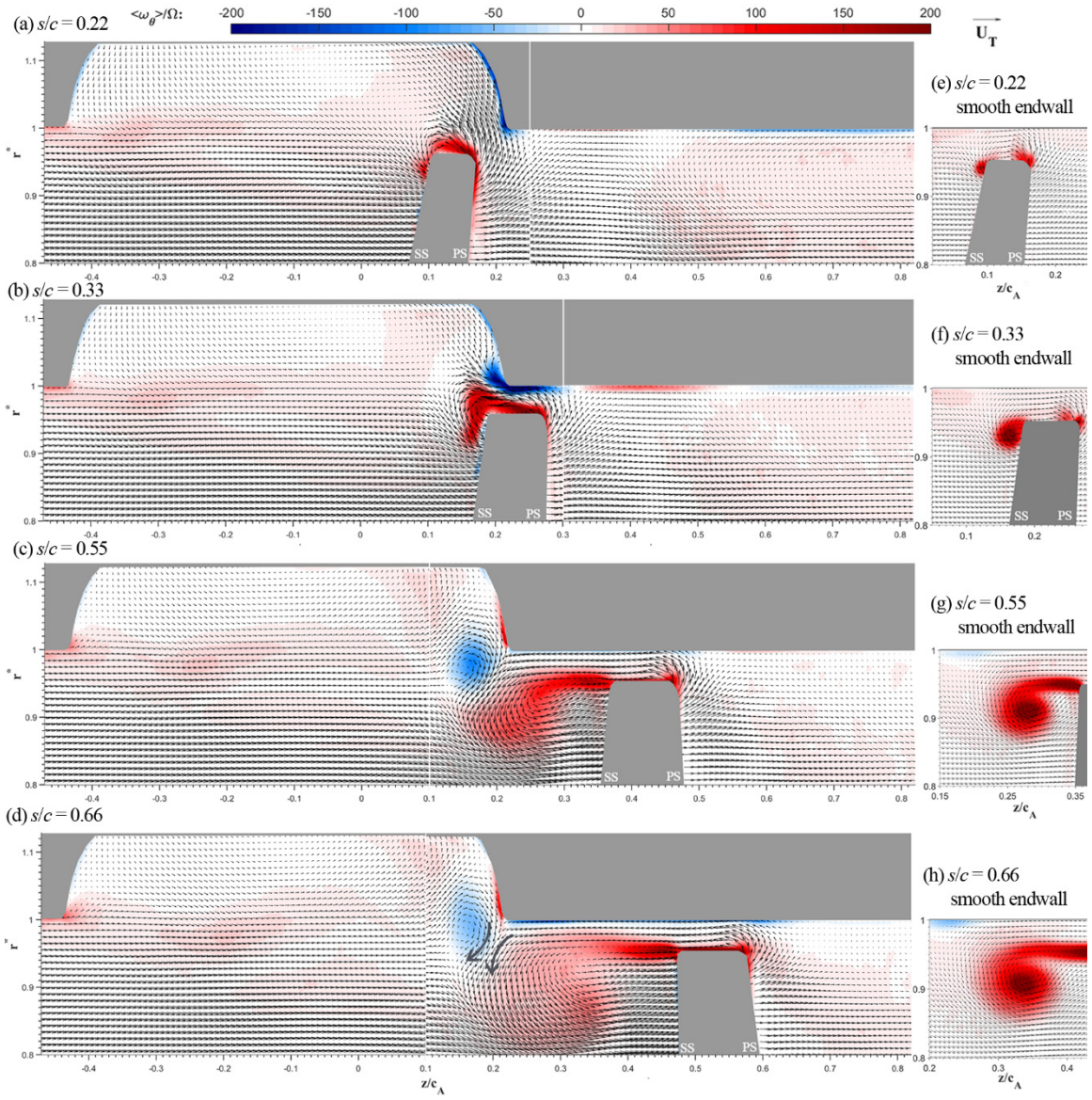

Figure 5-4 Ensemble-averaged vorticity ($<\omega_\theta>/\Omega$) distributions superimposed on vectors of (U_z, U_r) in meridional planes with casing grooves (left column) and a smooth endwall (right column) at φ=0.35. The chord wise locations are indicated above each plot along with a reference vector showing U_T. Arrows in (d) highlight the counter-rotating vortex pair. Vectors are diluted by 3:1 in both directions for clarity.

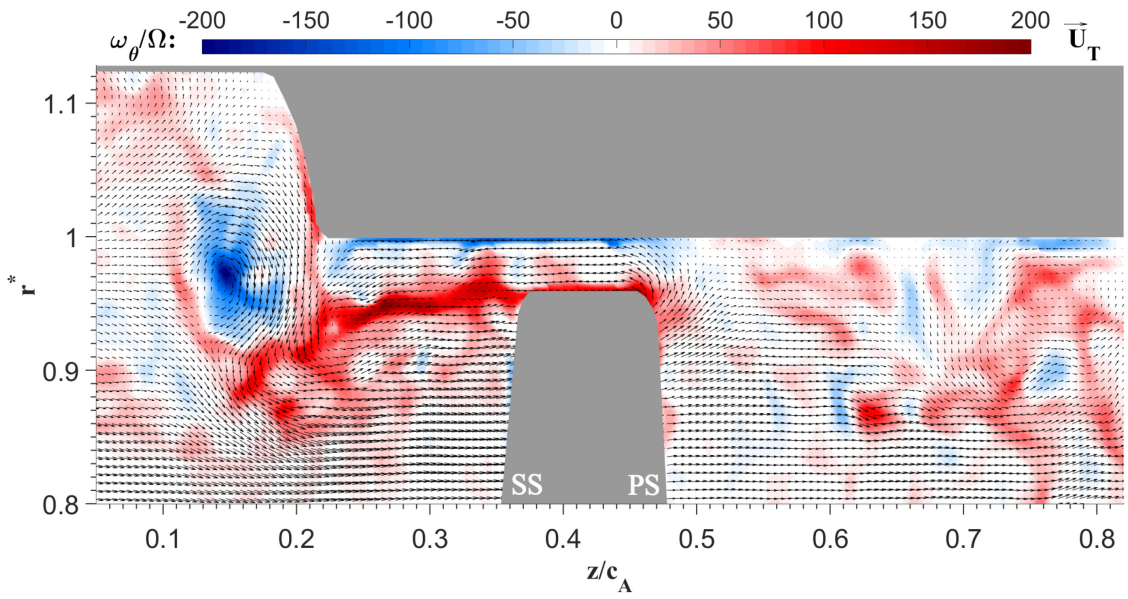

Figure 5-5 Sample instantaneous vorticity (ω_θ/Ω) and (U_z, U_r) distributions in the downstream meridional plane for s/c=0.55 and φ=0.35. Vectors are diluted by 2:1 in both directions.

In Figure 5-4c, at s/c=0.55, when the blade SS is located downstream of the groove. This phase is similar to that of the flow relative to G0 groove in Figure 5-3b. Here, the negative corner vortex grows into a large structure, which is centered radially inward from the endwall, i.e. it occupies part of the main flow passage. It forms a counter-rotating vortex pair with the TLV, which presumably corresponds to the parallel structures located on both sides of the corner evident in the cavitation image shown in Figure 5-3b. Interactions of the corner vortex with the TLV appear to have several effects. First, flow induced by the TLV is likely to be the cause for the radial inward migration of the corner vortex. Second, flow induced by the corner vortex broadens the area occupied by the ensemble-averaged TLV. Accordingly, the associated peak vorticity is substantially lower than that measured near the smooth endwall (Figure 5-4g) in spite of the higher overall circulation near the grooved endwall (data will follow). To elucidate some of the processes involved, Figure 5-5 provides an instantaneous sample at the same phase, showing that the TLV is fragmented with some of its parts forced to remain near the groove corner by flow induced by

the corner vortex. Third, at this phase, the rapid jet into the groove is diminished, and the flow around the downstream corner of the groove is driven mainly by corner vortex. Consequently, there is radial inflow into the groove at $0.1<z/c_A<0.15$, and negative radial velocity (outflow) near the corner. The velocity in the rest of the groove is much lower implying that most of the tip-groove interactions are concentrated at the downstream corner. In addition, Figure 5-4c&d display additional notable trends. First, there is a low-speed radial flow into the groove near its upstream end, at $z/c_A\sim-0.43$, which exits from the groove well upstream of the blade, around $z/C_A=-0.3$. Hence, the associated shear layer becomes wavy. Second, downstream of the blade, a circular flow with elevated vorticity, which is associated with the TLV of the previous blade, has already reached the PS of the blade.

At $s/c=0.66$, Figure 5-4d shows that the blade section aligned with the sample meridional plane is already located "far" downstream of the groove. Yet, the counter-rotating vortex pair persists, but with lower peak vorticity. The area containing positive vorticity associated with the TLV is larger than that observed in at lower s/c and much larger than the size of the TLV of the smooth endwall (Figure 5-4h), where the TLV is still compact and has higher peak vorticity. The axial extent of the huge area covered by positive vorticity associated with the TLV still starts near the groove corner, while the center of swirl moves downstream. The radial extent of this region also expands to $r^*<0.8$. However, the inflow and outflow around the downstream corner of the groove is still dominated by the corner vortex.

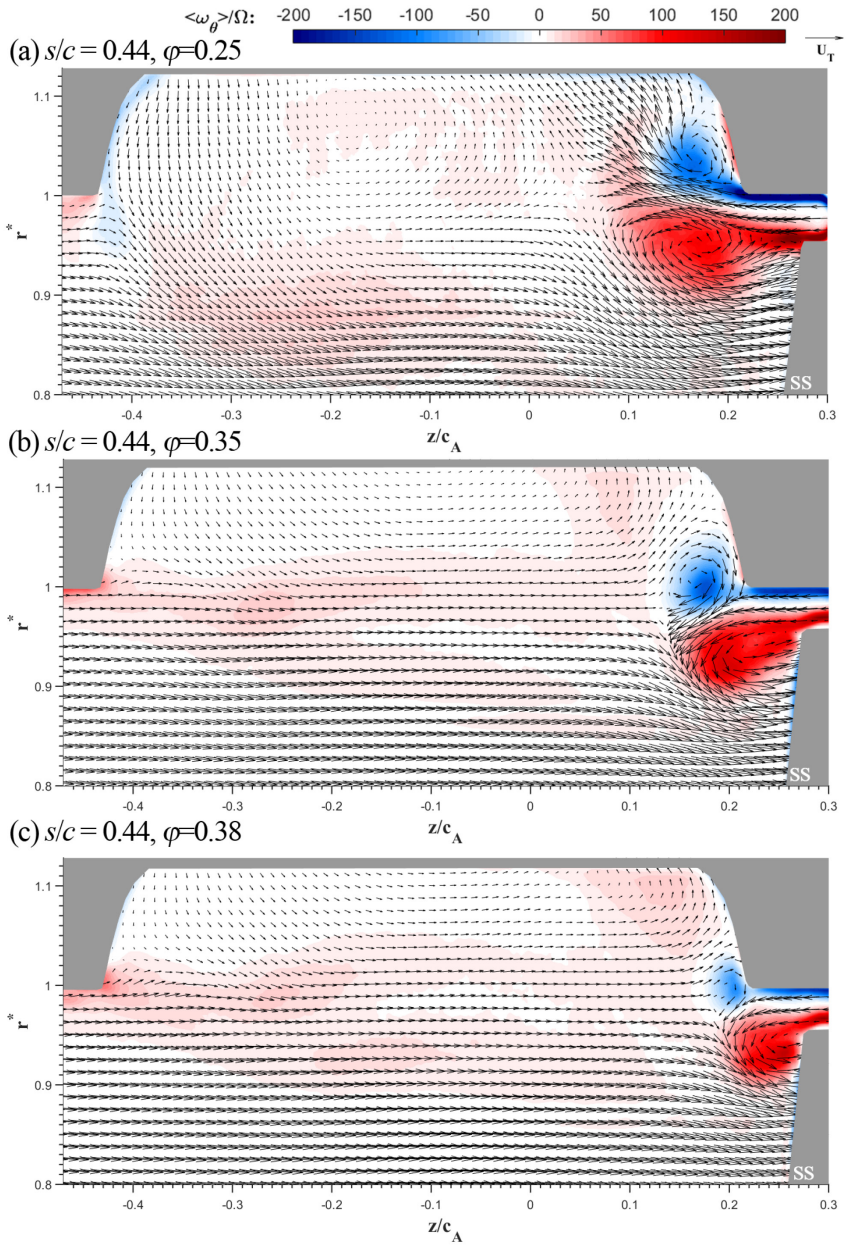

Figure 5-6 Effect of flow rate on the distributions of $<\omega_\theta>/\Omega$ (contour) superimposed on vectors of (U_z, U_r) at s/c=0.44. The flow rate is indicated above each plot. (a) φ=0.25, (b) φ=0.35 and (d) φ=0.38. Vectors are diluted by 4:1 in both directions.

To demonstrate the influence of flow rate on the flow around the groove corner, Figure 5-6 compares the flow fields at φ=0.25, 0.35 and 0.38, all at s/c=0.44. At φ=0.25 (Figure 5-6a), there is still a strong inflow into the groove in the downstream end, and an outflow at the upstream

end, which extends deeper into the passage. Accordingly, the entire corner vortex is located inside the groove, and there is no radial outflow at the downstream end. This fast inflow entrains part of the blade circulation into the groove, preventing it from being rolled up into the TLV. Consequently, the TLV circulation starts to decrease starting at mid-chord (Chen *et al.*, 2017a, Chapter 4). Additional data for this flow rate at other phases can be found in (Chen *et al.*, 2017b, Chapter 3). The distributions of $<\omega_\theta>$ at φ=0.35 and 0.38 (Figure 5-6b&c, respectively) contain a corner vortex and a radial outflow at the downstream corner, but the size and strength of this structure decrease with increasing flow rate. Furthermore, consistent with the delayed TLV rollup and leakage flow observed in the cavitation images, the TLV strength and area also decrease with increasing flow rate, at least up to s/c=0.44. In the upstream end of the groove, the direction flow changes from a strong outflow in the upstream at φ=0.25 to a weak inflow into the groove at φ=0.35, which increases slightly at φ=0.38 (discussion follows). Finally, the shift in the location of the corner vortex with increasing flow rate impacts the flow at higher chord fractions as well. In particular, Figure 5-7 shows that for φ=0.38 and at s/c=0.66, the negative corner vortex is already located within the passage. In contrast, at φ=0.35 and the same location, Figure 5-4d shows that only the bottom half of this structure is inside the main passage. At even higher s/c (not shown), the clear elevated negative vorticity region upstream of the TLV persists at φ=0.38 all the way to the trailing edge of the blade. Conversely, a diminishing signature of this corner vortex remains latched to the groove corner at φ=0.35. It is worth noting that for the smooth endwall and present tip gap, the negative vorticity originating from the endwall boundary layer remains near the casing, and is not entrained away from the wall by the TLV (Figure 5-5g&h, Li *et al.* (2016)).

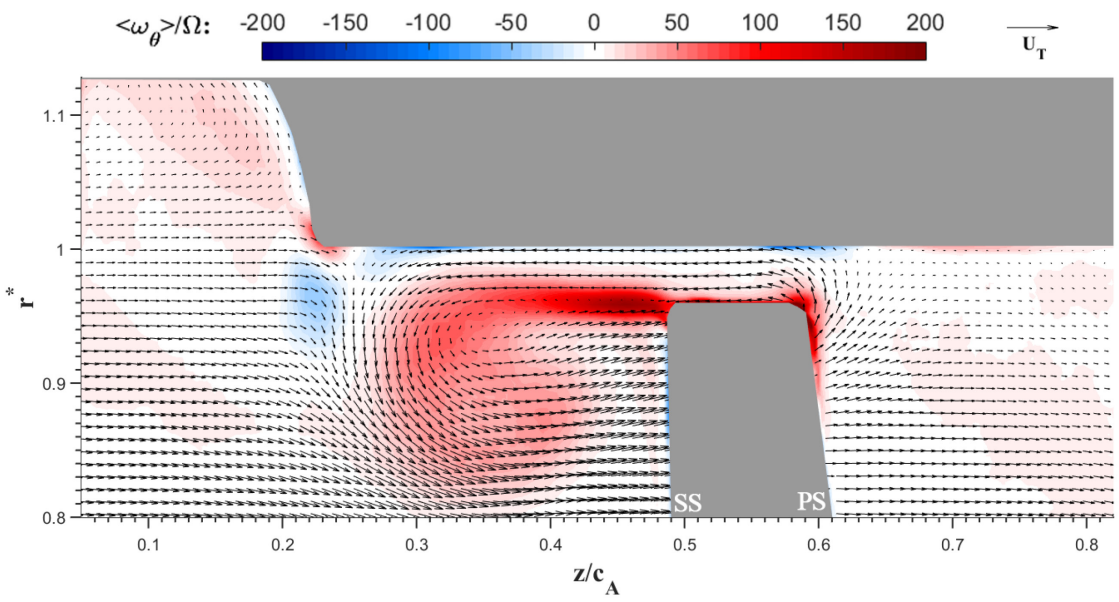

Figure 5-7 The distributions of $<\omega_\theta>/\Omega$ around the blade tip for s/c=0.66 and φ=0.38. Vectors are diluted by 3:1 in both directions.

SPIV measurement results – ***(z, θ) planes***

Figure 5-8 provides contours of U_r and $<\omega_r>$ and vectors of (U_θ, U_z) in the *(z, θ)* planes located at r^*=0.96 and 0.98 (see Figure 5-1b), all for s/c=0.33 and φ=0.35. This phase corresponds to those in Figure 5-3a and Figure 5-4b. The r^*=0.96 plane in Figure 5-8a nearly coincides with the blade tip. The positive U_r along most of the blade PS indicates radial flow into the tip gap. The elevated U_r in the PS area coinciding with the G1 groove represents inflow into the groove. The r^*=0.98 plane coinciding with the tip gap shown in Figure 5-8b displays a strong radial inflow jetting into the G0 groove in the high θ (high y/L) edge of the downstream corner, where the blade PS is located just beyond the groove. It also shows radial inflow into the G1. The outflow from both grooves, with negative U_r, is concentrated near the high θ region of the upstream corners. The sharp transition in the sign of U_r along the blade SS in Figure 5-8a is induced by the TLV and can be used to identify its trajectory. Similar to the cavitation image in Figure 5-3a, the TLV has a kink at the high θ corner of the G0 groove, at the same location as the strong radial inflow into

the groove (Figure 5-8b). The negative U_r upstream of the radial jet is induced by the TLV, which at this phase is located above the blade tip, consistent with the $<\omega_\theta>$ distributions presented in Figure 5-4b. The radial vorticity distributions in the tip gap (r^*=0.98, Figure 5-8d) show that the jet is bounded by a pair of counter-rotating vortices, but there is no sign for this vortices at r^*=0.96 (Figure 5-8c). This phenomenon is caused by entrainment into the groove of the PS vorticity by the radial jet. Figure 5-8e is a qualitative visual aid aimed at illustrating this process. The PS boundary layer vorticity has positive $<\omega_\theta>$. When this vorticity is pulled into the groove at the corner, it creates counter-rotating vortex filaments that cross the radial plane coinciding with the tip gap (Figure 5-8d), but has limited signature in the r^*=0.96 plane (Figure 5-8c) except for a mild change in the sign of $<\omega_r>$ on the PS. The fast entrainment of flow originating from the PS is also consistent with the cavitation image in Figure 5-3a. In fact, there are two possible origins for the positive circumferential vorticity appearing near the PS corner of the blade tip. The first is the PS boundary layer, and the second involved entrainment of upstream parts of the endwall boundary layer by the blade PS, which prior publications refer to as a scraping vortex (Inoue *et al.*, 1989). Given the present relatively large gap as well as the fact that the elevated PS positive vorticity appears well below the (e.g. Figure 5-4), we believe (but cannot verify) that the PS boundary layer is the primary origin of the positive vorticity near the PS corner.

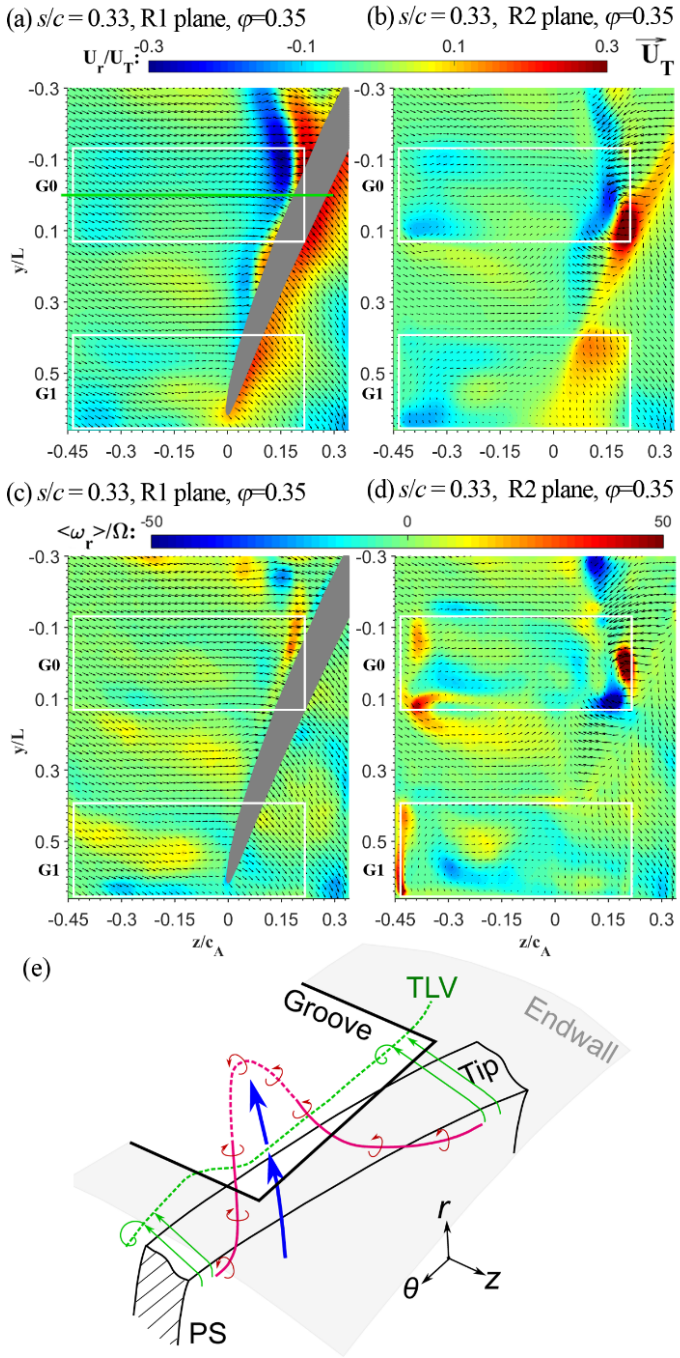

Figure 5-8 (a-d) Ensemble-averaged in-plane velocity vectors (nearly U_z, U_θ) superimposed on contours of the radial velocity (top row) and radial vorticity (second row) components at s/c=0.33 and φ=0.35. Left column: r^*=0.96. Right column: r^*=0.98. Vectors are diluted by 4:1 in both directions. (e) A sketch illustrating the vortex-groove interactions.

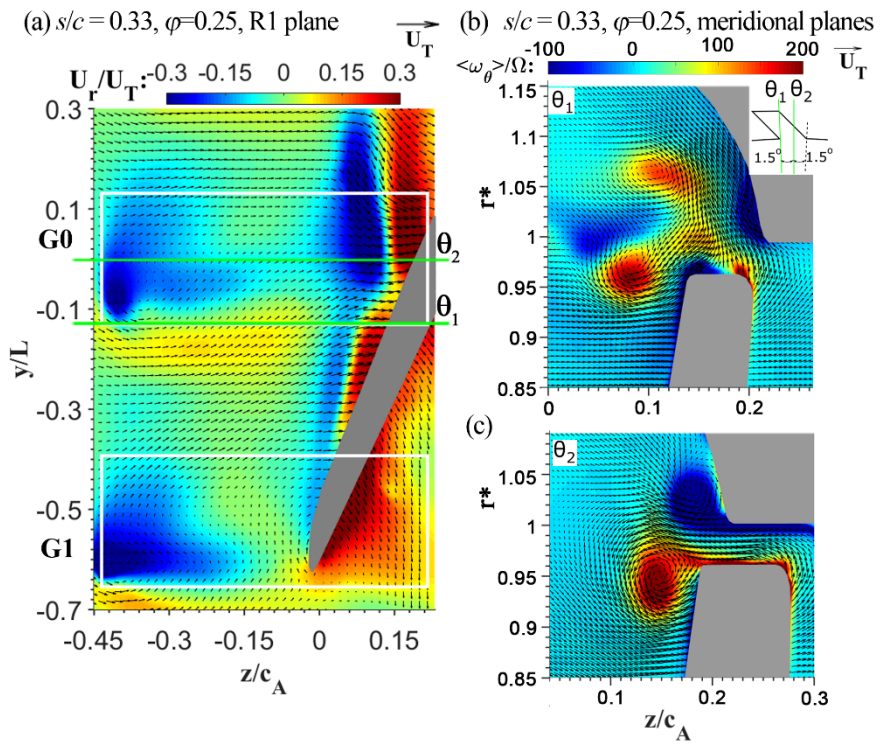

Figure 5-9 Flow features at s/c = 0.33 and φ=0.25 illustrating the vortex-groove interactions. (a) U_r contours in a radial plane at r^*=0.96. (b&c) $<\omega_\theta>/\Omega$ distributions at two meridional planes.

To further understand the impact of entrainment of vortex filaments into the groove caused by the rapid jetting, Figure 5-9 provides sample results for φ=0.25 and s/c=0.33. The U_r distributions at r^*=0.96 and φ=0.25 (Figure 5-9a) show similar kinks in the TLV trajectory along the blade SS and radial jetting into the grove when the blade PS is aligned with the downstream end of the groove. However, the radial velocity magnitudes are much higher than those measured at φ=0.35, consistent with the increased blade loading with decreasing flow rate and the results presented in Figure 5-6. Figure 5-9b shows the distributions $<\omega_\theta>$ and (U_z, U_r) in the θ_1 meridional plane, which intersects with the entrance to the groove close to its high θ corner, as illustrated in the insert. This plane is located in the same area as the high-speed radial jet discussed before, enabling us to observe the flow structure in this region. Several phenomena are evident from Figure 5-9b. First, a high-speed jet originating from the blade PS penetrates into the groove.

Second, apart from the distinct TLV near the blade SS, another vortex with $<\omega_\theta>$ >0 originating from the blade PS is located inside the groove, at the upstream edge of the jet. There is no sign of the positive vortex in the θ_2 plane cutting through the groove center, and the corner is dominated by the corner vortex. These observations along with those seen in Figure 5-8a-d are consistent with the illustration presented in Figure 5-8e. As part of the PS vorticity is entrained into the groove by the jet, instead of rolling up into the TLV, it alters TLV trajectory, keeping the vortex concentrated near the downstream corner of the groove. Note that the variations in the magnitude of U_r along the blade SS might also be affected by radial variations in the location of the TLV center evident by comparing the radial location of the TLV in Figure 5-9b&c. In Figure 5-9b the TLV center is located above the r^*=0.96 plane, but at the center of the groove (Figure 5-9c) the TLV center nearly coincides with this plane.

The tip flow-groove interactions at s/c=0.55 and φ=0.35 are shown in Figure 5-10. Here, the blade SS is located downstream of the G0 groove, as shown also in Figs. 4b and 5c. At r^*=0.96 (Figure 5-10a), the TLV signature still has a discontinuity near the high θ corner of the G0 groove. However, in this case, the same area has a strong flow aligned almost perpendicularly to the blade chord. This flow is much weaker in the r^*=0.98 plane (Figure 5-10b), where TLV signature essentially disappears. Instead, the radial velocity in the downstream corner of the G0 groove shows a transition from positive to negative U_r, consistent with the flow induced by the corner separation vortex, as shown in Figure 5-4c. Figure 5-10b also shows the rapid change in the direction of U_z as the tip leakage flow meets the incoming main passage flow, also consistent with the meridional plane data (Figure 5-4c). In this phase, both the inflow and outflow from G0 groove are weak. However, consistent with the blade location, there is still strong jetting into the G1 groove in the region where it is exposed to the blade PS, and accordingly, a higher outflow from the upstream end.

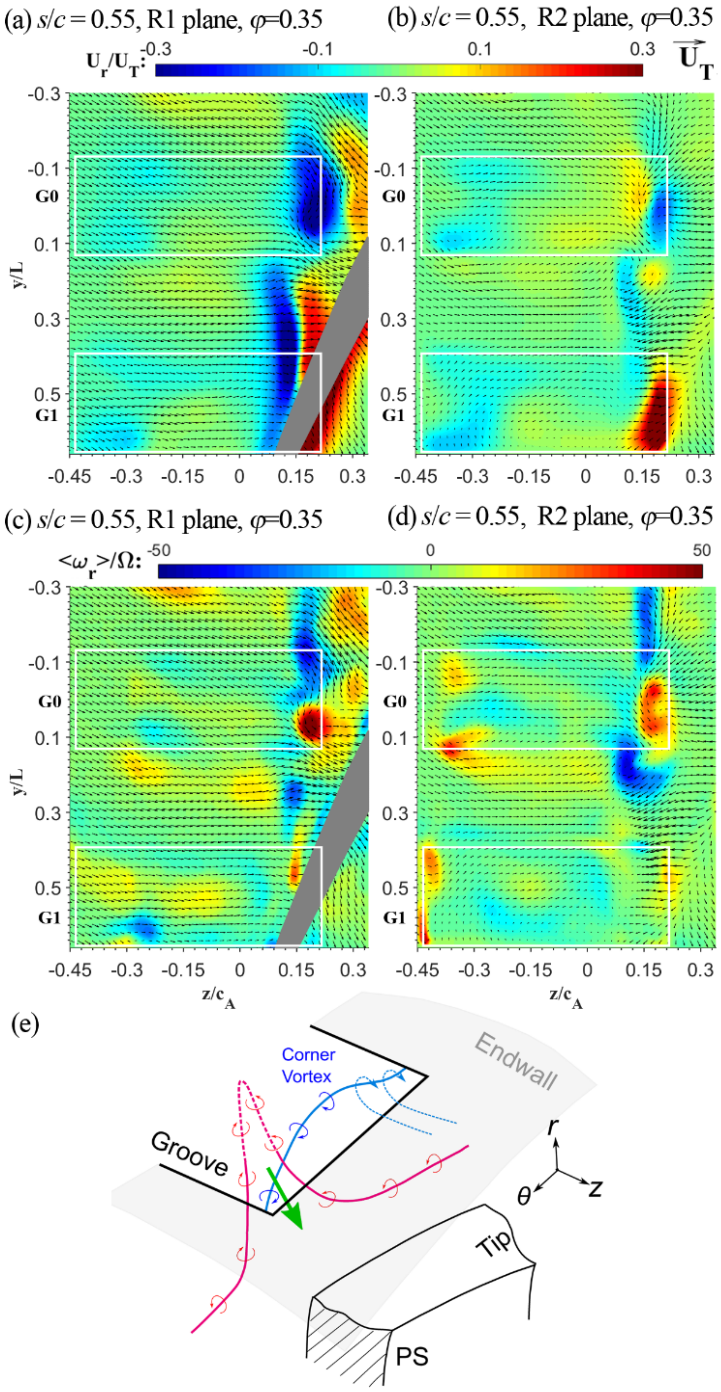

Figure 5-10 (a-d) Ensemble-averaged in-plane velocity vectors (nearly U_z, U_θ) superimposed on contours of the radial velocity (top row) and radial vorticity (second row) components at s/c=0.55 and φ=0.35. Left column: r^*=0.96; right column: r^*=0.98. (e) A sketch illustrating the vortex-groove interactions.

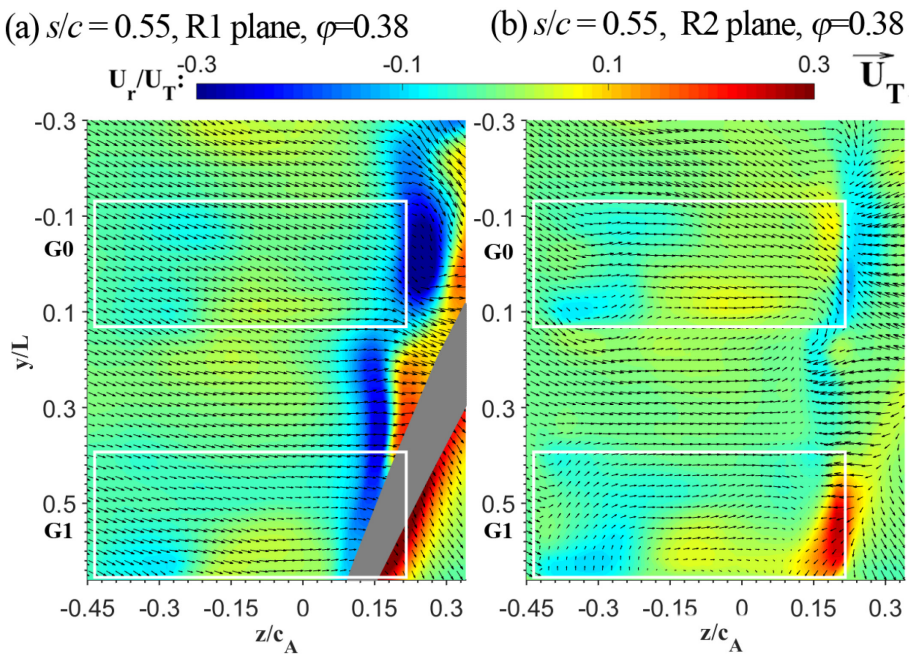

Figure 5-11 Ensemble-averaged in-plane velocity vectors (nearly U_z, U_θ) at (a) r^*=0.96, and (b) r^*=0.98 superimposed on contours of the radial velocity at s/c=0.55 and φ=0.38.

The $<\omega_r>$ distributions in Figure 5-10c&d show more complicated vortex-groove interactions. First, in Figure 5-10c, a positive radial vortex is located in the middle of the G0 groove downstream end. It is bounded on both sides with regions containing negative $<\omega_r>$. The high-speed flow perpendicular to the blade chord is bounded by the positive vortex on one end and a weaker negative vortex on the other. In Figure 5-10d, at r^*=0.98, the previously discussed vortex pair observed at s/c=0.33 appears to persist in this phase as well. However, the positive vortex in the middle of the groove might also be related to the negative vorticity layer/line appearing at $y/L<-0.1$. The qualitative illustration in Figure 5-10e is an attempt to provide a plausible explanation for these observations. The red vortex line is similar to that observed at s/c=0.33 and discussed before. It is formed initially by the entrainment of the PS vorticity, but due to the low flow into the groove in subsequent phases, it persists near the downstream corner of the groove. In addition, the blue vortex line in Figure 5-10e corresponds to the corner vortex with $<\omega_\theta><0$ resulting from the endwall boundary layer separation. This structure migrates radially

outward in the middle of the groove, consistent with Figure 5-4c, but has to connect with the endwall boundary layer at a lower r on both sides of the groove. The combined effect of these two 3D structures appears to be consistent with the velocity and vorticity distributions presented in Figure 5-10a-d. Both structures contribute to the positive $<\omega_r>$ in the middle of the groove and the negative $<\omega_r>$ on both sides of the groove. However, one should keep in mind that the proposed plausible illustration in Figure 5-10e has to be proven either by volumetric three-dimensional velocity measurements using, e.g., tomographic PIV or by systematic measurements in a series of closely spaced parallel planes.

Samples characterizing the interactions of the tip flow with the groove at φ=0.38 and s/c=0.55 are presented in Figure 5-11. Except for differences in magnitudes and a slight shift in locations, the depicted flow structure is similar qualitatively to that recorded at φ=0.35 (Figure 5-10a&b). The TLV discontinuity is evident in Figure 5-11a, where the downstream shift in the location of the TLV center is consistent with Figure 5-6c. The weaker signature of the corner vortex, as well as the flow jetting into the G1 groove can be seen in Figure 5-11b. On the upstream end, Figure 5-11b shows that there is a radial outflow from the corners/edges of the grooves and a weak inflow in the middle of the grooves. The magnitude of this outflow is weaker and that of the inflow is stronger than those at φ=0.35 (Figure 5-10b).

Changes in flow angle and blade loading

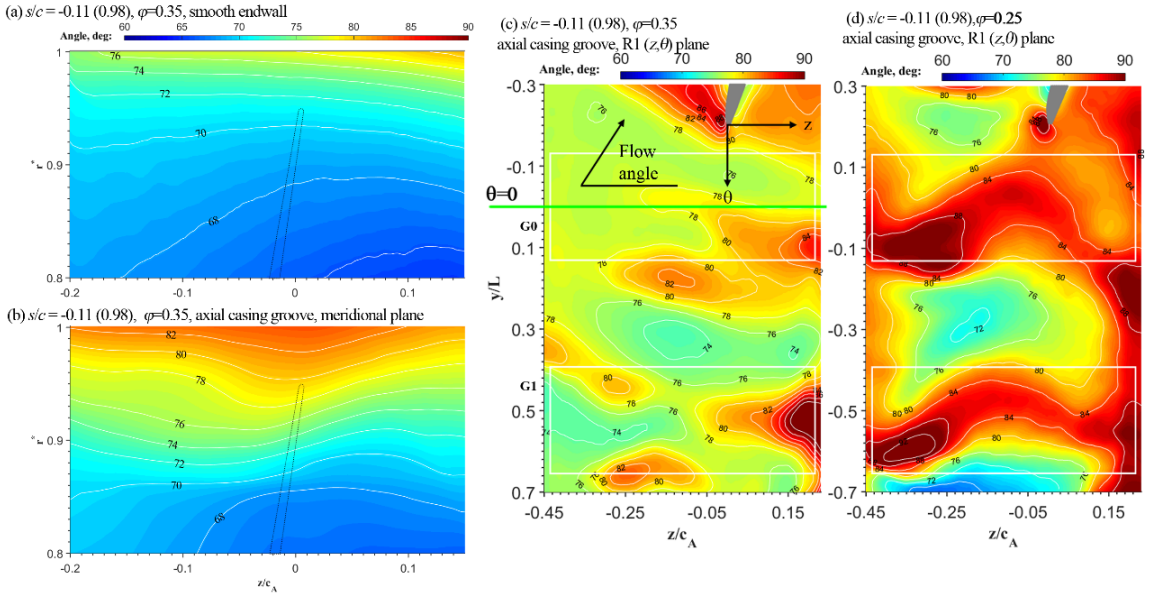

Figure 5-12 Distributions of relative flow angles in the rotor reference frame at s/c=−0.11 and φ=0.35 in meridional planes (a) without and (b) with casing grooves, and (c) in (z, θ) plane at blade tip with casing grooves. Results from φ=0.25 are shown in (d) for comparison. Dashed lines in (a&b) indicate the location of the blade LE at s/c=0.

Figure 5-12a&b compare the distributions of flow angle in the rotor reference frame at φ=0.35 without (Figure 5-12a) and with (Figure 5-12b) ACGs in a meridional plane located upstream of the blade LE (s/c=−0.11). For convenience, the location of the blade LE, which is about to enter the field of view is marked by dashed lines. As is evident, in the tip region, the grooves increase the flow angle close to the blade LE by a maximum of 7°. This increase diminishes with decreasing radial location and is hardly noticed at r^*<0.84, indicating that interactions with groove only affect less than 16% of the blade span. A radial view of the flow angle at r^*=0.96 under the same conditions is provided in Figure 5-12c. As is evident, as the blade tip LE travels across the grooves, it experiences peak to peak periodic fluctuations in flow angle of around 5°. For comparison purposes, Figure 5-12d demonstrates the periodic variations in flow angles at φ=0.25, which is discussed in (Chen *et al.*, 2017a, Chapter 4). Here, the faster outflow

from the groove increases the peak-to-peak variations in flow angle to 10°. The radial extent of these variations is also higher at φ=0.25, consistent with Figure 5-6a&b. These observations confirm that the influence of the groove on the flow around the blade LE increases with decreasing flow rate.

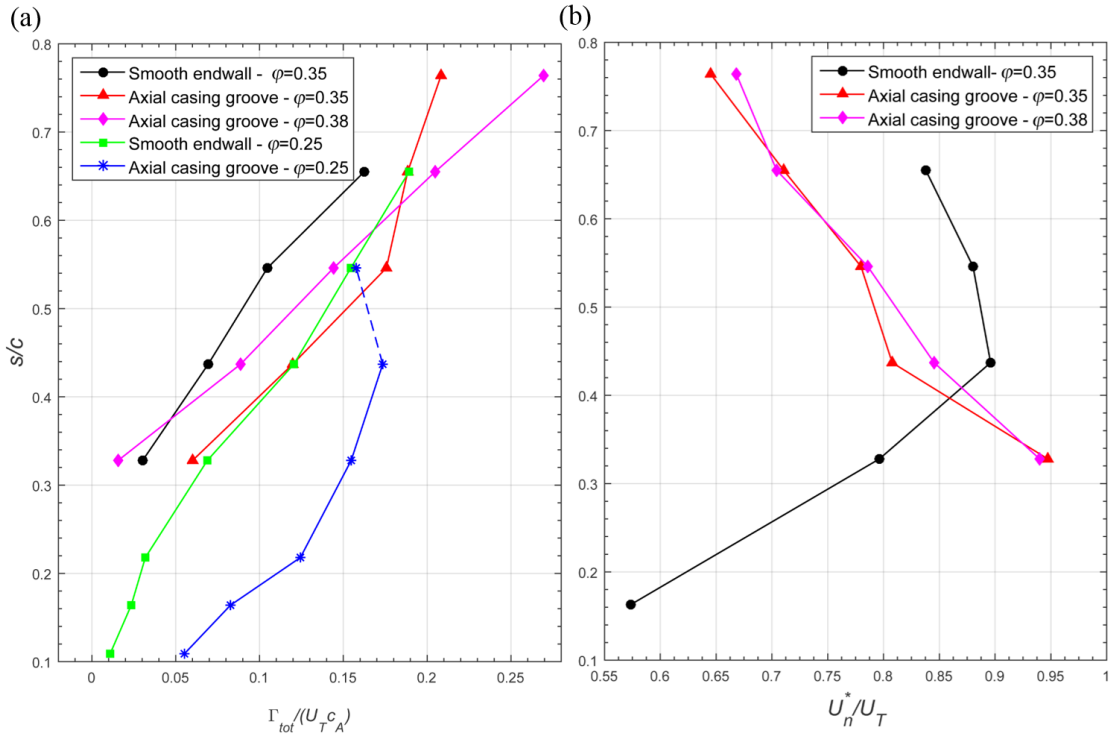

Figure 5-13 Comparisons of (a) total positive circulation at blade SS and (b) tip leakage flow strength normal to the blade chord with and without casing grooves.

Figure 5-13 examines the effects of the ACGs on the magnitudes of positive circulation on the blade SS (Figure 5-13a), and the tip leakage flow (Figure 5-13b). The circulation is calculated by integrating the circumferential vorticity in the regions that it is positive over the entire SS. Unlike in Chapter 4, we do not attempt to separate between vorticity entrained into the TLV and that located in the shear layer connecting the TLV to the SS tip corner since the boundary between them is fuzzy. The tip leakage flow strength, denoted as U^*_n is obtained by (radially) averaging the velocity across the tip gap in a direction normal to the blade chord in the rotor

reference frame. Due to variations in the blade location relative to the groove, at s/c=0.33 the leakage velocity is integrated in a plane coinciding with the downstream corner of the groove. In other phases, the calculation is based on integration along the SS tip corner. As is evident from Figure 5-13a, at φ=0.25 and 0.35, the circulation in the grooved endwall is persistently higher than those of the smooth endwall. While the periodic entrainment of the TLV into the groove at φ=0.25 decreases the TLV strength at mid-chord (Chen *et al.*, 2017a, Chapter 4), at φ=0.35, the circulation keeps on increasing, but at a slower rate at s/c>0.55. This slower growth rate downstream of the groove suggests a reduction in blade loading in the aft part of the blade. Hence, in spite of the entrainment of parts of the TLV into the groove, the remaining parts are still stronger than those of the smooth wall. This trend suggests that the groove causes an upstream shift in blade loading. Increasing the flow rate to φ=0.38 reduces the TLV strength at low s/c, but the growth rate does not appear to diminish in the aft parts. Examination of the trends of leakage velocity is another way of evaluating the variations in blade loading since U^*_n is expected to increase with pressure difference across the blade. Figure 5-13b shows that for φ=0.35 and at s/c=0.33, the grooves increase the tip leakage velocity significantly, consistent with higher circulation there, and the previously mentioned shift in blade loading towards the leading edge of the blade. This shift is consistent with the higher flow angle (Figure 5-12) near the LE. For the smooth endwall, the leakage peaks at s/c=0.44, and decreases slowly further along the blade. Conversely, for the grooved endwall, U^*_n decreases monotonically in our measurement range. This decrease is also consistent with the change in the slope of the circulation at φ=0.35 at mid-chord. The profiles of U^*_n at φ=0.38, for which we do not have data without grooves, are similar to those at φ=0.35.

A note on the distribution of turbulence

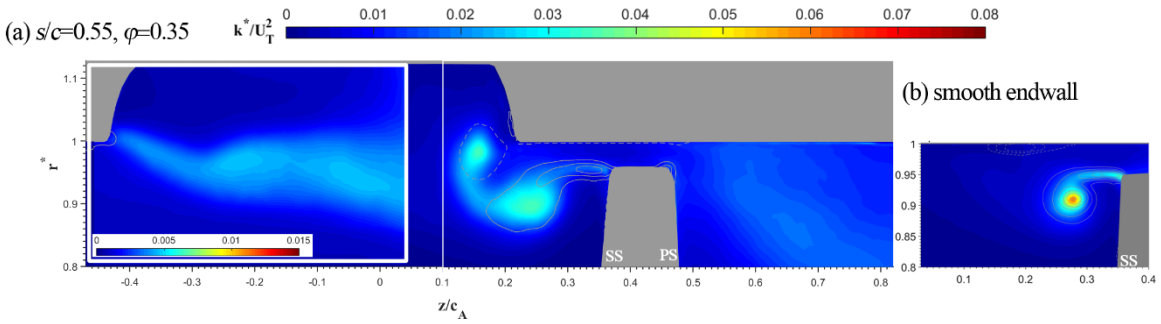

Figure 5-14 Distribution of turbulent kinetic energy (a) with and (b) without axial casing grooves at s/c=0.55 and φ=0.35. Note the scale for the insert in (a) has a significantly smaller range. Contour lines show the circumferential vorticity.

Figure 5-14 provides a sample comparison of TKE distributions with (Figure 5-14a) and without (Figure 5-14b) casing grooves. The TKE level is high around the centers of the TLV and corner vortex, as well as in the shear layer connecting the TLV to the SS corner. The area with elevated TKE in the grooved endwall case is much broader than that of the smooth casing, but the peak value near the TLV center and in the shear layer is lower. The wide area with elevated TKE in the PS of the blade in Figure 5-14a is associated with remnants of the TLV originating from the previous blade. Similar phenomena have been observed before for the smooth endwall as well (Chen *et al.*, 2017b; Li *et al.*, 2016). Using a significantly different scale, Figure 5-14a also shows that the TKE is elevated in the shear layer originating from the upstream end of the groove and separating between the main passage flow and slow circulating flow inside the groove. This elevated turbulence representing a loss of mean flow kinetic energy is likely to adversely influence the efficiency of the machine.

5.3 Summary

Consistent with previous studies (Beheshti *et al.*, 2004; Seitz, 1999; Wilke *et al.*, 2004), the axial casing grooves effectively delay the onset of stall at low flow rates, but degrade the performance of the machine around the best efficiency point. SPIV measurements and flow visualizations have been used for investigating the flow mechanisms involved and comparing them to those observed near a smooth endwall. The skewed semicircular, four-per-passage ACGs are based on those described in Müller *et al.* (2011). They partially overlap with the rotor blade LE, and the rest extend upstream. The present measurements have been performed close to and at the BEP. The complement data obtained under the pre-stall conditions of the untreated rotor (Li *et al.*, 2016), and previous measurements at low flow rates using the same grooves (Chapter 4, Chen *et al.* (2017a)). Combined, the extensive experimental database elucidates many of the complicated interactions of the blade tip flow with the grooves.

While it is difficult to summarize all the observed phenomena in a few sentences, several appear to be particularly important. The radial inflow into the groove peaks periodically when the blade PS is aligned with downstream corner of the groove. The resulting rapid radial jet entrains vorticity originating from the PS boundary layer into the groove, preventing it from rolling up into the TLV. This process forms a three-dimensional structure that appears as a counter-rotating pair of radial vortices at the entrance to groove and causes a kink in the TLV trajectory. During this period, there is a weak outflow from the upstream end of the groove. The inflow into the groove diminishes when its downstream end is exposed to the blade SS. Instead, separation of the endwall boundary layer as the backward leakage flow reaches the downstream corner of the groove generates a large corner vortex, which rotates in the opposite direction of the TLV. At low flow rates, this corner vortex is forced into the groove, and has a limited influence. Conversely, near the BEP, as the PS driven inflow into the groove diminishes, interactions of the corner vortex with the TLV become the dominant flow phenomenon. At φ=0.35, this corner vortex lingers around

the downstream corner of the groove, causing fragmentations of the TLV, and generating a broad area with high turbulence level. At φ=0.38, the corner vortex remnants migrate away from the groove together with the TLV and can be detected even at the blade trailing edge.

During periods of increased inflow, there is also a weak outflow from the upstream end of the groove. However, in other phases, most of the high secondary flows are confined to the downstream corner, and the flow in the rest of the groove is limited to slow circulation with a growing shear layer separating it from the main passage flow. This process persists until the next blade arrives. The grooves also increase and cause periodic variations in the flow angle near the blade tip LE. Accordingly, the magnitudes of circulation shed from the blade tip and leakage flow also increase near the leading edge. These observations might guide potential improvements to the geometry of the grooves that would (e.g.) prevent the lingering effect of the corner vortex at high flow rates.

Finally, this Chapter concludes with a discussion about possible mechanisms that would cause a reduction in efficiency of the grooved machine at high flow rates. While the flow around the grooved endwall is extremely complex and the present measurements examine only a few sections of the flow domain, the database enables us to identify several of the key phenomena: First, the periodic outflow from the groove increases the blade incidence angle, and appear to shift the blade loading upstream, as confirmed by the increase in leakage velocity and TLV circulation. Such an upstream shift also occurs with decreasing flow rate, which involves also a reduction in efficiency when the machine is operating off its optimized load distribution. Second, the grooves cause generation of a series of secondary flow structures and consequently increase the area with elevated turbulence in the tip region. In particular, a sizable corner vortex, which remains confined to the groove at low flow rates, is entrained by the TLV into the passage as the inflow into the grooves diminishes with increasing flow rate. Close to the best efficiency point, the corner vortex migrates with the TLV and remains noticeable all the way to the trailing edge. In contrast, the endwall boundary layer negative vorticity remains close to the endwall in the untreated passage.

Third, interactions of the TLV with this corner vortex result in a much larger and more broadly distributed TLV circulation, extending it to r^*=0.75 (at s/c=0.66), as opposed to r^*=0.85 for the smooth endwall at the same location (Figs. 5d and h). Clearly, tip leakage effects propagate deeper into the passage in the grooved endwall at high flow rates. While suction of the TLV reduces its signature in the passage at φ=0.25, the opposite effects occur around the best efficiency point, when the radial velocity into the groove diminishes.

Chapter 6 Systematic Evaluations aimed at Optimizing the Geometry of Axial Casing Groove in the NASA Compressor

Performance and flow measurements are carried out to investigate the impact of varying the geometry of axial casing grooves on the stall margin and efficiency of the NASA compressor. Prior studies (Chapter 4 and Chapter 5) have shown that skewed semi-circular grooves installed near the blade LE have multiple effects on the flow structure, including ingestion of the TLV, suppression of BFVs, and periodic variations of flow angle. To determine which of these phenomena is a key contributor, the present study examines the impact of several grooves, all with the same inlet geometry, but with outlets aimed at different directions. The "U" grooves that have circumferential exits aimed against the direction of blade rotation, achieve the highest stall margin improvement of well above 60% but cause a 2.0% efficiency loss near the best efficiency point (BEP). The "S" grooves, which have exits aimed with the blade rotation, achieve a relatively moderate stall margin improvement of 36%, but they do not reduce the BEP efficiency. Other grooves, which are aligned with and against the flow direction at the exit from upstream inlet guide vanes, achieve lower improvements. These trends suggest that causing high periodic variations in flow angle around the blade leading edge is particularly effective in extending the stall margin, but also reduces the peak efficiency. In contrast, maintaining low flow angles near the LE achieves more moderate improvement in stall margin, without the maximum efficiency loss. Hence, of the geometries tested, the S grooves appear to have the best overall impact on the machine performance. Velocity measurements and flow visualizations are performed in an axial plane located downstream of the grooves, near the trailing edge of the rotor. Reduced efficiency

or performance co-occurs with elevated circumferential velocity in the tip region, but differences in the axial blockage are subtle. Yet, near the BEP, the regions with reduced axial velocity, or even negative velocity between the TLV and the endwall, are wider behind the U grooves compared to the S grooves. The vorticity profiles also show that at low flow rates the TLV is ingested entirely by the grooves, in contrast to the best efficiency point, where a considerable fraction of the TLV rollup occurs downstream of the grooves. This work was published in the *Proceedings of ASME Turbo Expo 2019: Turbomachinery Technical Conference and Exposition* (Chen *et al.*, 2019).

6.1 Experimental setup

New casing grooves

Due to cost considerations and the number of grooves involved, the presently used groove-containing rings that surround the leading edge of the rotor are not transparent, preventing us from performing velocity measurements inside the grooves or around the blade leading edge. These rings are made using rapid prototyping. However, we can still perform velocity measurements within the rotor passage downstream of the grooves to determine their impact on the flow structure near the rotor blade trailing edge. Based on the present conclusions, in future work, we plan to manufacture fully accessible grooves for two of the present cases and investigate the flow within and around them in greater detail.

Four of the grooves, the focus of the present Chapter, are illustrated in Figure 6-1. They are labeled as “U”, “S”, “J”, and “ζ” grooves. In all cases, as illustrated for the U groove in Figure 6-1a, the downstream one-third of the groove overlaps with the blade leading edge, and the rest extends upstream and occupies most of the space between the IGV and the rotor. This axial positioning and overlap fraction are consistent with those of the original skewed semi-circular ACG (Figure 4-2). The grooves are evenly spaced circumferentially, and there are four grooves per blade passage, also in agreement with the semi-circular ACG. They have the same inlet

dimensions and shapes, but different outflow orientations. The inlet to each groove has a width of 14.76 mm (8.2 times the tip gap) consisting of a 45° and 9.08 mm deep ramp aligned in the positive circumferential direction. The shape of this ramp has been selected to resemble that of the entrance to the original ACGs. The outlets also have a 45° ramp. The exit from the U groove is aligned in the negative circumferential direction, and consequently, is expected to have a general orientation of the exit flow resembling that of the semi-circular ACG. In contrast, the S groove directs the outflow in the positive circumferential direction. In the J groove, the outflow is directed against the outflow from the inlet guide vane (IGV), and in the ζ groove, the outflow is directed with the outflow from the IGV grooves. All of the grooves are open, i.e., they basically consist of open channels with ramped ends. We have also tested (not shown) "closed" grooves, where only the ramps are open, and the rest of the channel is closed. Additional information, including comments on results obtained for other open grooves, is provided later.

SPIV in axial planes

SPIV measurements (Figure 6-2a) are conducted at two flow rates, $\varphi = 0.25$ and 0.38, for S and U grooves in a axial plane (r, θ) at 86% (Figure 6-2b) of the rotor chord away from the LE (i.e., $s/c = 0.86$, where s is the chordwise coordinate whose origin is at LE.) Since the cross-plane velocity component is dominant, delays between exposures have been set at 60μs for $\varphi = 0.25$ and 40μs for $\varphi = 0.38$, ensuring enough particle displacements in the images (~12-20px) while retaining most of the particles in the laser sheet during two exposures. Shown in Figure 6-2a, the particle images in the 111.3 × 134.8 mm^2 field of view are recorded by two Imperx B6640 CCD cameras (6600×4400 px^2), covering an entire rotor passage from the casing wall to the hub (Figure 6-2b). The resulting vector spacing by using 50% overlap with 24×24 px^2 final interrogation windows is 0.283mm. The ensemble-averaged velocities are presented in a cylindrical coordinate system (r, θ, z) centered at the rotor hub. The corresponding components in the lab reference frame, (U_r, U_θ, U_z), are transformed from the Cartesian components obtained from the SPIV

measurements. The axial vorticity ω_Z is calculated directly from the SPIV results in the Cartesian system since ω_Z is the same in the two coordinate systems.

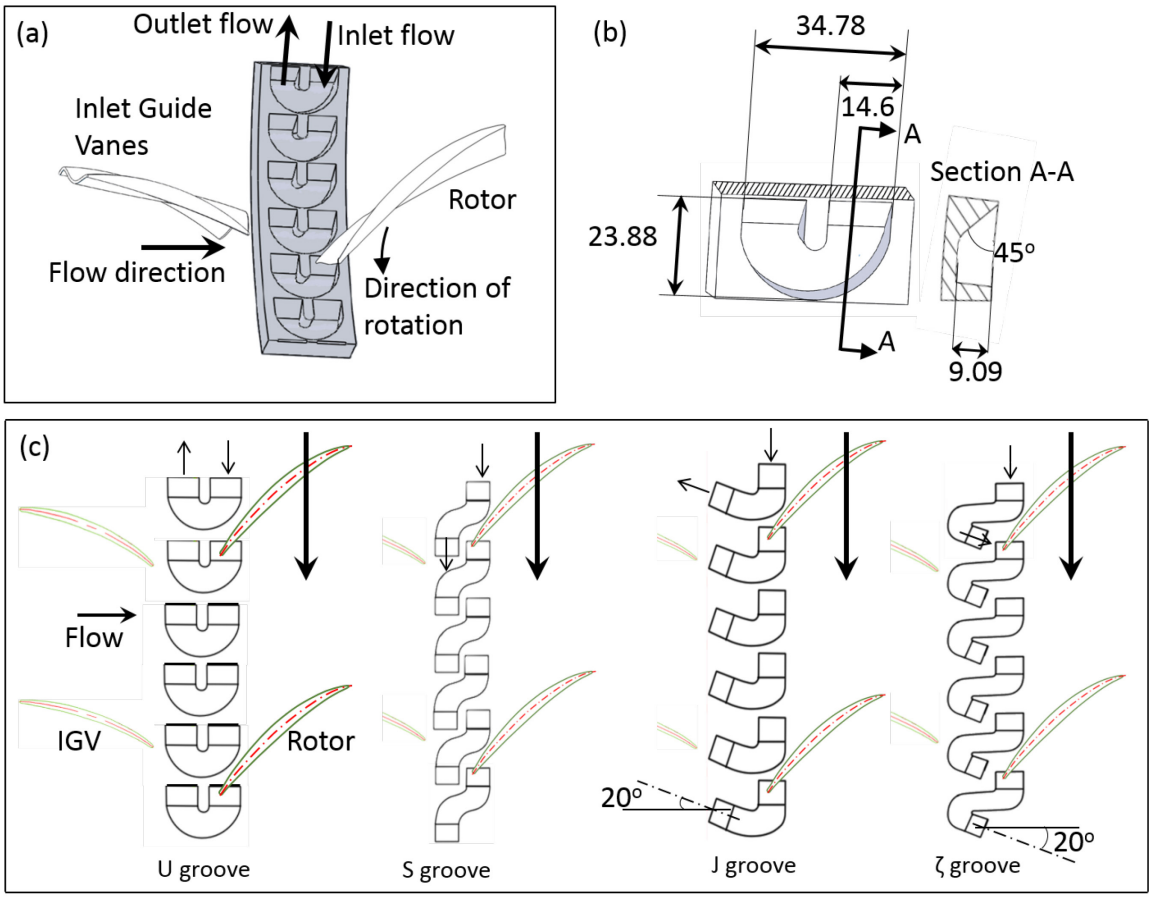

Figure 6-1 The geometry of the present casing grooves. (a) The location and orientation of the U grooves relative to the rotor and IGV blades; (b) Dimensions of the U groove in mm; (c) the shapes and orientation of the grooves.

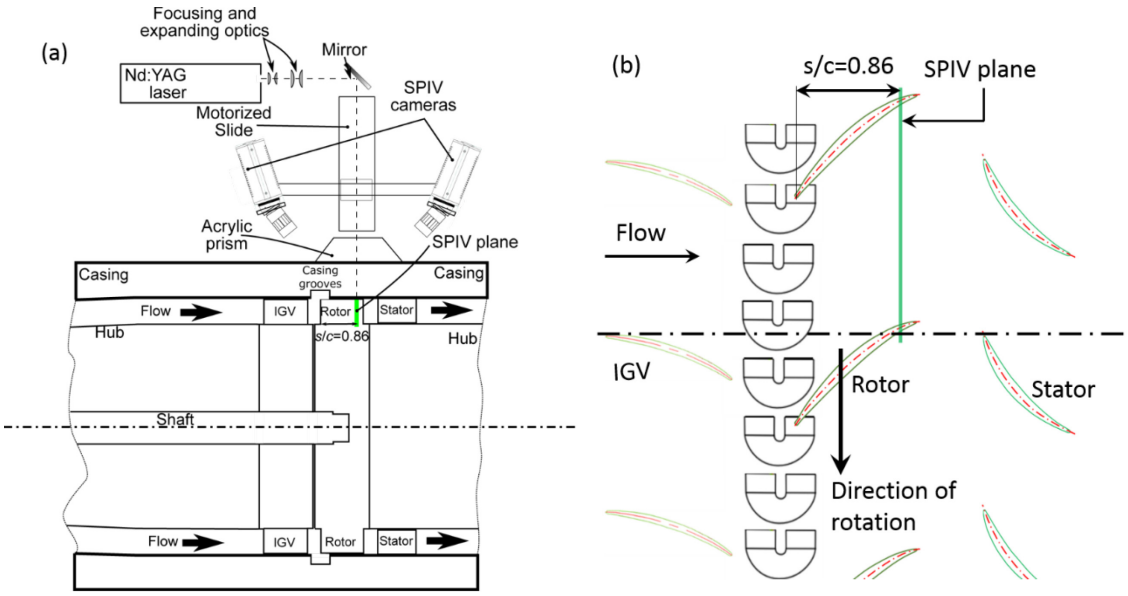

Figure 6-2 Experimental setup for SPIV measurements in an axial (r, θ) plane near the trailing edge of the rotor: (a) side view, and (b) top view.

6.2 Results and discussions

Performance and efficiency curves

Plots of the static-to-static head rise coefficient (ψ_{SS}), are presented in Figure 6-3a&b. The former covers the entire range of flow coefficients expressed as $\varphi=V_Z/U_T$, and the latter focuses on the high flow rate range. The efficiency of the machine (η) for the different casing grooves is presented in Figure 6-3c&d, with the latter again highlighting the high flow rate range. The plots contain results for the original untreated endwall, the semi-circular ACG, as well as for the open U, S, J and ζ grooves. As is evident and discussed before (Chen *et al.*, 2017b, Chapter 2), the stall onset for the smooth endwall occurs at φ=0.25. Installing the original ACG increases the magnitude of ψ_{SS} at φ=0.25, shifts the stall point to φ<0.15. However, as is particularly evident from Figure 6-3b&d, these ACGs cause a reduction in ψ_{SS} at φ>0.36, and a decrease in efficiency at φ>0.35. The peak efficiency decreases by 2.5% and shifts to a lower flow rate.

The U grooves extend the stall margin even further, to φ=0.1, representing a striking 60% improvement compared to the untreated endwall. At φ=0.1, the head coefficient decreases abruptly. On the other side of the performance curve, the values of ψ_{SS} match those of the untreated endwall at φ=0.38, and fall slightly below them at higher flow rates. However, at φ>0.36 the efficiency falls well below that of the smooth endwall, and do not differ significantly from those of the semi-circular grooves. The S grooves extend the stall margin to φ=0.16, representing a substantial 36% improvement, but not to the same extent as the ACGs and the U grooves. The head coefficient matches those associated with the other grooves down to φ=0.25 but then plateaus before decreasing at φ<0.16. At high flow rates (φ>0.37) the magnitudes of ψ_{SS} are marginally higher (within the uncertainty range) than those of the smooth endwall. However, most importantly, the S grooves do not cause an efficiency penalty and maintain the same (even marginally higher) peak efficiency of slightly below 85% at the same flow rate as the untreated endwall. As the error bars in Figure 6-3c indicate, the efficiency penalty caused by the semi-circular ACGs and U grooves at high flow rates, in contrast to the S grooves, which maintain the original efficiency, exceed the uncertainty in the present measurements. Furthermore, to ensure that results are repeatable, two of the tests have been repeated at a different time, and both results, which show consistent trends, are included in Figure 6-3.

As for the ζ grooves, which are aligned with the outflow from the IGV, they have limited effect on the stall margin, reducing the stall flow coefficient only from 0.25 to 0.23. At high flow rates, they maintain high head coefficients matching those of the S groove. The associated efficiencies are only slightly lower than those of the S groove. The J groove, whose exit is aligned in the opposite direction to outflow from the IGV achieve a higher improvement to the stall margin, reducing it from 0.25 to 0.18. However, at high flow rates, the J grooves cause an efficiency loss matching those of the semi-circular ACGs and the U grooves.

In summary, the U grooves achieve the highest stall margin improvements but cause the familiar efficiency loss at high flow rates. In contrast, the S grooves still achieve a substantial stall

margin improvement, but not to the same extent as the U grooves. However, they do not cause an efficiency penalty at high flow rates. Hence, of the geometries tested, the S grooves appear to have the best overall impact on the machine performance. Since both grooves have the same inlet geometry, it appears that the aligning the outflow in the negative circumferential direction achieves better stall margin improvement, presumably owing to the associated larger periodic variations in flow angle near the rotor blade leading edge. Near BEP, these flow angle oscillations appear to contribute to a reduction in machine efficiency. These postulates will be tested in future studies.

Before continuing, as noted before, we have also tested grooves that are not included in Figure 6-3. First, a U groove with a closed channel except for the inlet and exit ramps maintains the same elevated values of ψ_{SS} as the other grooves down to φ=0.25 but then stalls abruptly. Thus, it increases the blade loading up to the pre-stall conditions but does not extend the stall margin. Near BEP, the efficiency falls slightly below that of the untreated wall and is clearly higher than that of the open U grooves. The reasons for the abrupt stall at φ=0.25 in spite having essentially the same head coefficient as the open grooves are not clear at this point. We have also tested open grooves that have exits inclined at 20° to the z-axis in the positive circumferential direction with outlet ramps aligned with and against the flow direction (corresponding to negative and positive circumferential outflow directions). They both extend the stall margin to about φ=0.19, i.e., they are not as effective as the S groove. However, they do not cause an efficiency loss near BEP, and in fact, reach a marginally higher peak efficiency of exceeding 0.85.

Because of the present findings, we have opted to focus our attention on the U and S grooves and study the differences between the flow fields that they generate. In the next section, we use the present non-transparent rings, to examine the flow structure in the rotor passage downstream of the grooves to determine their overall effects on blockage and flow direction. Studies planned for the future will examine the detailed flow structure within and around the grooves using transparent U and S grooves.

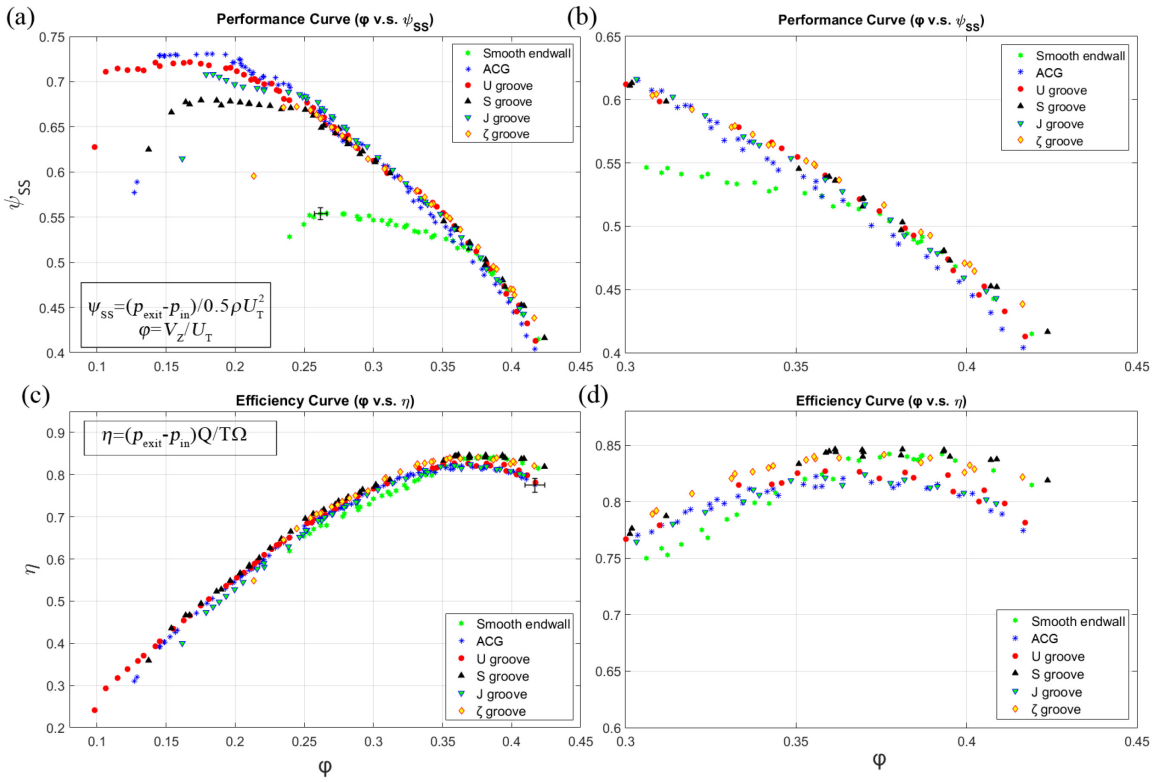

Figure 6-3 Comparisons of performance and efficiency curves for the different grooves to those of the smooth endwall: (a&b) static head rise, and (c&d) efficiency. (a&c) cover the entire flow rate range, and (b&d) focus on the vicinity of the BEP.

Flow structure downstream of the grooves

Figure 6-7 shows the distributions of axial velocity scaled with V_Z covering an entire rotor passage for the U grooves (left column) and S grooves (right column). The top row shows the results for φ=0.25 (pre-stall for untreated groove), and the bottom row for φ=0.38 (BEP for untreated groove). The dashed lines show the location of U_Z/V_Z=1.0, red for the S grooves and black for the U grooves, above which the axial velocity falls below the mean values due to effects of tip blockage. The solid lines show the location of U_Z/V_Z=0.0, above which the axial velocity is negative, with the same color codes. Several trends are evident. First, at φ=0.25, the differences between velocity contour maps are small, but the U grooves create a wider region with negative U near the endwall casing. At φ=0.38, the U_Z/V_Z<1.0 and U_Z/V_Z<0 are noticeably wider for the U

grooves, consistent with the corresponding reduced BEP efficiency. However, even in this case, the overall velocity distributions are not strikingly different.

Larger discrepancies occur in the distributions of U_θ/V_Z presented in Figure 6-5. To accommodate comparisons to Figure 6-4, each of the plots contains the lines indicating the locations of U_Z/V_Z=1.0 and 0.0. In all cases, the tip regions with $0<U_Z/V_Z<1.0$ are also characterized by high U_θ. At φ=0.25, U_θ for the S groove is higher than that of the U groove, and conversely, at φ=0.38, U_θ for the U groove is higher than that of the S groove. These trends suggest that reduced performance is associated with increased values of U_θ in the tip region. Interestingly, Houghton and Day (Houghton *et al.*, 2011) also observe an increase in U_θ and a minimal difference in axial velocity for circumferential grooves installed at mid-passage, which causes a higher efficiency penalty. They attribute the reduced efficiency to the elevated circumferential flow. In all cases, the U_Z/V_Z=1.0 line is located in a region with radial gradients in U_θ. Accordingly, the corresponding distributions of mean streamwise vorticity, presented in Figure 6-6, show that for the most part peaks with positive values along or just above this line. A second thinner positive vorticity layer appears to form near the SS of the blade and seems to be connected to the SS below the tip corner. A third negative layer is evident primarily at φ=0.38 near the endwall close to the PS, just inboard of the U_Z/V_Z=0.0 line. At mid-passage, where this negative layer is located between the positive ones, it appears to have a kink. At φ=0.25, the negative layer is much thinner and remains confined very close to the endwall.

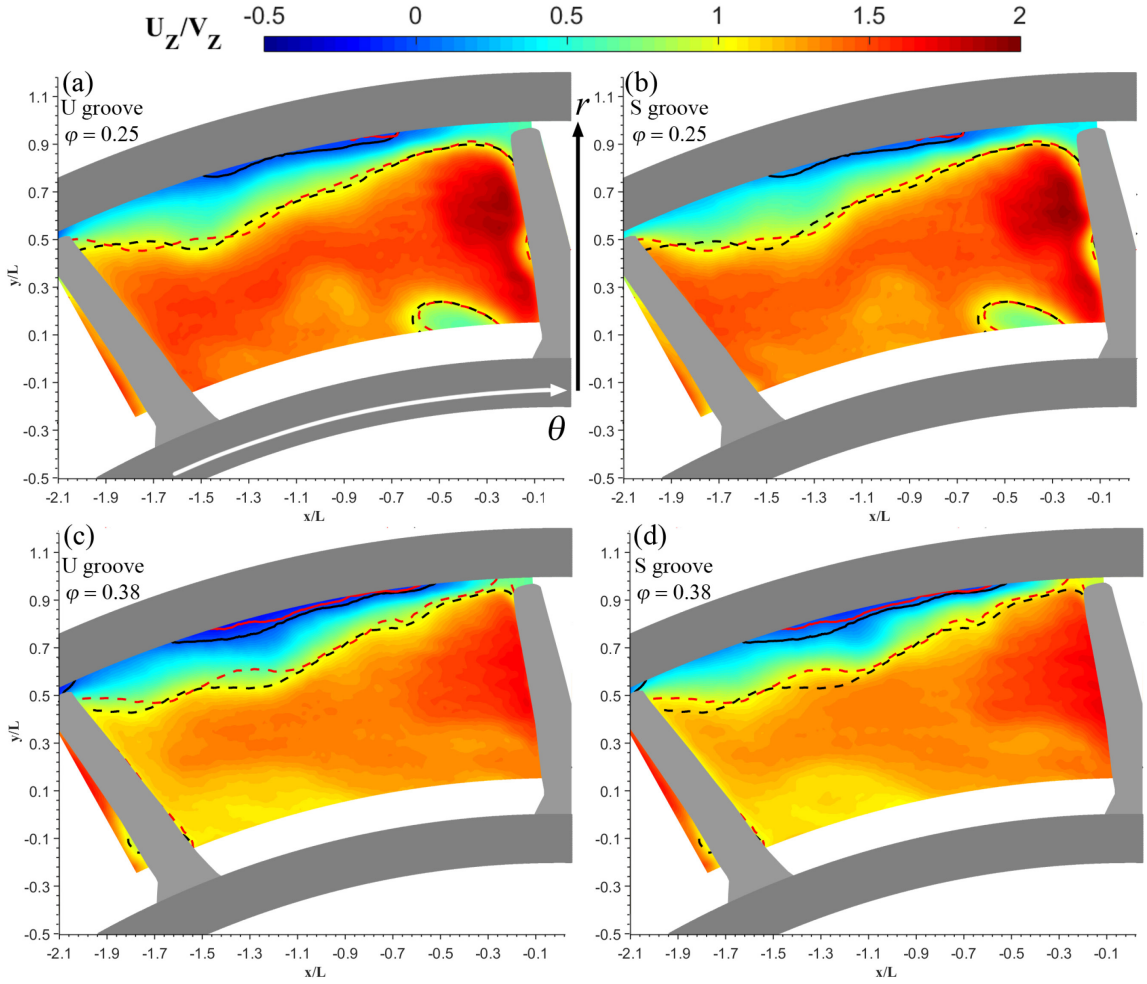

Figure 6-4 Distributions of axial velocity (U_Z/V_Z) in the (r, θ) plane located at s/c = 0.86. (a&b) φ=0.25; (c&d) φ=0.38. Left column (a&c) U groove; and right column (b&d) S groove; Dashed lines: U_Z/V_Z=1; solid lines: U_Z/V_Z =0. Black lines correspond to the U groove and red lines to the S groove.

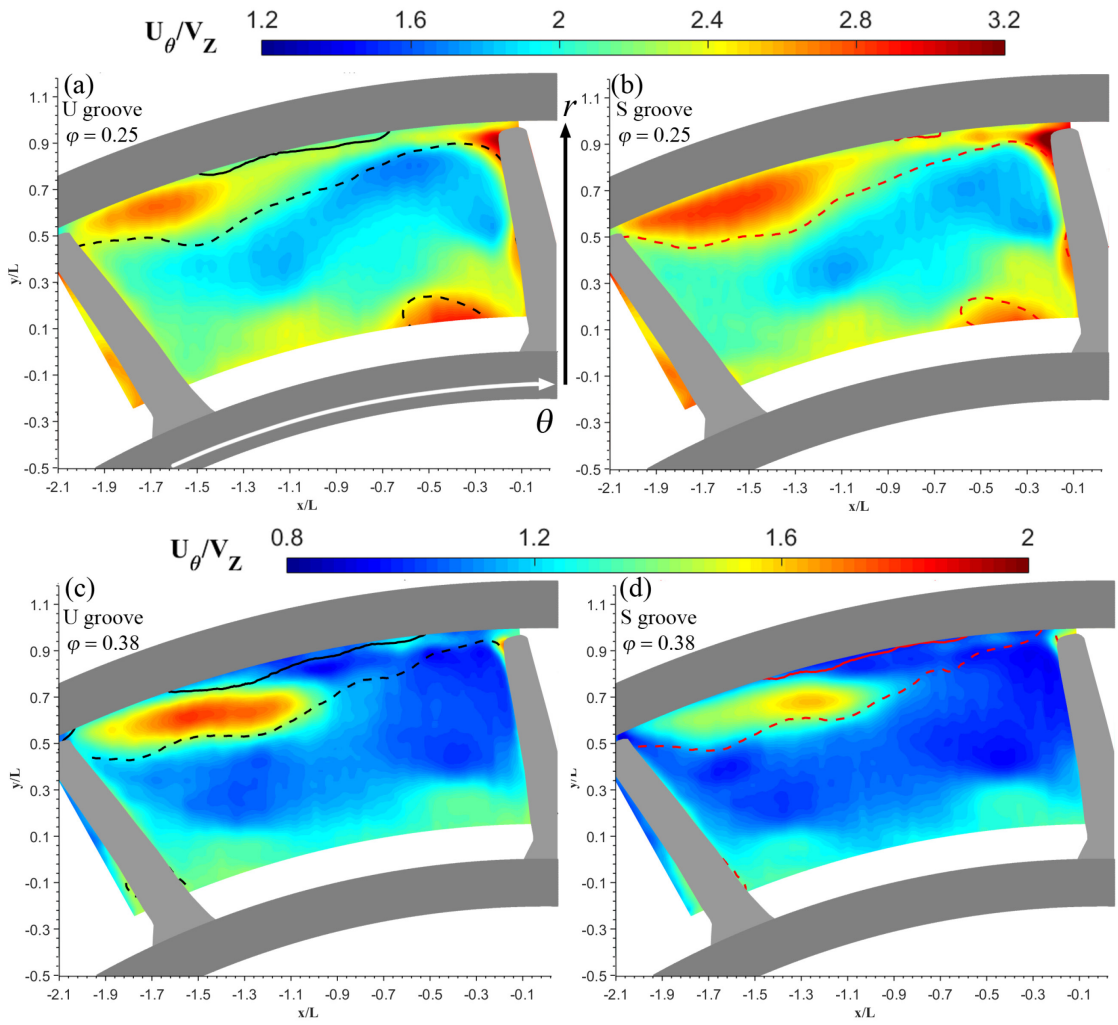

Figure 6-5 Distributions of circumferential velocity (U_θ/V_Z). For line definitions, see Figure 6-4.

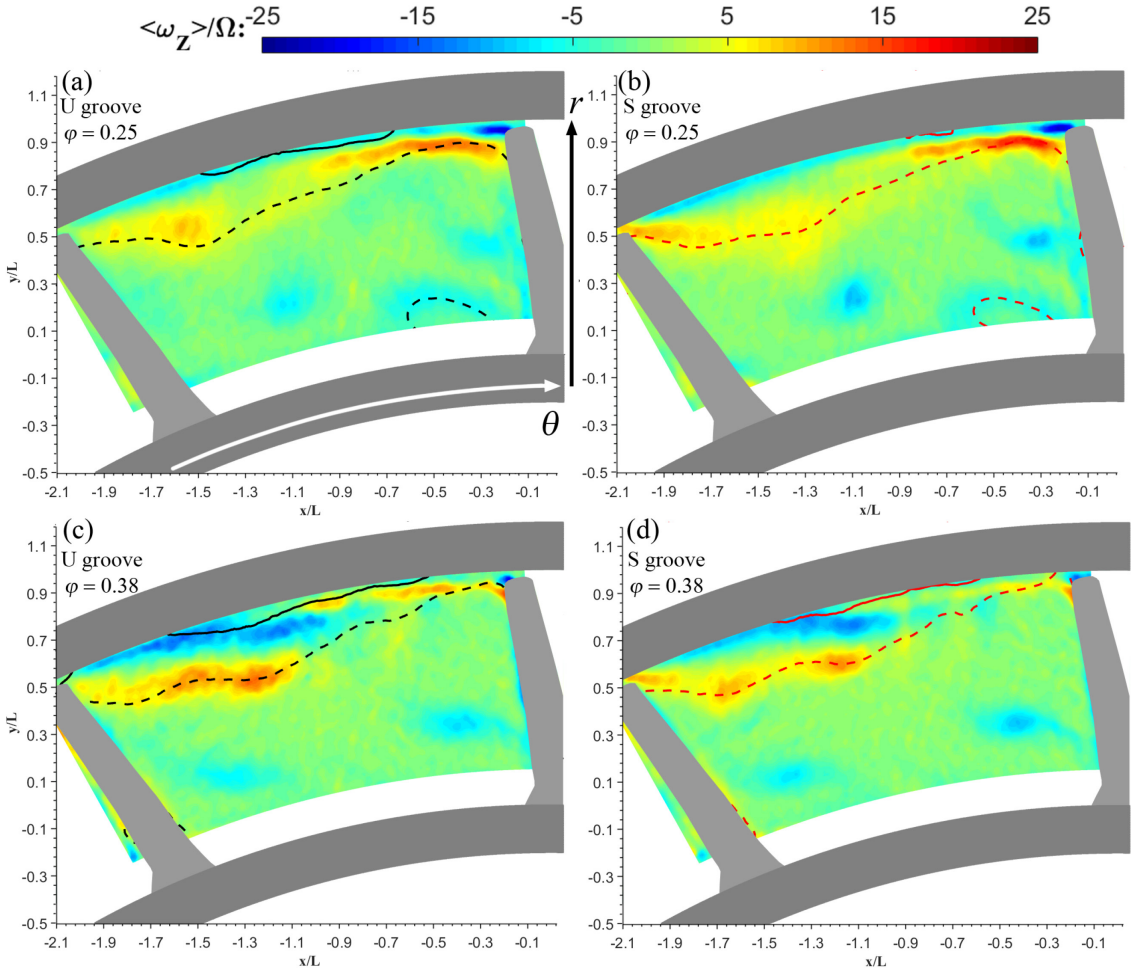

Figure 6-6 Distributions of axial vorticity ($<\omega_Z>/\Omega$). Lines are defined in Figure 6-4.

In an attempt to understand the origin of the vorticity layers, Figure 6-7 shows two sample cavitation images for an S groove at φ=0.35, which visualize the location of low-pressure regions, such as vortices. As discussed in previous publications (Tan *et al.*, 2015b), the cavitation is initiated after reducing the mean pressure in the facility. All the performance curves and velocity measurements are performed at higher pressures, without any cavitation. As is evident, in both cases, the main TLV is only slightly inclined to the circumferential direction, implying that its signature in the present PIV plane should appear as a broad low negative vorticity layer, mostly closer to the PS of the blade. Velocity induced by this vortex above its center, i.e., near the endwall,

is expected to be in the negative axial direction. These observations explain the presence of the $<\omega_Z>$ <0 layer and the region U_Z/V_Z <0 above it. The positive inner layer is associated with the backflow vortices (Chen *et al.*, 2017b, Chapter 2), which, as discussed in the introduction, formed at the interface between the region influenced by the tip leakage flow where U_θ is elevated, and the main passage flow inboard from it. The presence of these BFVs, which have a positive axial component, is evident from the cavitation images. For an untreated endwall, they are a primary contributor to the onset of rotating stall (Chen *et al.*, 2017b, Chapter 2). Finally, the outer/narrower $<\omega_Z>$ >0 layer develops along the inboard side of the tip leakage flow emerging from the tip gap carrying a series of vortex filaments, which are also evident from Figure 6-7. The consistent presence of multiple layers with the same signs, confirming the present claims, is also demonstrated based on higher resolution measurements performed in the untreated machine (Chen *et al.*, 2017b, Chapter 2).

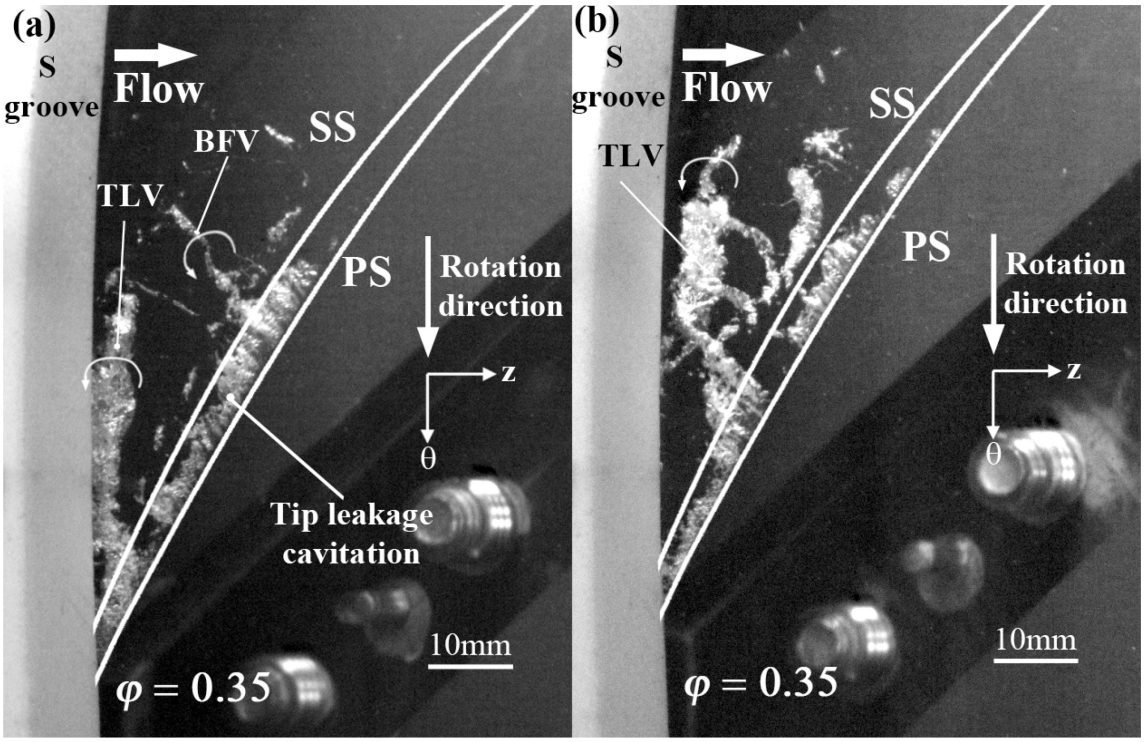

Figure 6-7 Sample cavitation images visualizing vortical structures in the tip region downstream of the S groove at φ = 0.35.

In contrast, except for limited tip leakage cavitation just downstream of the ring, the cavitation image recorded at φ=0.25 with the S grooves do not show persistent, organized large-scale structures developing downstream of the grooves. Hence, they are not presented. This observation indicates that at this flow rate, most of the TLV is ingested and scrambled by the grooves, in complete agreement with the observations and measurements performed using the transparent ACGs (Chen *et al.*, 2017a, Chapter 4). Hence, the corresponding axial vorticity distributions (Figure 6-6) do not have a distinct negative vorticity layer propagating to the pressure side of the passage. The only place where the TLV has any noticeable effect is very close to the blade tip. As the flow rate increases and blade loading shifts downstream, a larger fraction of the vortex shedding and TLV rollup occurs downstream of the grooves, resulting in the patterns observed close to BEP. In summary, all the flow phenomena occurring in the tip region, including the elevated U_θ regions high are associated with tip leakage flows and their propagation away from the blade. Increased U_θ appears to correlate with reduced performance or efficiency. In addition, the U grooves generate a slightly wider region with reduced axial velocity, i.e., blockage, than the S grooves close to the best efficiency point.

6.4 Summary

Prior velocity measurements and flow visualizations performed in the JHU refractive index matched facility have shown that axial casing grooves aimed at extending the stall margin have multiple effects on the flow structure. They ingest and scramble the TLV, prevent the formation of BFVs, which play a prominent role in the propagation of rotating stall, and cause substantial periodic variations in the flow angle around the rotor blade leading edge. To determine which of the co-occurring flow phenomenon is a key contributor to the suppression of stall, the present Chapter examines the impact of series of grooves, all with the same inlet (downstream end) geometry, but with outlets are aimed at different directions. Hence, the periodic suction of the

TLV is expected to occur in all of them, but they would cause different periodic variations in flow angle near the blade LE.

The U grooves that have exits aimed in the negative circumferential direction (against the blade rotation), similar to the original skewed semi-circular grooves, achieve the highest stall margin improvement of well above 60% but cause a 2.0% efficiency loss at near the best efficiency point. The S grooves, which have exits aimed at the positive circumferential direction, still achieve a substantial stall margin improvement of 36%, but not to the same extent as the U grooves. However, they do not reduce the efficiency at high flow rates compared to the untreated endwall. Several other grooves, which are aligned with and against the flow direction at the exit from the IGV, achieve lower stall margin improvements. These trends suggest that causing high periodic variations in flow angle around the blade leading edge, achieved by aiming the outflow from the groove against the direction of blade rotation, and achieves the highest stall margin improvement. However, this approach also involves a penalty of reduced maximum efficiency. In contrast, aiming the outflow with the blade rotation, which reduces the flow angle near the LE, appears to achieve a more moderate but still substantial improvement in stall margin, without the efficiency loss at a high flow rate. Hence, of the geometries tested, the S grooves appear to have the best overall impact on the machine performance.

Due to the number of grooves involved, they have been manufactured of non-transparent materials using rapid prototyping. Hence, velocity measurements and flow visualizations have been limited to axial planes located downstream of the grooves, near the trailing edge of the rotor. The velocity measurements, which cover almost an entire blade passage, compare the flow structure downstream of the U and S grooves. In agreement with previously observed trends for circumferential grooves, reduced efficiency or performance co-occur with elevated circumferential velocity in the tip region. Blockage effects in the tip region occur downstream of both grooves, and the differences between them are subtle. Yet, near the best efficiency point, the regions with a negative axial velocity above the TLV, and where the axial velocity is lower than

the spatially averaged value, are a little wider behind the U grooves. The vorticity profiles also suggest that at low flow rates the TLV is ingested almost entirely by the grooves, in contrast to the vicinity of the best efficiency point, where a considerable fraction of the TLV rollup occurs downstream of the grooves. To explain the present findings, the next series of experiments will focus on measuring and comparing the details of blade-groove interactions for the U and S grooves at varying flow rates using transparent, fully accessible flow near the blade leading edge.

Chapter 7 Measurements of Flow and Pressure within the AxWJ-2 Waterjet Pump during Cavitation Breakdown

The flow mechanisms causing cavitation breakdown in axial turbomachines have been a long-standing puzzle. Recently, observations in our laboratory have associated this phenomenon with blockage caused by perpendicular cavitating vortices (PCVs) in the blade tip region (Tan *et al.*, 2015c). In follow-up experiments, circumferential casing grooves (CGs) have been used to manipulate the tip leakage flow, intending to suppress the formation of PVCs. While the PCV formation is affected by a CG located near the trailing edge, it shows very little effect in alleviating the rapid performance deterioration during the breakdown. High-speed movies show that breakdown begins when a slight decrease in inlet pressure extends the attached/sheet cavitation on the blade SS into the blade overlap region. At this phase, the area covered by the sheet cavitation initially fluctuates and then expands rapidly to cover a large portion of the surface. SPIV measurements performed in non-cavitating fractions of the passage show that this process involves a significant increase in liquid velocity and a decrease in pressure along the blade PS in the overlap region. It appears that blockage caused by the cavitation on the SS accelerates the flow along the PS, which results in further reduction in pressure over the entire passage and further expansion of the cavitation on the SS. However, the pressure difference across the blade tip measured at mid-span increases, compensating for the reduction in PS pressure. Hence, in some cases, the pump head increases slightly at the onset of breakdown. Further reduction in inlet pressure causes an increase in blockage in the tip region, but still a slight increase in velocity deeper in the passage. The reduced flow rate combined with a decrease in mid-passage pressure results in a rapid drop in the head as well. The CG is only partially effective in reducing the tip region blockage,

presumed due to the inability of the shallow grooves to affect the cloud cavitation that fills the trailing edge tip region at this stage. This work was presented at *31st ONR Symposium on Naval Hydrodynamics* (Chen *et al.*, 2016) and *2017 International Symposium on Transport Phenomena and Dynamics of Rotating Machinery* (Chen *et al.*, 2017a).

7.1 Experimental setup

Circumferential casing grooves at varying locations are created by installing a combination of 6.35mm thick transparent acrylic inserts in slots surrounding the rotor, as illustrated in Figure 7-1a. As shown in Figure 7-1b, three CG configurations have been tested, with CG1 centered at the blade leading edge, CG2 located near the mid-chord, and CG3 covering the trailing edge. All grooves have the same width of 30.4mm (0.11*c*) and depth of 6.35mm (0.04*R*). High-speed images of cavitation are recorded by a PCO. dimax high-speed camera at 1800 frames per second, corresponding to 20 frames per blade passing when the rotor is operating at a constant speed of 900 RPM.

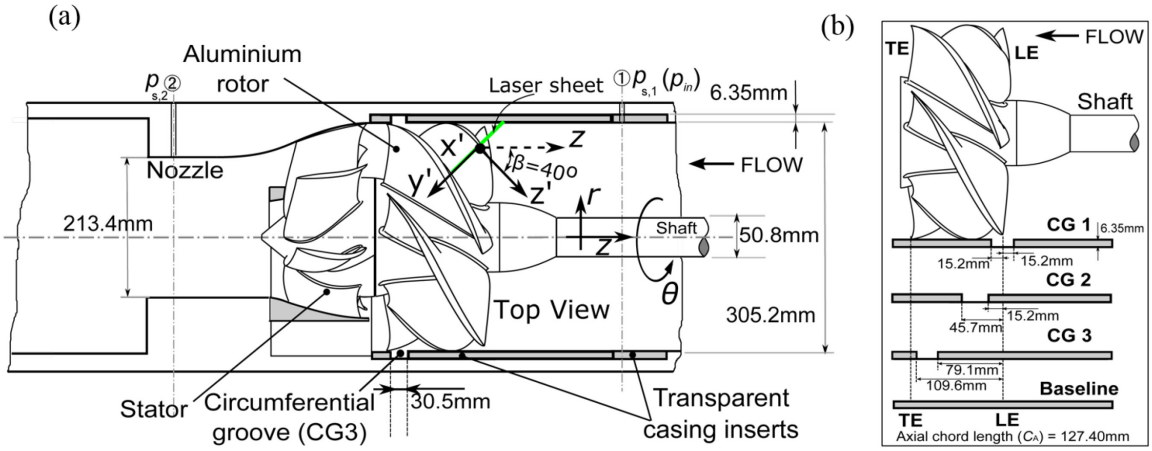

Figure 7-1 (a) The AxWJ-2 with casing groove (CG3) installed and the imaging setup for SPIV measurement. (b) The circumferential groove configurations.

The setup for SPIV measurement is shown in Figure 7-1 and Figure 7-2. The images are recorded by a pair of 2048×2048 pixel PCO. 2000 cameras located on either sides of the laser

sheet. Optical distortions are minimized by viewing the sample area through prisms with the outer surface aligned perpendicularly to the lens axis. To characterize the effect of cavitation on the pump performance, the SPIV measurements focus on the flow along PS deep inside the blade and the non-cavitating parts of the tip region. The laser sheet is orientated to minimize the detrimental effects of light scattered by the cavitation. It is also almost perpendicular to the SS surface at the entrance to the blade overlap region. To define the orientation and location of this sheet, we use a general coordinate system (r, θ, z) that has an origin located at the pump center, and coincides with the plane of the leading edge of the blade. The coordinate system associated with the sample plane is (x', y', z'), where x' and y' are located within the illuminated area, and z' is inclined by β=40° to the z direction (Figure 7-1a and Figure 7-2c). As illustrated in Figure 7-2c&d, the origin of (x', y', z') is located at r/R=0.995, θ_{PIV}=−37.5° (θ=0 is the vertical direction), and z=0. Figure 7-2a&b, which look at the sample area from the back, show that in this arrangement, the intersection of the bottom of the laser sample area with the blade PS is located more downstream of the LE than the top part. By maintaining the laser sheet in the same location, but recording data for different blade orientations, we can obtain data in different planes relative to the blade leading edge. The measurements have been performed in 4 planes. For each one, 200 images pairs have been recorded at a series of cavitation indices.

The sample area size is 75.3×114.8 mm^2, and the vector spacing is 0.41 mm for 24×24 pixels^2 interrogation windows with 50% overlap. Due to obstruction by the TLV cavitation, only part of the PIV image is available, but it still allows us to examine the flow and pressure distributions along the pressure side of the blade, from the casing, r/R=1.0, down to r/R=0.66, which represents 50% of the rotor blade span. As shown in Figure 7-2b, the "triangular" field of view (FOV) is bounded by the blade PS to the left and the casing wall on the top. The SPIV measurements have been performed on the baseline case without grooves and CG3 case, with the groove located near the blade trailing edge.

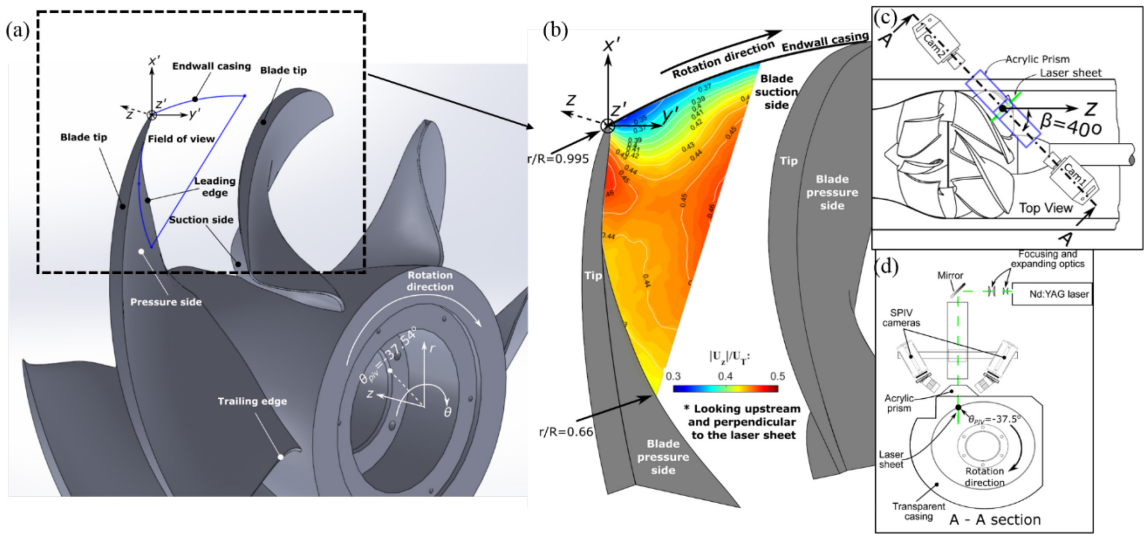

Figure 7-2 (a) A perspective view of the laser sheet coincides with the LE tip. (b) A magnified view of the SPIV plane with a sample $|U_z|$ distribution. (c & d) Top and section views of the SPIV setup.

All the velocity components have been transformed from the laser sheet coordinate system (u, v, w) into the global cylindrical system (u_r, u_θ, u_z), with the corresponding ensemble averages components denoted as (U_r, U_θ, U_z). The coordinates and vectors transformations are as follows:

$$r = \sqrt{(x' + R_r \cos\theta_{PIV})^2 + (y'\cos\beta + z'\sin\beta - R_r \sin\theta_{PIV})^2} \tag{7.1}$$

$$\theta = \tan^{-1}\frac{y'\cos\beta + z'\sin\beta - R_r \sin\theta_{PIV}}{x' + R_r \cos\theta_{PIV}} \tag{7.2}$$

$$z = -y'\sin\beta + z'\cos\beta \tag{7.3}$$

$$u_r = u\cos\theta + (v\cos\beta + w\sin\beta)\sin\theta \tag{7.4}$$

$$u_\theta = -u\sin\theta + (v\cos\beta + w\sin\beta)\cos\theta \tag{7.5}$$

$$u_z = -v\sin\beta + w\cos\beta \tag{7.6}$$

A sample distribution of axial velocity magnitude ($|U_z|/U_T$) prior to cavitation breakdown is presented in Figure 7-2b. It shows the axial velocity deficit near the tip occurring due to

combined effects of the casing boundary layer, TLV cavitation induced blockage, and proximity to the blade leading edge, as well as the increase in velocity with increasing distance from the PS. In this case, the sample plane coincides with the leading edge of the blade tip. However, most of the data presented in this Chapter corresponds to a plane that intersects with the blade tip at s/c=0.065, i.e. inside the passage. Here, s is the distance from the leading edge along the blade tip chord.

7.2 Results and discussion

Pump performance

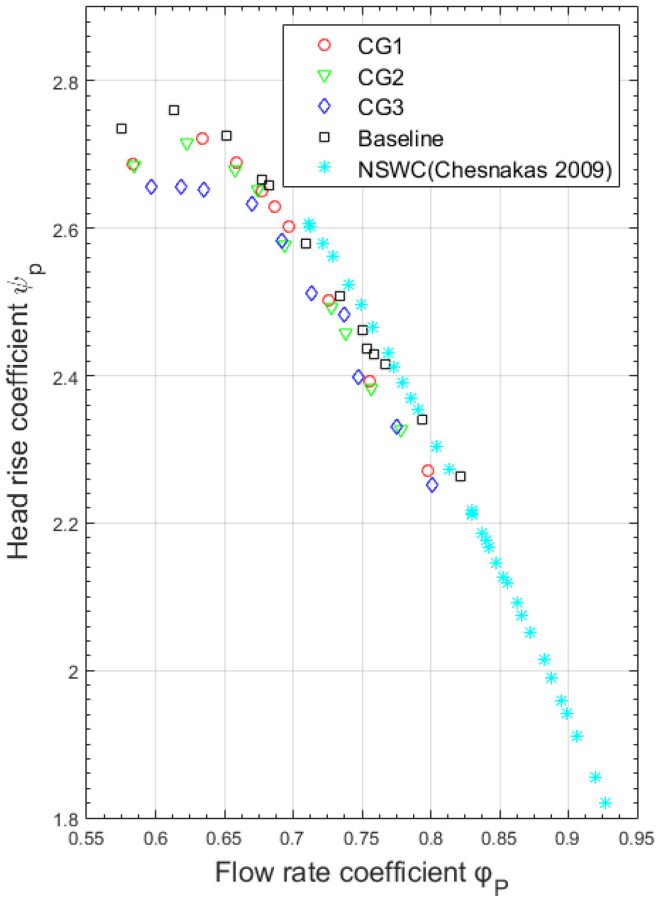

Figure 7-3 Pump performance curves for the baseline and CGs

Figure 7-3 shows the flow rate-head curves for all the tested cases. The test results conducted in NSWC (Chesnakas *et al.*, 2009) using the same rotor are also included for comparison. Based on NSWC results, the pump efficiency peaks at 89% at φ_p=0.76. The definitions for φ_p and ψ_p are introduced in Chapter 2.

The absolute static pressure at the entrance to the pump ($p_{s,1}$ at z/R=1.16) is measured by a manometer and used for calculating the cavitation index

$$\sigma = \frac{p_{s,1} - p_v}{0.5\rho U_T^2} \tag{7.7}$$

where p_v is the vapor pressure of the liquid.

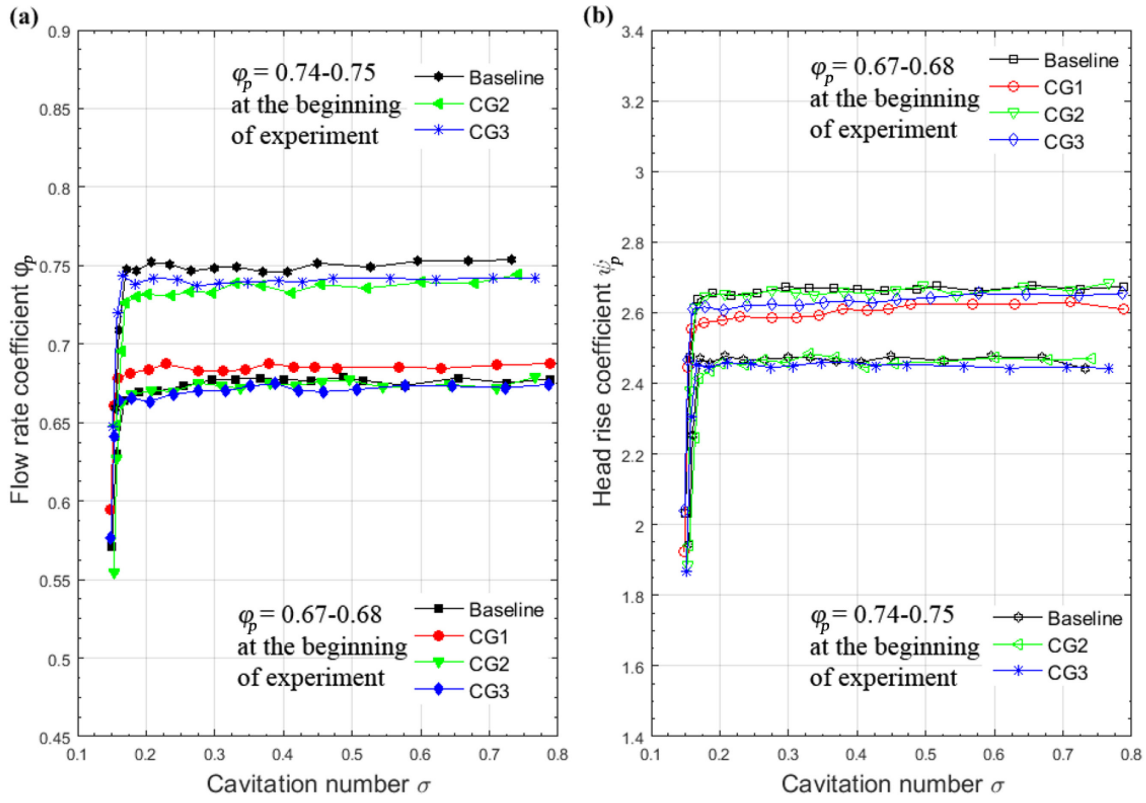

Figure 7-4 Cavitation breakdown curves: (a) Flow rate coefficient, and (b) total head coefficient.

As shown in Figure 7-3, for φ_p=0.65-0.8, the casing grooves cause a 1%-2% reduction in total head rise compared to the baseline values. The untreated performance curve peaks at φ=0.61, suggesting that stall might occur under this condition. The present CGs do not seem to delay the

onset of stall, and in fact, cause a maximum of about 4% decrease in performance at low flow rates. While other studies have shown that circumferential grooves cause a delay in the onset of stall (Fujita *et al.*, 1984; Takata *et al.*, 1977), the present CGs do not, presumably due to their shallow depths.

To test the effectiveness of the CGs on delaying cavitation breakdown, the mean pressure in the facility is gradually reduced, and the pump performance is measured after running the machine at the same condition for more than 40s. The results are summarized in Figure 7-4. The tests are carried out at two different initial flow rates, one starting from φ_p=0.74-0.75 while the other one starting from φ_p=0.67-0.68. For all the cases and flow rates, the total head drops abruptly at around σ=0.17, indicating that the CGs do not change the breakdown cavitation index noticeably. Furthermore, the breakdown cavitation index is not affected by the flow rate, hence the blade load distribution. Tests performed by Kang *et al.* (2010) for an inducer with CG at the LE have shown similar trends. In their study, although the primary goal of using the CGs to suppress the instabilities caused by cavitation is achieved, the grooves do not appear to have a significant impact on delaying the cavitation breakdown.

Appearance of cavitation

Detailed descriptions of the appearance of cavitation for the different CG cases are provided in Chen *et al.* (2016), and only samples for CG3 are discussed in detail in this Chapter. Figure 7-5 compares the CG1 and baseline cavitation phenomena at two different cavitation indices. At relatively high pressures (σ>0.3), CG1 clearly entrains the TLV and aligns it parallel to the groove downstream side (Figure 7-5a). Although the shedding of cloud cavitation on the SS persists, it is clearly decoupled from the TLV, and formation of a PCV is prevented. However, with decreasing pressure to σ<0.3, even before breakdown (Figure 7-5c), significant parts of the triangular cavitating area and TLV appear downstream of the groove. Furthermore, PCVs develop, in a location that is very similar to that of the baseline case (Figure 7-5d). At this pressure,

interactions of the TLV with the attached cavitation still occurs upstream of the overlap region. With further reduction in pressure (not shown), the differences in the appearance of tip region cavitation become harder to notice, although some of the TLV remains trapped within the groove. Hence, it appears that CG1 does not have sufficient impact on the cavitation in the (overlap) region, where it seems to matter. Similar phenomenon happens for CG2 as well. In conclusion, at high cavitation indices, well above breakdown, CG1&2 trap the TLV, altering its interactions with the cloud cavitation. However, upon further reduction in inlet pressure, but still before breakdown, part of the TLV "escapes" from the grooves, resulting in tip region cavitation phenomena that are similar to those associated with the baseline case.

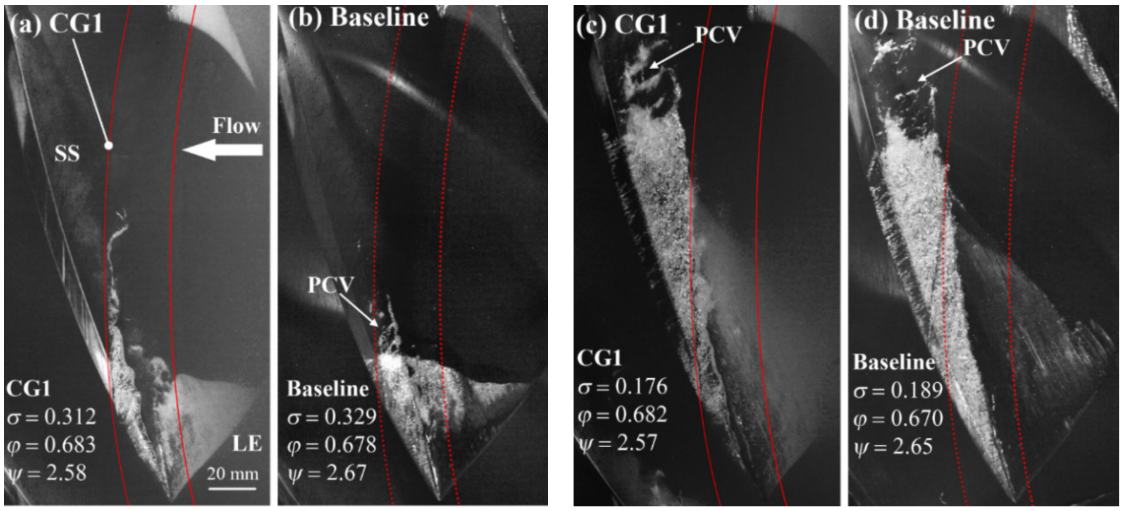

Figure 7-5 (a) A sample image demonstrating the entrainment of the TLV by CG1 at σ=0.312, prior to breakdown, and (b) a baseline sample at similar conditions. (c) Part of the vortex escapes from CG1 with decreasing σ, and (d) a baseline case under similar conditions. Solid red lines indicate the boundaries of CG1, and dashed lines show the same location, but without grooves.

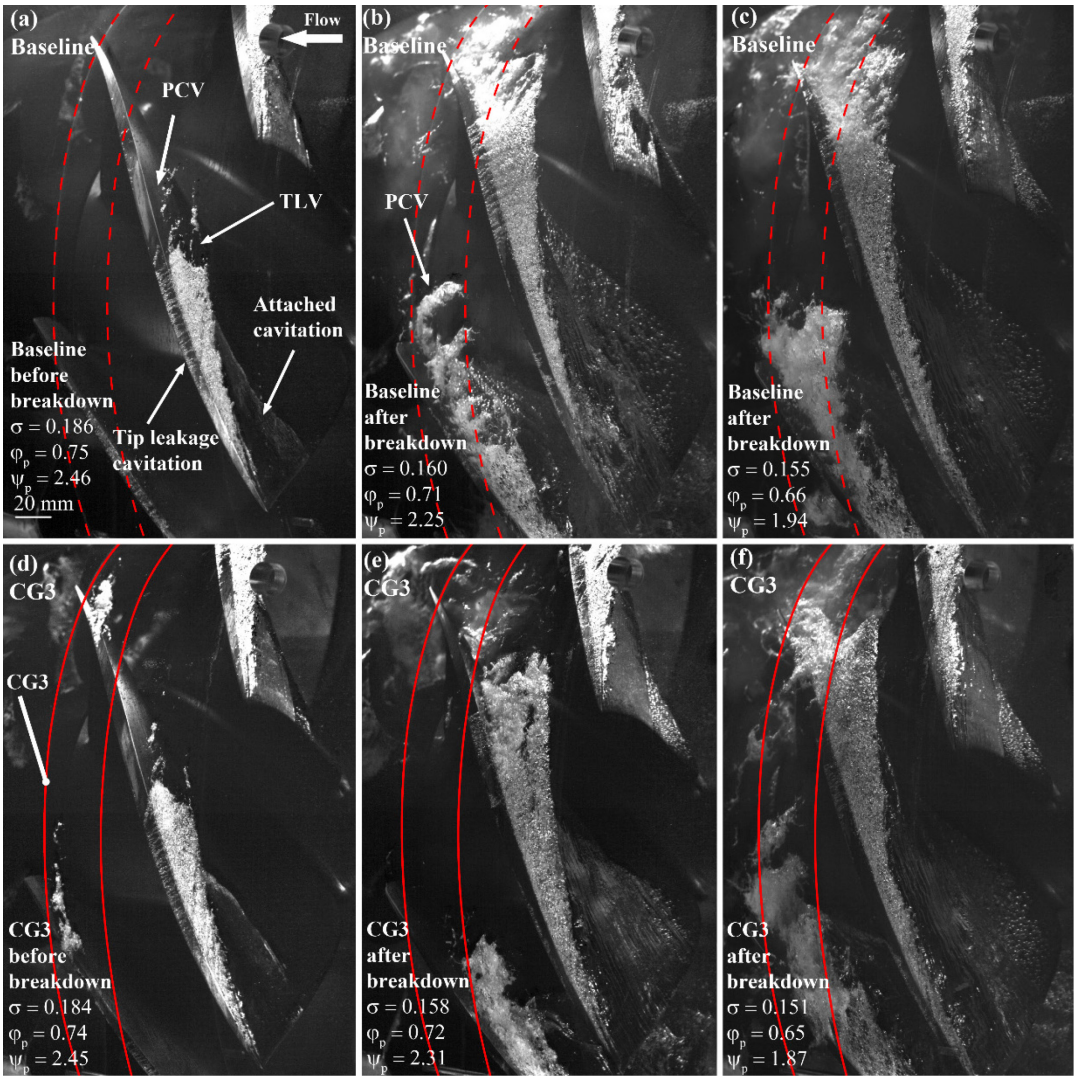

Figure 7-6 Comparisons of cavitation phenomena at three different cavitation numbers before (a & d) and after (b-c & e-f) cavitation breakdown for the baseline case (top row) and the CG3 case (bottom row). Solid red lines in (d-f) indicate the boundaries of CG3 and the dashed lines in (a-c) show the same location but without a groove.

Figure 7-6 compares the evolution of cavitation for the baseline and CG3 cases with decreasing σ. The cavitation indices are chosen to represent the flow conditions that are just before and after cavitation breakdown. Before breakdown (Figure 7-6a&d), the extent of TLV cavitation and the area covered by attached cavitation on the blade SS for the baseline and CG3 appear to be similar. In both cases, entrainment and re-orientation of the cloud cavitation by the TLV generate

the small-scale PCVs indicated on the figure. Under this condition, the attached cavitation has not yet propagated into the blade overlap region. The only effect of CG3 is the formation of an additional cavitating vortical structure inside the groove, close to the trailing edge. Similar phenomena have been observed for the other grooves but at different locations. In contrast, once breakdown occurs, a substantial fraction of the blade SS within the overlap region is covered by cavitation (Figure 7-6b, c, e&f). A sample time sequence demonstrating the transition between these states is presented for the baseline case in Figure 7-7. Here, the cavitation index (σ=0.171) is only slightly lower than that of Figure 7-6a (σ=0.186), corresponding to an absolute pressure difference of 2.8 kPa. The attached cavitation propagates into the blade overlap region and the fraction of SS area covered by it oscillates at high amplitude. All the images in Figure 7-7 correspond to the same mean flow condition, but while a small area is covered by cavitation at $t=t_0$ and $t=t_0+3\Delta t$ (Figure 7-7a&d), most of the lower blade is covered at $t=t_0+\Delta t$ and $t_0+2\Delta t$ (Figure 7-7b & c). It should be noted that at this condition, which is referred to in the rest of this Chapter as "breakdown onset," the flow rate still has not changed, and the head rise increases slightly.

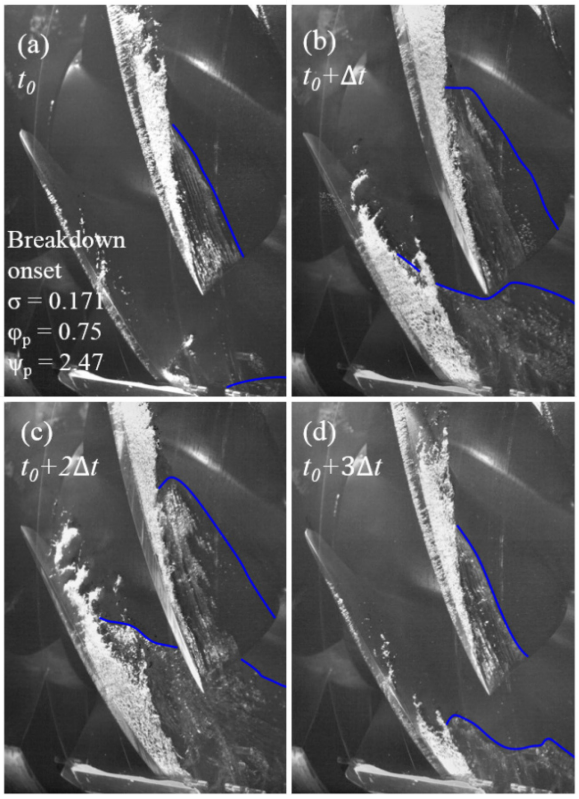

Figure 7-7 Rapid oscillations of attached cavitation at breakdown onset for the baseline

A further slight reduction of the inlet pressure of the baseline rotor to σ=0.160, a change of 2 kPa, already causes a significant reduction (8.5%) in the head rise. The attached cavitation stabilizes in the overlap region, and distinct PCVs form near the blade trailing edge (Figure 7-6b). While the expansion of the attached cavitation into the overlap region occurs for the CG3 case as well, its chordwise extent is lower than that in the baseline case, and the formation of PCVs near the blade trailing edge is suppressed (Figure 7-6e). Yet, the performance barely improves, as evidenced by the slightly higher head rise occurring at a lower cavitation index (σ=0.158) in Figure 7-6e. This observation challenges the claim that the PCVs play primary roles in the cavitation breakdown, as proposed by Tan *et al.* (2015c). Further minor reduction in cavitation index causes substantial deterioration of both the flow and head coefficients for both the baseline and CG3 cases (Figure 7-6c&f). Here, the PCVs form for the CG3 case as well, demonstrating that this groove is not effective in suppressing them.

Velocity and pressure distributions

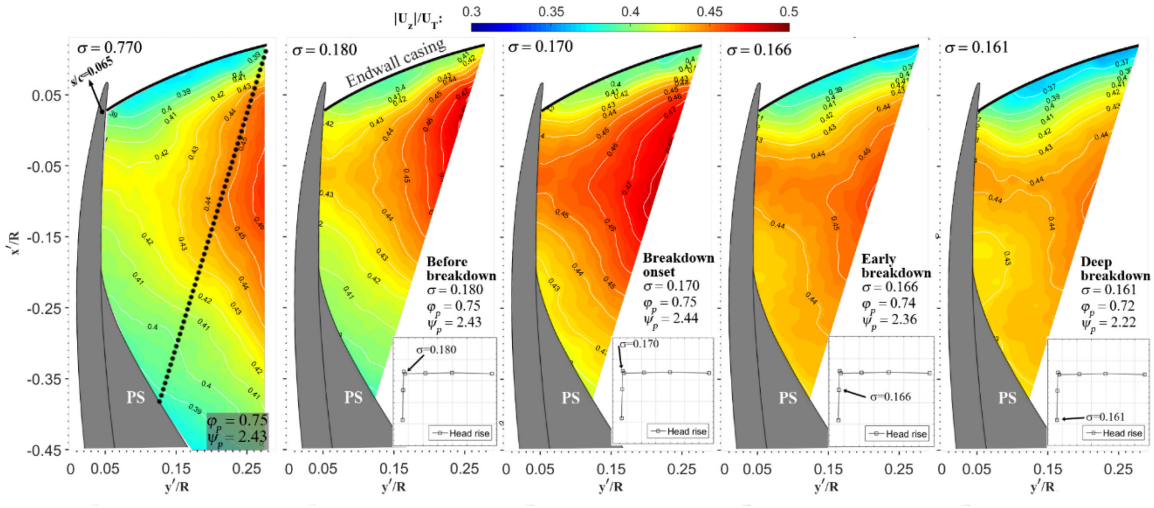

Figure 7-8 Evolution of $|U_z|$ for the baseline case with σ at s/c=0.065 inside passage: σ=0.77 (without cavitation), σ=0.180 (just before breakdown), σ=0.170 (breakdown onset), σ=0.166 (early breakdown), and σ=0.161 (deep breakdown). Dotted line in σ=0.77 indicates the boundary of the field of view in σ=0.180-0.161.

SPIV measurements have been conducted at conditions corresponding to φ=0.74-0.75 prior to breakdown at five different cavitation indices. Figure 7-8 shows the distribution of axial velocity magnitude ($|U_z|/U_T$) for the baseline case. The five conditions are: (i) high pressure when cavitation is suppressed (σ=0.77); (ii) close to, but before breakdown (σ=0.180); (iii) "breakdown onset", when attached cavitation oscillates and the head rise peaks (σ=0.170); (iv) "early breakdown" when the performance of the machine already deteriorates (σ=0.166); and (v) "deep breakdown" (σ=0.161), when the head coefficient is 9% lower than that without cavitation. For convenience, each velocity distribution is accompanied by the corresponding point on the head coefficient plot.

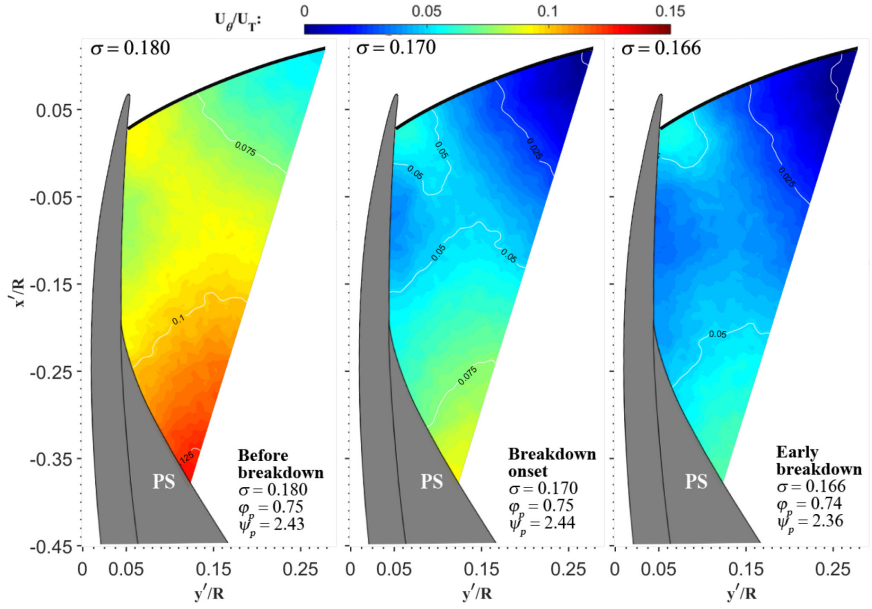

Figure 7-9 Evolution of U_θ for the baseline case: σ=0.180 (just before breakdown), σ=0.170 (breakdown onset), and σ=0.166 (early breakdown).

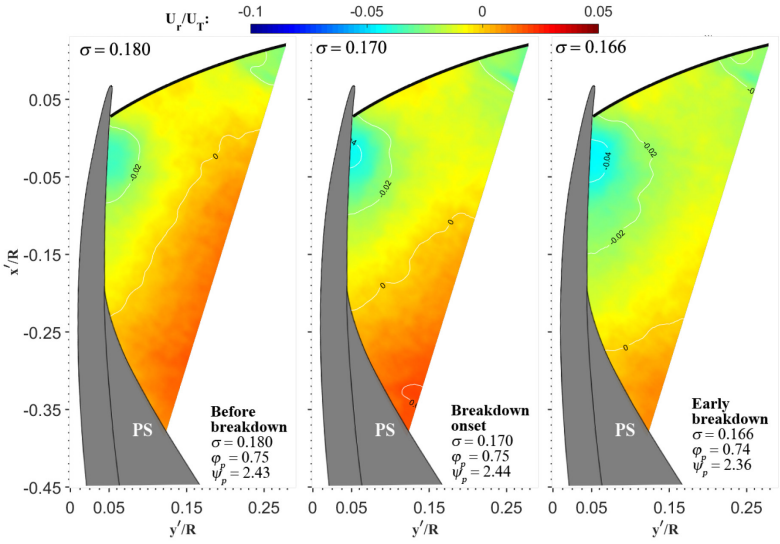

Figure 7-10 Evolution of U_r for the baseline case: σ=0.180 (just before breakdown), σ=0.170 (breakdown onset), and σ=0.166 (early breakdown)

At σ=0.77, $|U_z|$ is low near the endwall casing and along the PS, increasing with decreasing distance from the blade SS. The reduced velocity along the casing is associated with the casing

boundary layer as well as other phenomena, such as tip leakage flows, TLV formation, etc. (e.g., Bindon, 1989; Khalid *et al.*, 1999; Stauter, 1992). The low velocity along the PS is inherent. Due to partial visual blockage by the tip region cavitation, the FOVs for the other σ are smaller, as indicated by the dotted line. At σ=0.180, $|U_z|$ increases slightly essentially everywhere. Further reduction in pressure to σ=0.170 causes a substantial increase in velocity over almost the entire FOV, including the vicinity of the PS, but not in the tip region. For example, along the PS and at x'/R=-0.35, there is a 6% increase, from $0.395U_T$ to $0.420U_T$. Since the overall flow rate in the machine remains essentially unchanged, the increase in axial velocity along the PS is likely to be a result of (cavitation-induced) blockage in other regions of the rotor passage, predominantly along the SS. Recall that the visual observations indicate that at σ=0.170, the attached cavitation oscillates and extends rapidly into the blade overlap region (Figure 7-7a&d), supporting the argument about the effect of cavitation-induced blockage. A further slight decrease in cavitation index to σ=0.166, when the flow rate and the head rise start to drop, the axial velocity decreases in the outer parts of the PS and in the tip region but keeps on increasing along inner parts of the PS, at $x'/R<-0.2$. When the cavitation index is lowered further to σ=0.161, there is a reduction in axial flow over the entire FOV, including the PS, but especially along the endwall casing. The latter is presumably associated with the cavitation, including the cavitating TLV, the cloud cavitation near the trailing edge, and the large PCVs evident in Figure 7-6b&c.

Figure 7-9 shows the evolution of circumferential velocity for the baseline case at three different σ. The magnitude of U_θ is much smaller than $|U_z|$, but it decreases by about 50% at breakdown onset (σ=0.170), and keeps on decreasing as the cavitation index is reduced further. Note that a decrease in U_θ implies higher velocity relative to the blade (less swirl). The corresponding evolution of the radial velocity component is shown in Figure 7-10. The values are quite low almost everywhere and decrease with decreasing cavitation index. During the transition from σ=0.180 to σ=0.170, the combined effects of rapidly increasing $|U_z|$ and decreasing U_θ, the latter implying that in the rotor reference frame (Ωr-U_θ) increases, resulting in nearly unchanged

flow angle relative to the blade (not shown). Hence, the phenomena occurring during breakdown onset do not involve substantial changes to the incidence angle.

Knowledge of the velocity magnitude upstream and within the rotor passage enables us to use the Bernoulli equation to estimate the pressure distributions along the blade PS. Neglecting effects of viscous and Reynolds stresses and assuming a steady flow in the rotor reference frame, along a streamline

$$\frac{p}{\rho}+\frac{W^2}{2}-\frac{(\Omega r)^2}{2}=const \tag{7.8}$$

where W is the speed of the fluid in the rotor reference frame (Lakshminarayana, 1996; Lyman, 1993). In the current case, considering that U_r is very small (Figure 7-10), the radial displacement of the streamlines is negligible, and the $(\Omega r)^2/2$ is canceled. Hence, the time-averaged pressure in the passage is

$$p(r,\theta,z)=p_{in}+0.5\rho(U_{z,in}^2+(\Omega r)^2)-0.5\rho(U_r^2+(\Omega r-U_\theta)^2+U_z^2) \tag{7.9}$$

where $U_{z,in}$ is the measured axial velocity at z/R=0.65, well upstream of the rotor LE (Tan, 2015). Since the inlet condition have only been recorded at φ=0.76, the $U_{z,in}$ profiles at other flow rates are estimated by assuming the same radial distributions far upstream of the rotor and scaling the velocity magnitude accordingly. Since the present analysis focuses on the effect of cavitation on the performance of the machine, in addition to σ, we also define the local cavitation index

$$\sigma_{local}=\frac{p(r,\theta,z)-p_v}{0.5\rho U_T^2} \tag{7.10}$$

Its distribution along the PS of the blade will be used as a representative of the pressure difference across the blade when the SS is covered by attached cavitation. The distributions σ_{local} for the baseline case are shown in Figure 7-11. As is evident, the slight decrease in σ from 0.18 to 0.17 (breakdown onset) causes an order of magnitude larger decrease in σ_{local} everywhere in the passage. This drastic reduction in pressure is associated with the increase in velocity magnitude in the rotor reference frame. Further reduction in cavitation index to σ=0.166 causes a further significant

decrease in pressure along the inner part of the PS, but not at the same rate as that occurring between σ=0.18 to 0.17. In the rest of the passage, especially in the tip region, the pressure hardly changes. Between σ =0.16 to 0.161, the latter corresponding "deep breakdown", the pressure distribution changes very little across the FOV, but there is a decrease in the PS pressure at low x'/R.

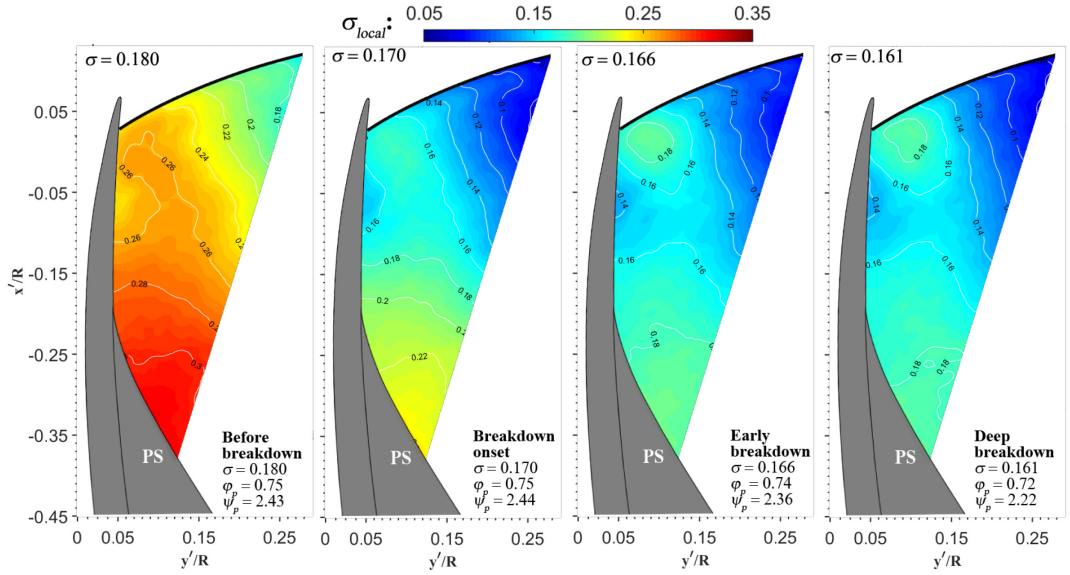

Figure 7-11 Evolution of σ_{local} for baseline case: σ=0.180 (just before breakdown), σ=0.170 (breakdown onset), σ=0.166 (early breakdown), and σ=0.161 deep breakdown.

Sample comparisons between the baseline and CG3 flow fields

Figure 7-12 compare the changes to $|U_z|$ as the cavitation index is reduced from pre-breakdown to breakdown-onset conditions for the baseline and CG3 cases. For the baseline case, we present ($|U_{z,\sigma=0.170}|$-$|U_{z,\sigma=0.180}|$), and for the CG3 cases, (($|U_{z,\sigma=0.173}|$-$|U_{z,\sigma=0.187}|$). The differences in the values of σ are caused by slight (<1 kPa) changes in the inlet pressure during the tests. The CG3 data also has a smaller field of view, which is indicated by the mask superimposed on the baseline figures. For both cases, the breakdown onset is characterized by an increase in axial velocity and a decrease in pressure along the blade PS. The differences between the two cases along the PS are quite small, but the increase in $|U_z|$ along the tip of the blade with CG3 is lower

than that of the baseline flow. Figure 7-13 provides a similar comparison between the baseline and CG3 cases, but this time the cavitation index is changed from pre-breakdown to deep breakdown conditions. Here, the area with decreasing $|U_z|$ indicating a blockage, and the magnitude of the decrease in the CG3 data are smaller than those of the baseline. This trend might be associated with the suppression of the PCVs further downstream, as shown in Figure 7-6e. Figure 7-14 shows three sample distributions of σ_{local} for CG3. Accounting for the differences in σ, the pre-breakdown and breakdown-onset pressure distributions are not significantly different from those of the baseline in Figure 7-11. Accordingly, the pressure coefficients are also marginally different. However, there is a difference at early breakdown (σ=0.164), where the pressure over the entire area is higher than that at σ=0.166 or 0.161 for the baseline data. The difference is significant, being higher by e.g., 0.04-0.06 along the PS of the CG3 distribution. Accordingly, the corresponding overall pressure coefficient of the CG3 setup is markedly higher, by 0.1-0.24, for similar flow rates. Hence, once the exact conditions are compared, adding the casing groves delays the rapid deterioration of PS pressure slightly and the overall performance in a more significant manner. However, this advantage is limited to a narrow range of flow coefficients and cannot be maintained as σ is decreased further (Figure 7-4 and Figure 7-6). The implications of these findings are addressed in the following discussion.

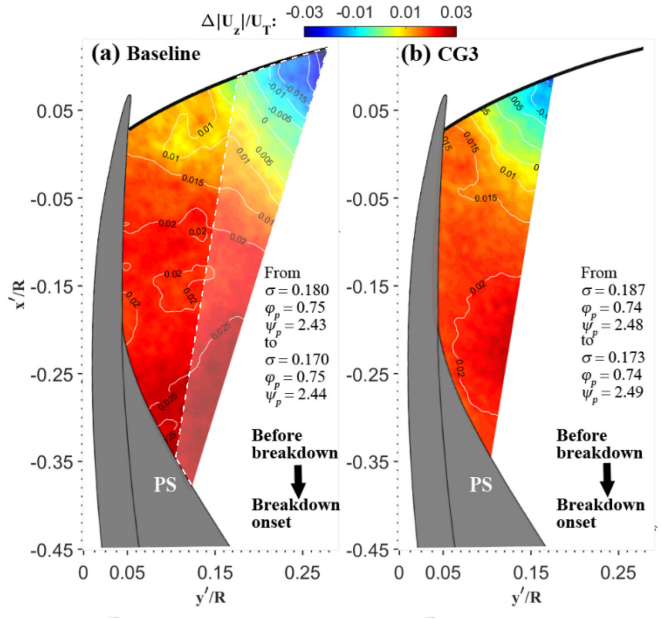

Figure 7-12 Changes in $|U_Z|$ with decreasing σ for (a) the baseline case ($|U_{z,\sigma=0.170}|-|U_{z,\sigma=0.180}|$) and (b) the CG3 case ($|U_{z,\sigma=0.173}|-|U_{z,\sigma=0.187}|$). The partially masked area in (a) is not available in (b).

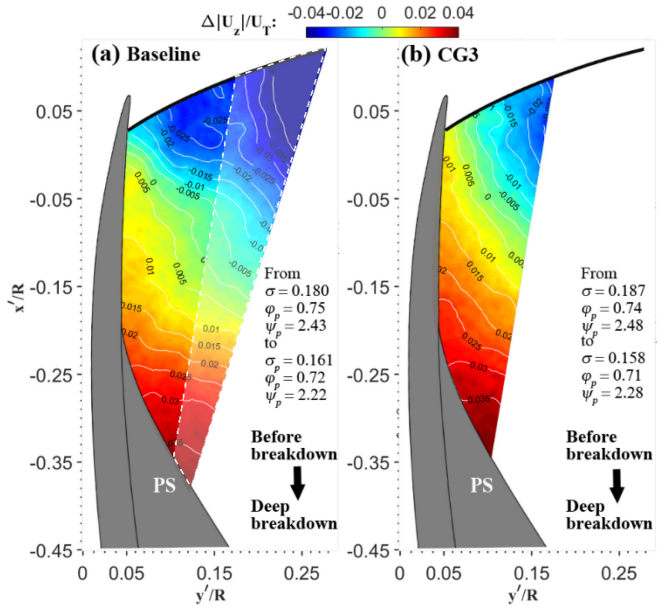

Figure 7-13 Changes in $|U_Z|$ with decreasing σ for (a) the baseline case (($|U_{z,\sigma=0.161}|-|U_{z,\sigma=0.180}|$) /$U_T$) and (b) the CG3 case (($|U_{z,\sigma=0.158}|-|U_{z,\sigma=0.187}|$) /$U_T$).

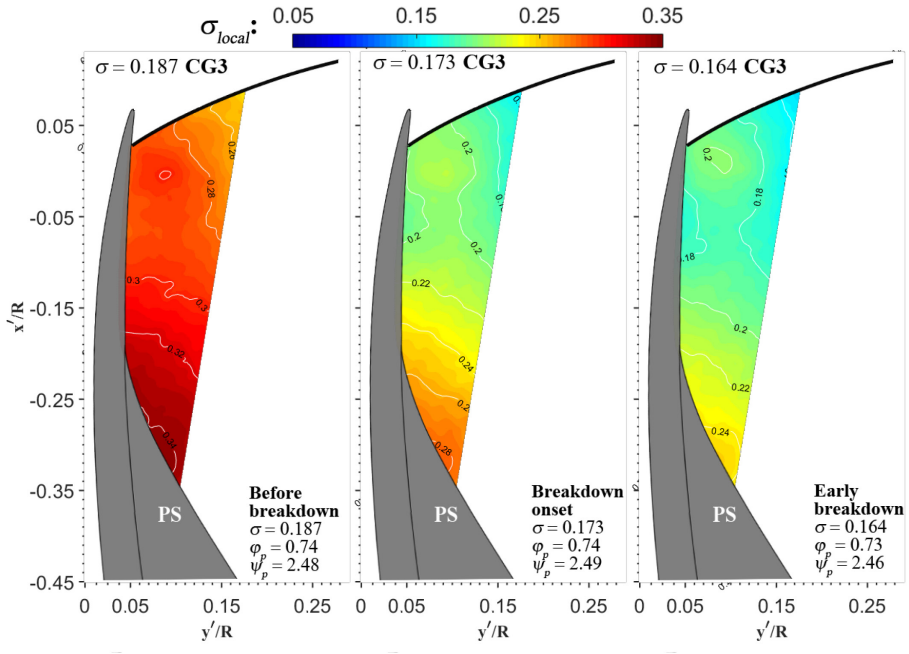

Figure 7-14 Evolution of σ_{local} for CG3 case: σ=0.187 (just before breakdown), σ=0.173 (breakdown onset) and σ=0.164 (early breakdown).

Discussion

In this section, we combine the present and previous findings of cavitation breakdown to introduce a plausible explanation for the mechanisms involved. The precursor for cavitation breakdown referred as breakdown onset in the current Chapter, occurs when the attached cavitation on the blade SS starts to expand into the blade overlap region, and the area covered by it fluctuates with large amplitudes (Figure 7-7). This phenomenon has been observed for all the tested cases and is consistent with the condition for breakdown observed for other machines by Pearsall (1973). At this cavitation index (σ=0.170 for the baseline case), the pump flow rate does not change, and the head increases slightly. The latter trend is consistent with simulations performed for the same pump geometry (Lindau *et al.*, 2012) and different machines (Guinard *et al.*, 1953; Stripling *et al.*, 1962). Yet, the SPIV measurements show that during breakdown onset, the mean axial velocity increases by 5-6% (Figure 7-8 and Figure 7-12) and the mean pressure decreases by more than 25% along the PS of the blade near the entrance to the overlap region

(Figure 7-11). The increase in axial velocity without a change in flow rate is presumably associated with a reduction in the through-flow area caused by the attached cavitation along the SS of the neighboring blade. The decrease in pressure over the entire entrance area is likely to reduce the pressure along the SS as well, resulting in a rapid expansion of the attached cavitation deep into the overlap region.

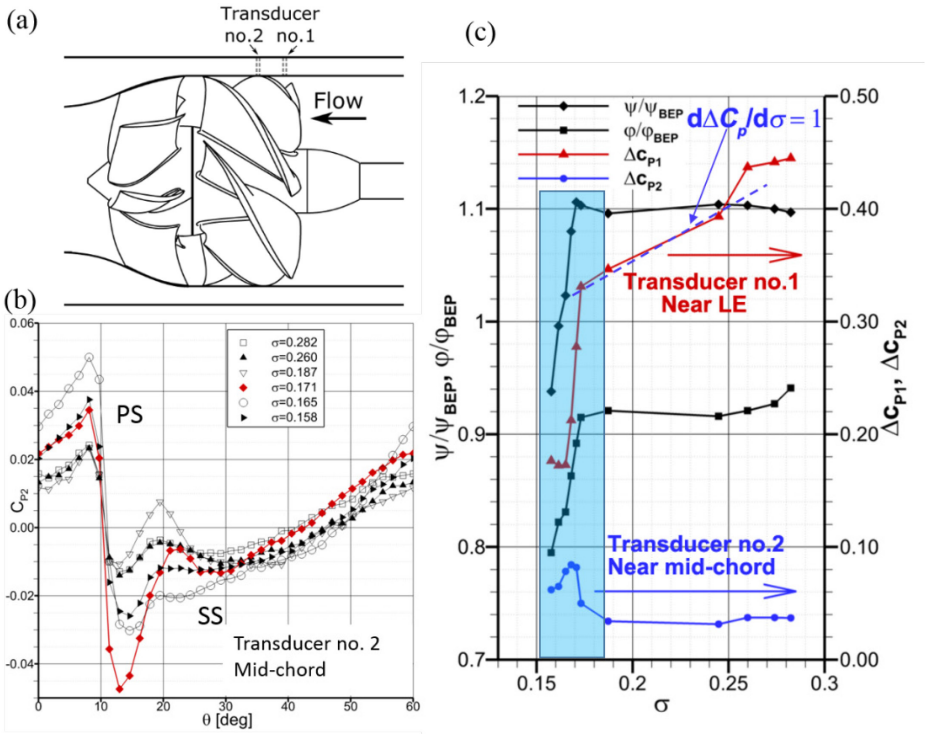

Figure 7-15 (a) Illustration of transducer locations. (b) Casing wall pressure variations near the mid-chord. (c) Pressure differences across the blade measured at casing wall at two different axial locations for the baseline case. (Adapted from Tan et al. 2015)

While the decrease in PS pressure concurrently with an increase in total head appears to be puzzling, it can be explained as follows: Measurements of pressure distributions on the surface of a cavitating 2D hydrofoil by Shen *et al.* (1989) show that the pressure inside the cavitation area on the SS is very close to the vapor pressure, and recovers to the fully wetted values only downstream of the cloud cavitation. Hence, in parts of the SS, the pressure is lower than that in a fully wetted flow. For this isolated foil, the pressure along the PS is not affected significantly by

the cavitation, at least as long as the SS cavitation does not reach the foil trailing edge. Consequently, partial cavitation actually increases the lift force. In the current pump, although PS pressure drops, it is accompanied by a rapid expansion of the SS cavitation and the area where the pressure is equal to the vapor pressure. Hence, the blade loading might still increase in spite of the decreases in PS pressure. Evidence supporting this argument can be obtained from the endwall casing pressure measurements in the same machine by Tan *et al.* (2015c) using two, fixed, flush-mounted piezoelectric transducers. The location of these transducers is indicated in Figure 7-15a. Transducer no. 1 is located near the blade LE (s/c=0.175), and Transducer no. 2, at the mid-chord (s/c=0.488). Sample ensemble-averaged pressure signals of Transducer no. 2 normalized by $0.5\rho U_T^2$ ($C_p=p(\theta)/0.5\rho U_T^2$)) for different σ are presented in Figure 7-15b. The sharp decrease in pressure occurs as the blade passes by the transducer, peaking on the PS, and reaching a minimum value along the SS, with the difference between them ($\Delta C_p=C_{p,\mathrm{PS}}- C_{p,\mathrm{SS}}$) representing the pressure difference across the blade. Hence, this difference can be used as a surrogate for the local loading near the blade tip. Note the sharp decrease in SS pressure at σ=0.171, the breakdown onset condition.

Figure 7-15c shows the effect of reducing σ on the pressure difference across the blade for both transducers along with the corresponding pump performance. As is evident, near the LE (transducer No. 1), the pressure difference decreases with decreasing σ, with $\partial\Delta C_p/\partial\sigma\sim1$ at $0.175<\sigma<0.25$. Under these conditions, the SS attached cavitation already extends to Transducer No. 1, hence the SS pressure is expected to be nearly constant and close to the vapor pressure. The slope of the ΔC_p line implies that the PS pressure decreases at the same rate as the inlet pressure, i.e. p_{ps}-p_{in} remains unchanged. The corresponding performance and flow rate remain nearly unchanged at $0.175<\sigma<0.25$, indicating that the decrease of blade loading near the LE must be compensated by an increase in blade loading somewhere else along the blade. According to Shen *et al.* (1989), the decrease in blade loading near the leading edge is compensated by an increase in pressure difference across the blade at higher chord fractions, where the pressure in the cavitation-

covered SS remains low. Indeed, as the SS cavitation expands to Transducer no. 2 at the breakdown onset conditions, ΔC_p (blade loading) increases at mid-chord, while drastically decreasing near the leading edge, consistent with the present observations. Figure 7-15b indicates that the increase in ΔC_{p2} is mostly attributable to the decrease in SS pressure. In Tan *et al.* (2015c), this decrease is associated with the formation of PCVs at the same location. The rapid decrease in ΔC_{p1} is attributed in this Chapter to cavitation-induced blockage once the attached cavitation reaches the blade overlap region. Considering that breakdown onset involves a rapid expansion of the SS area covered by cavitation, i.e., has a vapor pressure, a similar increase in ΔC_p most likely occurs over a broad fraction of the blade. This process might be the primary reason for the brief increase in the total head at σ=0.17. Although the cavitation-induced blockage reduced the PS pressure near the leading edge, the corresponding rapid expansion of the SS cavitation appears to make up for it.

While we cannot provide a substantiated explanation for the oscillation in the area covered by cavitation, once could still postulate about possible reasons. The rapid expansion of the SS cavitation is most likely a result of the cavitation-induced blockage, and the presently–observed corresponding increase in velocity and decrease in pressure over the entire wetted fraction of the passage (Figure 7-11). However, the expansion of the SS cavitation increases the pump performance, i.e., the pressure in the vicinity of the blade trailing edge. This increase is likely to shrink the area covered by cavitation, hence, reduce the total head and pressure in the passage. Consequently, the area covered by cavitation oscillates.

Upon further reduction in cavitation index, the head rise drops sharply, consistent with the blade loading reduction both at the LE and at mid-chord (Figure 7-15c). At deep breakdown, i.e., σ=0.161, the attached cavitation of the baseline case reaches the blade trailing edge (Figure 7-6b) and stops oscillating, while the pressure along the LE PS remains nearly unchanged (Figure 7-11). This trend is consistent with the plateau in ΔC_{p1} at σ<0.165 in Figure 7-15c. However, the blade loading near mid-chord keeps on decreasing, at least in the tip region, contributing to the

performance loss. In Tan *et al.* (2015c), the latter trend is attributed to the cavitation-induced blockage as the entire tip region becomes occupied by the PCVs (Figure 7-6c). The increased tip blockage is consistent with the persistent decrease in $|U_z|$ near the LE, as shown in Figure 7-8.

Finally, one has to answer why the grooves have a limited effect on the breakdown process (consistent with Choi *et al.* (2007)), in spite of the fact that they suppress the formation of PCVs and improve the machine performance during early phases of breakdown ($\sigma \geq 0.158$), as shown in Figure 7-6b&e. The PCVs reappear and the performance deteriorates rapidly upon further reduction in cavitation index, reaching conditions that are similar to those of the machine without grooves (Figure 7-4, and Figure 7-6e&f). The groove does reduce the blockage in the tip region under deep breakdown (Figure 7-13), but apparently, this effect is not sufficient for causing a significant delay the cavitation index corresponding to the breakdown. There are several possible reasons for this observation. First, away from the tip, the increase in axial velocity, decrease in PS pressure, and rapid expansion of the attached cavitation caused by cavitation-induced blockage when it reaches the blade overlap region during cavitation breakdown onset can be seen in both cases (Figure 7-11-Figure 7-14). Hence, the effect of the groove is limited to the tip region. Second, for $\sigma<0.16$, the reappearance of the PCVs indicates that the present groove is no longer effective, resulting in a growing tip region blockage. Larger or different geometry grooves might have been more effective, but it is not clear to what extent. It should be noted that in addition to the PCVs, the SS tip near the trailing edge under the PCVs is occupied by cloud cavitation as well. Hence, suppressing the PCVs might not be sufficient, requiring additional means to alleviate the effect of the cloud cavitation.

7.3 Summary

Performance tests, high-speed imaging, and SPIV measurements have been carried out to study the flow structures and pressure within the rotor passage of an axial waterjet pump during cavitation breakdown. A Prior study (Tan *et al.*, 2015c) in our lab has attributed this phenomenon

to the formation of large scale perpendicular cavitating vortices, which block the flow in the tip region. In recent experiments, we have tried to use circumferential grooves placed in several axial locations to manipulate the tip leakage flow, hoping to affect the PCV formation. These observations show that when the CG is located near the blade trailing edge, using the so-called CG3, the PCV formation is delayed. However, it causes only a limited effect on the conditions for cavitation breakdown, in agreement with previous studies (Choi *et al.*, 2007). Consistent with Pearsall (1973), the onset of breakdown occurs when the attached cavitation on the blade SS reaches the blade overlap region, with or without casing grooves, and at all flow rates. Just before the rapid performance degradation, the attached cavitation expands rapidly with large oscillations in the SS area covered by it. Blockage to the through-flow area at the entrance to the overlap region accelerates the flow in the remaining area, causing a significant (~25%) reduction to the pressure along the blade PS. This pressure reduction presumably causes further expansion of the attached cavitation on the SS. At this stage, the performance is not degraded yet, and in-fact the pump head even increases slightly, consistent with RANS simulations of the same pump performed by Kim *et al.* (2010) and Lindau *et al.* (2012) as well as numerous studies performed in other machines. From the measurements of the pressure difference across the blade tip at mid-passage, it appears that reduction in the SS pressure as the attached cavitation expands rapidly compensates for the reduction in PS pressure, causing an increase in overall performance. The resulting increase in pressure rise across the blade passage might oppose the expansion of the SS cavitation area, causing the high amplitude oscillation.

A further slight reduction in cavitation index causes rapid deterioration in flow rate and head, increased tip region blockage, but a slight increase in velocity and decrease in PS pressure at mid-span. The SS cavitation expands to the vicinity of the blade trailing edge, and the oscillations in coverage diminish. At mid-span, with the SS maintained at the vapor pressure, and the PS pressure decreasing, the pump performance deteriorates. In the tip region, PCVs extending from the SS of one blade to the PS of the neighboring one occupy most of the tip region in the

overlap area. Cloud cavitation also appears under the PCVs, but only near the SS. Both structures appear to contribute to the tip region blockage. While the trailing edge casing groove delays the PCV formation, it has a limited effect on the cloud cavitation. Hence, the groove is only partially effective in reducing the tip region blockage. During early phases of breakdown, suppression of the PCVs by CG3 indeed causes a limited improvement to the tip blockage and performance of the pump. However, with a further slight reduction in cavitation index, the PCVs reappear.

Conclusions

This experimental work focuses on two extreme phenomena happening in axial turbomachines, namely the stall in the NASA compressor and the cavitation breakdown in AxWJ-2 waterjet pump. High-speed image of cavitation and high-resolution PIV measurements reveal the detailed flow structures associated with them. In an attempt to delay or alleviate their adverse effects, axial and circumferential grooves are installed and tested.

The stall in the NASA compressor is associated with the formation and propagation of backflow vortices (BFVs). They rollup in the shear layer between the swirling backflow and the incoming main passage flow. When the flow rate is low, the BFV grows perpendicularly at the blade suction side (SS) and propagates diagonally to the pressure side (PS) of the next blade. When it reaches the next blade passage through the tip gap or around the leading edge (LE), it triggers the formation of a similar structure. The BFVs also cause intermittent, but significant changes to the incidence angle upstream of the blade LE. Such incidence changes might cause LE flow separation in a highly loaded machine, as observed in other studies at the onset of stall. The number and size of the BFVs increase dramatically when the flow rate is further reduced into the stall range, and they rotate with the blade, indicating little or no through-flow in the tip region.

Installing semicircular axial casing grooves (ACGs) reduces the stall flow rate of the NASA compressor by 40%, causes a substantial increase in pressure rise at low flow rates, and degrades the performance at higher flow rates. Detailed SPIV measurements have shown that a periodic circulating flow enters the grooves at the downstream end and exits at the upstream edge. The inflow peaks when the downstream end of the groove is aligned with the PS of the blade, and decreases, but does not vanish when this end is located near the SS. Flow separation occurs at the groove corners as the flow enters and leaves the groove, creating secondary flows there. The

grooves periodically remove the tip flow associated with the TLV and reduce its strength. The outflow carries negative circumferential velocity and enters the flow upstream of the LE, periodically increasing the rotor blade incidence angle. The grooves constrain the region where the BFVs can form, and prevent them from reaching the LE of the next blade. However, at high flow rates, the separating vortex at groove downstream corner moves towards the blade passage, blocking part of the flow there. Interactions with the TLV results in a much larger and more broadly distributed TLV circulation. The increase in incidence angle shifts the blade loading more towards the LE. All of those are associated with the efficiency loss at high flow rates. Since the ACGs installed near the blade LE have multiple effects on the flow structure, to determine which of these phenomena is a key contributor, a series of grooves with the same inlet geometry, but with outlets aimed at different directions are tested. Results have shown that the grooves with exits aligned in the positive circumferential direction achieve a substantial stall margin improvement but without causing efficiency loss at high flow rates.

High-speed images of cavitation in the rotor passage of the AxWJ-2 waterjet pump have shown the developments of different cavitating phenomena during cavitation breakdown. Combined with detailed SPIV measurements in the rotor passage, a plausible explanation for cavitation breakdown is obtained. The onset of breakdown occurs when the attached cavitation on the blade SS reaches the blade overlap region. Blockage to the through-flow area at the entrance to the overlap region accelerates the flow in the remaining area, causing a significant (~25%) reduction to the pressure along the blade PS. This pressure reduction presumably causes further expansion of the attached cavitation on the SS. A further slight reduction in mean pressure causes rapid deterioration in flow rate and head and increased tip region blockage. The SS cavitation expands to the vicinity of the blade trailing edge. At mid-span, as the SS maintained at the vapor pressure, and the PS pressure decreasing, the pump performance deteriorates. In the tip region, perpendicular cavitating vortices (PVCs) extending from the SS of one blade to the PS of the neighboring one occupy most of the tip region in the overlap area. Cloud cavitation also appears

under the PCVs, but only near the SS. Both structures appear to contribute to the tip region blockage and pump performance deterioration. Attempts to mitigate the dramatic performance breakdown by circumferential grooves achieve only limited success, as the shallow grooves unable to affect the cloud cavitation that fills the trailing edge tip region at deep breakdown.

Bibliography

Adrian, R., & Westerweel, J. (2011). Particle Image Velocimetry, New York: Cambridge University Press, pp. 241–248.

Arndt, R. E. A. (1981). Cavitation in Fluid Machinery and Hydraulic Structures. *Annual Review of Fluid Mechanics*, **13**, pp.273–328.

Arndt, R. E. a. (2002). Cavitation in Vortical Flows. *Annu. Rev. Fluid Mech*, **34**, pp.143–175.

Bai, K., & Katz, J. (2014). On the Refractive Index of Sodium Iodide Solutions for Index Matching in PIV. *Experiments in Fluids*, **55**(4), pp.1–6.

Beheshti, B. H., Teixeira, J. A., Ivey, P. C., Ghorbanian, K., & Farhanieh, B. (2004). Parametric Study of Tip Clearance—Casing Treatment on Performance and Stability of a Transonic Axial Compressor. *Journal of Turbomachinery*, **126**(4), pp.527–535.

Bindon, J. P. (1989). The Measurement and Formation of Tip Clearance Loss. *Journal of Turbomachinery*, **111**(3), pp.257.

Brandstetter, C., Kegalj, M., Wartzek, F., Heinichen, F., & Schiffer, H.-P. (2014). Stereo PIV Measurement of Flow Structures underneath an Axial-Slot Casing Treatment on a One and a Half Stage Transonic Compressor. In *17th International Symposium on Applications of Laser Techniques to Fluid Mechanics*, Lisbon, Portugal, pp. 1–18.

Brennen, C. E. (1994). *Hydrodynamics of Pumps*, Concepts ETI and Oxford University Press. doi:10.1017/CBO9780511976728

Camp, T. R., & Day, I. J. (1998). A Study of Spike and Modal Stall Phenomena in a Low-

Speed Axial Compressor. *Journal of Turbomachinery*, **120**(7), pp.393–401.

Chen, H., Doeller, N., Li, Y., & Katz, J. (2017a). Measurements of the Flow and Pressure within an Axial Waterjet Pump during Cavitation Breakdown. In *International Symposium on Transporat Phenomena and Dynamics of Rotating Machinery*, Maui, pp. 1–12.

Chen, H., Koley, S. S., Li, Y., & Katz, J. (2019). Systematic Experimental Evaluations aimed at Optimizing the Geometry of Axial Casing Grooves In a Compressor. In *Proceedings of ASME Turbo Expo 2019: Turbomachinery Technical Conference and Exposition*, Phoenix, AZ, pp. 1–13.

Chen, H., Li, Y., Doeller, N., Koley, S. S., Keyser, B., & Katz, J. (2016). Effects of Circumferential Grooves on the Cavitation and Performance of an Axial Waterjet Pump. *31th Symposium on Naval Hydrodynamics*, (September).

Chen, H., Li, Y., & Katz, J. (2018). On the Interactions of a Rotor Blade Tip Flow With Axial Casing Grooves in an Axial Compressor Near the Best Efficiency Point. *Journal of Turbomachinery*, **141**(1), pp.011008.

Chen, H., Li, Y., Koley, S. S., Doeller, N., & Katz, J. (2017b). An Experimental Study of Stall Suppression and Associated Changes to the Flow Structures in the Tip Region of an Axial Low Speed Fan Rotor by Axial Casing Grooves. *Journal of Turbomachinery*, **139**(12), pp.121010.

Chen, H., Li, Y., Tan, D., & Katz, J. (2017c). Visualizations of Flow Structures in the Rotor Passage of an Axial Compressor at the Onset of Stall. *Journal of Turbomachinery*, **139**(4), pp.041008.

Chesnakas, C. J., Donnelly, M. J., Pfitsch, D. W., Becnel, A. J., & Schroeder, S. D. (2009).

Performance Evaluation of the ONR Axial Waterjet 2 (AxWJ-2). No. NSWCCD-50-TR-2009/089, West Bethesda, MD.

Choi, Y.-D., Kurokawa, J., & Imamura, H. (2007). Suppression of Cavitation in Inducers by J-Grooves. *Journal of Fluids Engineering*, **129**(January 2007), pp.15–22.

Chow, Y.-C., Uzol, O., Katz, J., & Meneveau, C. (2005). Decomposition of the spatially filtered and ensemble averaged kinetic energy, the associated fluxes and scaling trends in a rotor wake. *Physics of Fluids*, **17**(8), pp.085102.

Chudina, M. (2003). Noise as an indicator of cavitation in a centrifugal pump. *Acoustical Physics*, **49**(4), pp.463–474.

Crook, A. J., Greitzer, E. M., Tan, C. S., & Adamczyk, J. J. (1993). Numerical Simulation of Compressor Endwall and Casing Treatment Flow Phenomena. *J. Turbomach.*, **115**(3), pp.501–512.

Day, I. J. (1993). Stall Inception in Axial Flow Compressors. *Journal of Turbomachinery*, **115**(1), pp.1–9.

Day, I. J. (2015). Stall, Surge, and 75 Years of Research. *Journal of Turbomachinery*, **138**(1), pp.011001.

Deppe, A., Saathoff, H., & Stark, U. (2005). Spike-Type Stall Inception in Axial-Flow Compressors. In *Proceedings of the 6th European Conference on Turbomachinery*, Lille, France, pp. 178–188.

Djeghri, N., Vo, H. D., & Yu, H. (2015). Parametric Study for Losses Casing Treatment on a Mixed-Flow Compressor Rotor. In *Proceedings of the ASME Turbo Expo 2015: Turbine Technical Conference and Exposition*, Montreal, Canada, pp. GT2015-42750.

Emmons, H., W., Person, C., E., & Grant, H., P. (1955). Compressor Surge and Stall Propagation. *Trans ASME*, **77**(4), pp.455–469.

Everitt, J. N., & Spakovszky, Z. S. (2012). An Investigation of Stall Inception in Centrifugal Compressor Vaned Diffuser. *Journal of Turbomachinery*, **135**(1), pp.011025.

Fujita, H., & Takata, H. (1984). A Study on Configurations of Casing Treatment for Axial Flow Compressors. *Bulletin of JSME*, **27**(230), pp.1675–1681.

Fukano, T., & Jang, C. M. (2004). Tip Clearance Noise of Axial Flow Fans Operating at Design and Off-Design Condition. *Journal of Sound and Vibration*, **275**(3), pp.1027–1050.

Furukawa, M., Inoue, M., Saiki, K., & Yamada, K. (1998). The Role of Tip Leakage Vortex Breakdown in Compressor Rotor Aerodynamics. In *ASME 1998 International Gas Turbine and Aeroengine Congress and Exhibition*, p. V001T01A054.

Garnier, V. H., Epstein, A. H., & Greitzer, E. M. (1991). Rotating Waves as a Stall Inception Indication in Axial Compressors. *Journal of Turbomachinery*, **113**(4), pp.290–301.

Greitzer, E. M. (1976). Surge and Rotating Stall in Axial Flow Compressors—Part I: Theoretical Compression System Model. *Journal of Engineering for Power*, **98**(2), pp.190.

Guinard, P., Fuller, T., & Acosta, A. (1953). An Experimental Study of Axial Flow Pump Cavitation. In *California Institute of Technology Hydrodynamics Laboratory Report No. E-19.3*, Pasadena, California, pp. 1–19.

Hah, C., Bergner, J., & Schiffer, H.-P. (2006). Short Length-Scale Rotating Stall Inception in a Transonic Axial Compressor – Criteria and Mechanisms. In *Proceedings of ASME Turbo Expo 2006*, pp. GT2006-90045.

Hah, C., Hathaway, M., & Katz, J. (2014). Investigation of Unsteady Flow Field in a Low-Speed One and a Half Stage Axial Compressor, Part 2: Effects of Tip Gap Size on the Tip Clearance Flow Structure At Near Stall Operation. *ASME Turbo Expo*, pp.GT2014-27094.

Houghton, T., & Day, I. (2011). Enhancing the Stability of Subsonic Compressors Using Casing Grooves. *Journal of Turbomachinery*, **133**(2), pp.021007.

Hoying, D. a., Tan, C. S., Vo, H. D., & Greitzer, E. M. (1999). Role of Blade Passage Flow Structurs in Axial Compressor Rotating Stall Inception. *Journal of Turbomachinery*, **121**(4), pp.735–742.

Inoue, M., & Kuroumaru, M. (1989). Structure of Tip Clearance Flow in an Isolated Axial Compressor Rotor. *Journal of Turbomachinery*, **111**(3), pp.250.

Inoue, M., Kuroumaru, M., Tanino, T., Yoshida, S., & Furukawa, M. (2001). Comparative Studies on Short and Long Length-Scale Stall Cell Propagating in an Axial Compressor Rotor. *Journal of Turbomachinery*, **123**(1), pp.24–32.

Inoue, M., Kuroumaru, M., Yoshida, S., & Furukawa, M. (2002). Short and Long Length-Scale Disturbances Leading to Rotating Stall in an Axial Compressor Stage With Different Stator/Rotor Gaps. *Journal of Turbomachinery*, **124**(3), pp.376–384.

Jakobsen, J. K. (1964). On the Mechanism of Head Breakdown in Cavitating Inducers. *Journal of Basic Engineering*, **86**(2), pp.291–305.

Kang, D., Arimoto, Y., Yonezawa, K., … Tsujimoto, Y. (2010). Suppression of Cavitation

Instabilities in an Inducer by Circumferential Groove and Explanation of Higher Frequency Components. *International Journal of Fluid Machinery and Systems*, **3**(2), pp.137–149.

Khalid, S. A., Khalsa, A. S., Waitz, I. A., Marble, F. E. (1999). Endwall Blockage in Axial Compressors. *Journal of Turbomachinery*, **121**(3), pp.499.

Kim, S., & Schroeder, S. (2010). Numerical Study of Thrust-Breakdown Due to Cavitation on a Hydrofoil , a Propeller , and a Waterjet. In *28th Symposium on Naval Hydrodynamics*, Pasadena, California.

Kosyna, G., Goltz, I., & Stark, U. (2005). Flow Structure of an Axial-Flow Pump from Stable Operation to Deep Stall. In *ASME Fluids Engineering Division Summer Meeting and Exhibition*, Houston, TX, pp. FEDSM2005-77350.

Lakshminarayana, B. (1996). *Fluid Dynamics and Heat Transfer of Turbomachinery*, John Wiley & Sons.

Li, Y. (2018). *Effects of Tip Gap Sizes and Operating Conditions on the Flow Structures and the Complex Turbulence in the Tip Region of An Axial Compressor Rotor*, The Johns Hopkins University.

Li, Y., Chen, H., & Katz, J. (2017). Measurements and Characterization of Turbulence in the Tip Region of an Axial Compressor Rotor. *Journal of Turbomachinery*, **139**(12), pp.121003.

Li, Y., Chen, H., & Katz, J. (2019). Challenges in Modeling of Turbulence in the Tip Region of Axial Turbomachines. *Journal of Ship Research*, pp.1–13.

Li, Y., Chen, H., Tan, D., & Katz, J. (2016). Effects of Tip Clearance and Operating Conditions on the Flow Structure and Reynolds Stresses within an Axial Compressor

Rotor Passage. *ASME Turbo Expo*, pp.GT2016-57050.

Lindau, J. W., Pena, C., Baker, W. J., Paterson, E. G. (2012). Modeling of Cavitating Flow through Waterjet Propulsors. *International Journal of Rotating Machinery*, **2012**, pp.1–13.

Lyman, F. A. (1993). On the Conservation of Rothalpy in Turbomachines. *Journal of Turbomachinery*, **115**(3), pp.520.

Mailach, R., Lehmann, I., & Vogeler, K. (2001). Rotating Instabilities in an Axial Compressor Originating From the Fluctuating Blade Tip Vortex. *Journal of Turbomachinery*, **123**(3), pp.453–463.

März, J., Hah, C., & Neise, W. (2002). An Experimental and Numerical Investigation into the Mechanisms of Rotating Instability. *Journal of Turbomachinery*, **124**(7), pp.367–375.

Mathioudakis, K., & Breugelmans, F. A. E. (1985). Development of Small Rotating Stall in a Single Stage Axial Compressor. *ASME Paper*, **85-GT-227**. doi:NACA-TN-3823

McDougall, N. M., Cumpsty, N. A., & Hynes, T. P. (1990). Stall Inception in Axial Compressors. *Journal of Turbomachinery*, **112**(1), pp.116.

Michael, T. J., Schroeder, S. D., & Becnel, A. J. (2008). *Design of the ONR AxWJ-2 Axial Flow Water Jet Pump. No. NSWCCD-50-TR-2008/066*, West Bethesda, MD.

Miorini, R. L., Wu, H., & Katz, J. (2012). The Internal Structure of the Tip Leakage Vortex Within the Rotor of an Axial Waterjet Pump. *Journal of Turbomachinery*, **134**(3), pp.031018.

Moore, R. D., Kovich, G., & Blade, R. J. (1971). Effect of Casing Treatment on Overall and Blade Element Performance of a Compressor Rotor. *NASA Techincal Note*,

pp.TN D-6538.

Müller, M. W., Schiffer, H.-P., Voges, M., & Hah, C. (2011). Investigation of Passage Flow Features in a Transonic Compressor Rotor. In *Proceedings of ASME Turbo Expo 2011: Power for Land, Sea and Air*, Vancouver, Canada, pp. 1–11.

Ng, S. L., & Brennen, C. (1978). Experiments on the dynamic behavior of cavitating pumps. *Journal of Fluids Engineering*, **100**(6), pp.166–176.

Osborn, W. M., Lewis, G. W. J., & Heidelberg, L. J. (1971). Effect of Several Porous Casing Treatments on Stall Limit and on Overall Performance of an Axial-Flow Compressor Rotor. *NASA Techincal Note*, pp.TN D-6537.

Pampreen, R. C. (1993). *Compressor Surge and Stall*, Concepts ETI.

Pearsall, I. S. (1973). Design of Pump Impellers for Optimum Cavitation Performance. *Proceedings of the Institution of Mechanical Engineers*, **187**(55), pp.667–678.

Philipp, A., & Lauterborn, W. (1998). Cavitation erosion by single laser-produced bubbles. *Journal of Fluid Mechanics*, **361**, pp.75–116.

Prince, D. C., Wisler, D. C., & Hilvers, D. E. (1975). A Study of Casing Treatment Stall Margin Improvement Phenomena. In *Volume 1A: General*, ASME, p. V01AT01A059.

Pullan, G., Young, A. M., Day, I. J., Greitzer, E. M., & Spakovszky, Z. S. (2015). Origins and Structure of Spike-Type Rotating Stall. *Journal of Turbomachinery*, **137**(5), pp.051007.

Roth, G. I., & Katz, J. (2001). Five Techniques for Increasing the Speed and Accuracy of PIV Interrogation. *Measurement Science and Technology*, **12**(3), pp.238–245.

Schoenenborn, H., & Breuer, T. (2012). Aeroelasticity at Reversed Flow Conditions —

Part II: Application to Compressor Surge. *Journal of Turbomachinery*, **134**(6), pp.061031.

Schrapp, H., Stark, U., Goltz, I., Kosyna, G., & S, B. (2004). Structure of The Rotor Tip Flow in a Highly-Loaded Single-Stage Axial-Flow Pump Approaching Stall. Part I: Breakdown of the Tip-Clearance Vortex. In *Proceedings of the ASME Heat Transfer/Fluids Engineering Summer Conference*, Charlotte, NC, pp. 307–312.

Seitz, P. A. (1999). *Casing Treatment for Axial Flow Compressors*, University of Cambridge.

Shen, Y., & Dimotakis, P. E. (1989). The Influence of Surface Cavitation on Hydrodynamic Forces. In *American Towing Tank Conference.*, pp. 44–53.

Smith, G. D. J., & Cumpsty, N. A. (1984). Flow Phenomena in Compressor Casing Treatment. *Journal of Engineering for Gas Turbines and Power*, **106**(3), pp.532–541.

Soranna, F., Chow, Y.-C., Uzol, O., & Katz, J. (2006). The Effect of Inlet Guide Vanes Wake Impingement on the Flow Structure and Turbulence Around a Rotor Blade. *Journal of Turbomachinery*, **128**(1), pp.82.

Stauter, R. C. (1992). Measurement of the Three-Dimensional Tip Region Flowfield in an Axial Compressor. In *Volume 1: Turbomachinery*, Vol. 115, ASME, p. V001T01A072.

Stripling, I. R., & Acosta, A. J. (1962). Cavitation in Turbo Pumps-Part 1. *Journal of Basic Engineering*, **1**(61), pp.1–13.

Takata, H., & Tsukuda, Y. (1977). Stall Margin Improvement by Casing Treatment --- Its Mechanism and Effectiveness. *Journal of Engineering for Power*, **99**(1), pp.121–133.

Tan, C. S., Day, I., Morris, S., & Wadia, a. (2010). Spike-Type Compressor Stall

Inception, Detection, and Control. *Annual Review of Fluid Mechanics*, **42**(1), pp.275–300.

Tan, D. (2015). *Common Features in the Structure of Tip Leakage Flows*, PhD Thesis, The Johns Hopkins University.

Tan, D., Li, Y., Chen, H., Wilkes, I., & Katz, J. (2015a). The Three Dimensional Flow Structure and Turbulence in the Tip Region of an Axial Flow Compressor. In *ASME Turbo Expo 2015: Turbine Technical Conference and Exposition*, pp. GT2015-43385.

Tan, D., Li, Y., Wilkes, I., Miorini, R., & Katz, J. (2015b). Visualization and Time Resolved PIV Measurements of the Flow in the Tip Region of a Subsonic Compressor Rotor. *Journal of Turbomachinery*, **137**(4), pp.041007.

Tan, D., Li, Y., Wilkes, I., Vagnoni, E., Miorini, R., & Katz, J. (2015c). Experimental Investigation of the Role of Large Scale Cavitating Vortical Structures in Performance Breakdown of an Axial Waterjet Pump. *Journal of Fluids Engineering*, **137**(11), pp.111301.

Tan, D., Miorini, R. L., Keller, J., & Katz, J. (2012). Flow Visualization Using Cavitation Within Blade Passage of an Axial Waterjet Pump Rotor. In *Proceedings of the ASME 2012 Fluids Engineering Summer Meeting*, Rio Grande, Puerto Rico. doi:10.1115/FEDSM2012-72108

Tsujimoto, Y., Yoshida, Y., Maekawa, Y., Watanabe, S., & Hashimoto, T. (1997). Observations of Oscillating Cavitation of an Inducer. *Journal of Fluids Engineering*, **119**(4), pp.775.

Uzol, O., Chow, Y. C., Katz, J., & Meneveau, C. (2001). Unobstructed PIV measurements

within an axial turbo-pump using liquid and blades with matched refractive indices. *DLR-Mitteilung*, **33**(3), pp.251–260.

Vo, H. D., Tan, C. S., & Greitzer, E. M. (2008). Criteria for Spike Initiated Rotating Stall. *Journal of Turbomachinery*, **130**(1), pp.011023.

Weichert, S., Day, I., & Freeman, C. (2011). Self-Regulating Casing Treatment for Axial Compressor Stability Enhancement. In *Asme Turbo Expo*, Vancouver, Canada: ASME, p. 13.

Westerweel, J., & Scarano, F. (2005). Universal Outlier Detection for PIV Data. *Experiments in Fluids*, **39**(6), pp.1096–1100.

Wieneke, B. (2005). Stereo-PIV Using Self-Calibration on Particle Images. *Experiments in Fluids*, **39**(2), pp.267–280.

Wilke, I., & Kau, H.-P. (2004). A Numerical Investigation of the Flow Mechanisms in a High Pressure Compressor Front Stage With Axial Slots. *Journal of Turbomachinery*, **126**(3), pp.339–349.

Wu, H., Miorini, R. L., & Katz, J. (2011a). Measurements of the Tip Leakage Vortex Structures and Turbulence in the Meridional Plane of an Axial Water-Jet Pump. *Experiments in Fluids*, **50**(4), pp.989–1003.

Wu, H., Miorini, R. L., Tan, D., & Katz, J. (2012). Turbulence Within the Tip-Leakage Vortex of an Axial Waterjet Pump. *AIAA Journal*, **50**(11), pp.2574–2587.

Wu, H., Tan, D., Miorini, R. L., & Katz, J. (2011b). Three-Dimensional Flow Structures and Associated Turbulence in the Tip Region of a Waterjet Pump Rotor Blade. *Experiments in Fluids*, **51**(6), pp.1721–1737.

Yamada, K., Furukawa, M., Nakano, T., & Inoue, M. (2004). Unsteady Three-

Dimensional Flow Phenomena Due to Breakdown of Tip Leakage Vortex in a Transonic Axial Compressor Rotor. In *ASME Turbo Expo 2004: Power for Land, Sea, and Air*, pp. 515–526.

Yamada, K., Kikuta, H., Iwakiri, K., Furukawa, M., & Gunjishima, S. (2013). An Explanation for Flow Features of Spike-Type Stall Inception in an Axial Compressor Rotor. *Journal of Turbomachinery*, **135**(2), pp.021023.

Yamamoto, K., & Tsujimoto, Y. (2009). Backflow Vortex Cavitation and Its Effects on Cavitation Instabilities. *International Journal of Fluid Machinery and Systems*, **2**(1), pp.40–54.

Yamanishi, N., Fukao, S., Qiao, X., Kato, C., & Tsujimoto, Y. (2007). LES Simulation of Backflow Vortex Structure at the Inlet of an Inducer. *Journal of Fluids Engineering*, **129**(5), pp.587–594.

Yokota, K., Kurahara, K., Kataoka, D., Tsujimoto, Y., & Acosta, A. J. (1999). A Study of Swirling Backflow and Vortex Structure at the Inlet of an Inducer. *JSME International Journal*, **42**(3), pp.451–459.

Yokota, K., Mitsuda, K., Tsujimoto, Y., & Kato, C. (2004). A Study of Vortex Structure in the Shear Layer Between Main Flow and Swirling Backflow. *Jsme International Journal Series B-Fluids and Thermal Engineering*, **47**(3), pp.541–548.

Young, A., Day, I., & Pullan, G. (2012). Stall Warning by Blade Pressure Signature Analysis. *Journal of Turbomachinery*, **135**(1), pp.011033.

Yu, X., Liu, B., & Jiang, H. (2007). Characteristics of the Tip Leakage Vortex in a Low-Speed Axial Compressor. *AIAA Journal*, **45**(4), pp.870–878.

Zhang, D., Shi, L., Shi, W., Zhao, R., Wang, H., & van Esch, B. P. M. (2015). Numerical

analysis of unsteady tip leakage vortex cavitation cloud and unstable suction-side-perpendicular cavitating vortices in an axial flow pump. *International Journal of Multiphase Flow*, **77**, pp.244–259.

Curriculum Vitae

EDUCATION

Johns Hopkins University, Baltimore, MD, USA

Ph.D. in Mechanical Engineering, Mar 2019

Johns Hopkins University, Baltimore, MD, USA

Master of Science in Engineering, May, 2016

Beijing University of Aeronautics and Astronautics, Beijing, China

Master of Science in Fluid Mechanics, Mar, 2013

Beijing University of Aeronautics and Astronautics, Beijing, China

Bachelor of Science in Engineering Mechanics, July, 2010

RESEARCH EXPERIENCE

Johns Hopkins University (8/2013 - present)

Research Assistant (Supervisor: Dr. Joseph Katz)

- Assembled and maintained the optical refractive index-matched facility at JHU.
- Installed the NASA experimental compressor and the Naval AxWJ-2 waterjet pump.
- Conducted performance measurements (flow rate, pressure and torque) on axial turbomachines.
- Performed high-speed imaging flow visualizations of cavitating structures in axial turbomachines.
- Studied the cavitation performance breakdown in the AxWJ-2 waterjet pump.

Detailed SPIV and pressure measurements in the non-cavitating part of the rotor passage revealed the mechanisms for cavitation breakdown.

- Studied the onset of stall in the NASA compressor. Key flow structures associated with the onset of stall have been identified and studied.
- Performed experiments to study the effects of semicircular skewed axial casing grooves on the performance and flow structures in the NASA compressor. Detailed SPIV measurement in the rotor tip region revealed complicated interactions of the tip flow with the casing groove. Further analysis showed how these grooves could delay the onset of stall but cause a performance penalty at higher flow rates.
- Studied novel casing treatments aimed at extending the operation range of the machine while did not degrade the performance near the best efficiency point.
- Conducted high-resolution 2D-PIV measurements in a Ventricular Assist Device model.

Beijing University of Aeronautics and Astronautics (1/2009 – 5/2013)

Research Assistant (Supervisor: Dr. Jinjun Wang)

- Conducted lift and drag measurements and oil flow visualizations of a delta wing with sinusoidal leading edges in a low-speed wind tunnel at BUAA.
- Designed and conducted hydrogen-bubble visualization, dye visualization and SPIV measurements in a water channel to investigate the leading edge vortices of delta wings with various sinusoidal leading edges.
- Simulated ice accretion on an unmanned aerial vehicle using ANSYS Fluent.
- Performed 2D-PIV measurement of the wake of a NACA0015 wing. Used dynamical mode decomposition method to analyze the data.

PUBLICATIONS

- Chen, H., Koley, S. S., Li, Y., & Katz, J. (2019), Systematic Experimental Evaluations aimed at Optimizing the Geometry of Axial Casing Groove in a Compressor, In *ASME Turbo Expo 2019, GT2019-91050. American Society of Mechanical Engineers.*
- Li, Y., Chen, H., & Katz, J. (2019) Challenges in Modelling of Turbulence in the Tip Region of Axial Turbomachines, *J. Ship Research, 2019, DOI: 10.5957/JOSR.09180054.*
- Chen, H., Li, Y., & Katz, J. (2018), On the Interactions of a Rotor Blade Tip Flow with Axial Casing Grooves in an Axial Compressor near the Best Efficiency Point, *J. Turbomach.*, 141(1), 011007.
- Chen, H., Doeller, N., Li, Y., & Katz, J. (2017), Measurements of the Flow and Pressure within an Axial Waterjet Pump during Cavitation Breakdown. *International Symposium on Transport Phenomena and Dynamics of Rotating Machinery, Maui, HI*.
- Chen, H., Li, Y., Koley, S. S., Doeller, N., & Katz, J. (2017), An Experimental Study of Stall Suppression and Associated Changes to the Flow Structures in the Tip Region of an Axial Low Speed Fan Rotor by Axial Casing Grooves, *J. Turbomach.*, 139(12), p. 121010.
- Li, Y., Chen, H., & Katz, J., (2017), Measurements and Characterization of Turbulence in the Tip Region of an Axial Compressor Rotor, *J. Turbomach.*, 139(12), p. 121003.
- Chen, H., Li, Y., Tan, D., & Katz, J. (2017), Visualizations of Flow Structures in the Rotor Passage of an Axial Compressor at the Onset of Stall. *J. Turbomach.*, 139(4), 041008.
- Chen, H., Li, Y., Doeller, N., Koley, S., Keyser, B., & Katz, J., (2016), Effects of Circumferential Grooves on the Cavitation and Performance of an Axial Waterjet Pump, In *Proceedings of the 31th Symposium on Naval Hydrodynamics, Monterey, CA*.
- Li, Y., Tan, D., Chen, H., & Katz, J., (2016), Stereoscopic PIV Measurement of the Flow in the Tip Region of an Axial Waterjet Pump, *International Symposium on Transport Phenomena and Dynamics of Rotating Machinery, Honolulu, HI*.

- Li, Y., Chen, H., Tan, D., & Katz, J., (2016), Effects of Tip Clearance and Operating Conditions on the Flow Structure and Reynolds Stresses within an Axial Compressor Rotor Passage. In *ASME Turbo Expo 2016, GT2016-57050. American Society of Mechanical Engineers.*
- Tan, D., Li, Y., Chen, H., Wilkes, I., & Katz, J. (2015), The Three Dimensional Flow Structure and Turbulence in the Tip Region of an Axial Flow Compressor. In *ASME Turbo Expo 2015: Turbine Technical Conference and Exposition (pp. V02AT37A036-V02AT37A036).*
- Chen, H., & Wang, J. J. (2014), Vortex Structures for Flow over a Delta Wing with Sinusoidal Leading edge. *Exp. Fluids*, 55(6), 1761.
- Chen, H., Pan, C. & Wang, J. J. (2013), Effects of Sinusoidal Leading Edge on Delta Wing Performance and Mechanism. SCIENCE CHINA Technological Sciences, 56(3), 772-779.

Conference Presentations

- 10th International Symposium on Cavitation, 2018, Baltimore, MD, *Experimental Investigations of Cavitation Performance Breakdown in an Axial Waterjet Pump*
- International Symposium on Transport Phenomena and Dynamics of Rotating Machinery 2017, Maui, HI, *Measurements of the Flow and Pressure within an Axial Waterjet Pump during Cavitation Breakdown*
- ASME Turbo Expo 2017, Charlotte, NC, *An Experimental Study of Stall Suppression and Associated Changes to the Flow Structures in the Tip Region of an Axial Low Speed Fan Rotor by Axial Casing Grooves*
- 31ST Symposium on Naval Hydrodynamics, 2016, Monterey, CA, E*ffects of Circumferential Grooves on the Cavitation and Performance of an Axial Waterjet Pump*